QUANTITATIVE SUSCEPTIBILITY MAPPING USING MAGNETIC RESONANCE IMAGING

A Dissertation

Presented to the Faculty of the Graduate School

of Cornell University

In Partial Fulfillment of the Requirements for the Degree of

Doctor of Philosophy

by

TIAN LIU

MAY 2011

QUANTITATIVE SUSCEPTIBILITY MAPPING USING MAGNETIC RESONANCE IMAGING

TIAN LIU, Ph. D.

Cornell University 2011

Magnetic susceptibility is an intrinsic tissue property that reflects underlying concentration of iron, calcification or contrast agents, which are useful for the investigation of a wide range of physiological or pathological conditions. Due to this promising outlook, there has been a long-standing interest in quantifying magnetic susceptibility. Although methods to quantify susceptibility of certain material samples have been proposed in the past, a practical means to measure an arbitrary susceptibility distribution in a living organism was lacking. Consequently, many of the potential applications were still in speculation.

This thesis reports a framework that allows quantitative mapping of magnetic susceptibility in human brain using magnetic resonance imaging (MRI). Two major building blocks were proposed to overcome the technical hurdles. First, a background field removal method was developed to obtain the magnetic field of interest free of contamination from background sources. Second, two independent methods were proposed to solve a classical ill-posed inverse problem of determining susceptibility sources from measured magnetic field.

With these technical developments, quantitative susceptibility mapping was realized. Its utility was demonstrated in a molecular MRI application, where identification and quantification of iron-based contrast agents are now feasible, and in cerebral MRI, where susceptibility provides a more objective measurement of hemorrhage, allowing cross-center comparisons and longitudinal studies.

BIOGRAPHICAL SKETCH

Tian Liu was born in Guangzhou, Guangdong, China in 1983. He received the Bachelors of Science degree in Electrical Engineering from Tsinghua University in 2006. He joined the graduate program in Biomedical Engineering at Cornell University in the fall of the same year, and received the Masters of Science degree in Biomedical Engineering in 2009.

I dedicate this thesis to my parents,

who sowed seeds of curiosity in my heart,

and convinced me

only sweat and integrity can nourish the seeds into sweet fruits.

ACKNOWLEDGMENTS

In the course of my Ph. D. study, I have found a new kind of people in my life, physicists. They have profound understanding of the physical laws governing the universe, yet their minds are never chained by the laws. “Physicist are the Peter Pans of the human race. They never grow up and they keep their curiosity.” In graduate school, I was blessed to have the opportunity to work with a few of them. With them, I simply feel happy.

The first physicist I would like to thank is my advisor and mentor Yi Wang. His scientific and personal guidance during these years is essential for my success in conducting original research. His unrelenting insist on grasping the insight of an idea has greatly influence not only the way I perform research but also my view on obstacles in life. Without his generosity to share his encouragement, or more importantly, criticism, it would not have been possible for me to finish this work.

I am greatly indebted to another physicist, Ludovic de Rochefort, for introducing me to the area of magnetic susceptibility quantification, which later turned out to be my thesis project. His elegant treatments of complex problems has an aesthetic appeal even better than the most beautiful MR image. His willingness to share his extensive knowledge in susceptibility and MRI has ushered me into this exciting new research area.

There is a third physicist to whom I owe particular thanks: Pascal Spincemaille. His constant intellectual advice has helped me endure periods when technical difficulties seemed formidable, and his sporadic comic support made me enjoy the challenges nature poses to us. In addition to coaching me the nuts and bolts of MRI, he also demonstrated to me how to think out of the box when conventional methods did not work.

Although Ph.D. training fosters independent research, my work could never have

been done in solitary. I owe a deep debt of gratitude to other people in my lab. Bryan Kressler was instrumental in my learning of MRI basics and convex optimization, and his rigor in research exemplified what a true engineer should be. I am grateful to Jing Liu, who gave much encouragement and advice regarding work and life during my time in graduate school. Ildar Khalidov has incredible insights into mathematical analysis and has provided many illuminating discussion. I am especially thankful to Thanh Nguyen, who has shown tremendous selflessness and patience in his availability to advise me, no matter how nitpicking I might be. I would like to thank James Ledoux for his technical support in dealing with many complex physics and computer problems. I feel fortunate to work with a group of young, bright and energetic graduate students, Ryan Brown, Noel Codella, Keigo Kawaji, Bo Xu, Mitchell Cooper and Cynthia Wisnieff, who have supplied a lot of encouragement, enlightenment, and occasional bad jokes.

Trying to write a medical paper for a person cultivated for engineering could be a nightmare. The shift in focus and the jargon and the data collection could be overwhelming for any novice to handle. But to my surprise, this task is not completely impossible when you have wonderful collaborators.

Dr. Martin Prince, a professor of medicine, mechanics, and almost anything else I can think of, has been instrumental in helping me establish collaborations with clinicians. His extensive knowledge of MRI has deeply influenced my research, and his keen intellect in identifying key problems has directly facilitate my progress.

I am deeply grateful to Dr. Krishna Surapaneni for his constant level of encouragement, support, and dedication to our collaborative projects. He gave me much useful advice to improve our algorithm, and supplied a lot of patient data with unimaginable efficiency. His commitment is crucial to the cerebral microbleed project.

I would like to thank many other collaborators, John Tsiouris, Craig Horenstein, Weiwei Chen, Min Lou, Jianlin Wu, Qing Zhang, Liuquan Cheng, and Minming Zhang, for providing patient data throughout my work.

Genius is 1 percent inspiration and 99 percent perspiration, so as graduate school. My gratitude to my roommates Richard Wong and Brian Lawrence, who have never left our fridge out of beer whenever hydration is needed. I am deeply thankful to a special person: Xin Liu, who is working towards her Ph.D. at the time this thesis was written, for providing unconditional support and assistance. I also appreciate my friends for providing constant encouragement and assistance. You have taught me, may or may not in academia, more than any could know, and if you are still reading this paragraph, yes, my friend, I am thanking you.

Finally, I would like to acknowledge the members of my special committee, Ehsan Afshari, David Christini and Yi Wang, who agreed to act as official examiners of this thesis.

TABLE OF CONTENTS

BIOGRAPHICAL SKETCH iii

ACKNOWLEDGMENTS v

TABLE OF CONTENTS viii

LIST OF FIGURES xi

LIST OF TABLES xii

LIST OF ABBREVIATIONS xiii

1 INTRODUCTION 1
1.1 Summary of Contribution 3

2 BACKGROUND 5
2.1 Basics of Magnetic Susceptibility 5
2.2 Prior Work on Measuring Susceptibility 6
2.3 Measuring Susceptibility using MRI 7
2.3.1 Relation between Tissue Magnetization to Magnetic Field 7
2.3.2 Data Acquisition in MRI 9
2.3.3 Measuring Magnetic Field from MR Signal Phase 11
2.3.4 Inverse Problem from Magnetic Field to Susceptibility Source 11
2.4 Reference 14

3 BACKGROUDN FIELD REMOVAL 17
3.1 Abstract 17
3.2 Introduction 17
3.3 Theory: Approximate Dipole Field Orthogonality and Projection Theorem 19
3.3.1 Error analysis 21
3.4 Methods and Materials 23
3.4.1 PDF algorithm implementation 23
3.4.2 Comparison with High-Pass filtering 24
3.4.3 Validation of background field removal methods 25
3.5 Results 29
3.6 Discussion 32
3.7 Conclusion 36
3.8 Acknowledgement 36
3.9 Reference 37

4 CALCULATION OF SUSCEPTIBILITY THROUGH MULTIPLE ORIENTATION SAMPLING 41
4.1 Abstract 41
4.2 Introduction 41
4.3 Theory 43

4.3.1 Relationship between Susceptibility and Magnetic Field 43
4.3.2 Inversion from Multiple Orientations 44
4.3.3 Stability of Inversion and Optimal Sampling Orientations 46
4.3.4 Noise Considerations 48
4.4 Materials and Methods 49
4.4.1 Optimal Sampling Orientations 49
4.4.2 Numerical Simulation 50
4.4.3 MRI Experiments 50
4.5 Results 53
4.5.1 Optimal Sampling Orientations 53
4.5.2 Numerical Phantom 54
4.5.3 Experimental results 55
4.6 Discussion 58
4.7 Conclusion 63
4.8 Appendix 64
4.8.1 Sampling from 2 different directions is insufficient to eliminate all the zeroes in the Fourier domain kernel 64
4.8.2 Sampling from 3 different directions will eliminate all the zeroes in the Fourier domain kernel except the origin. 65
4.9 Reference 67

5 MORPHOLOGY ENABLED DIPOLE INVERSION 73
5.1 Abstract 73
5.2 Introduction 73
5.3 Theory 75
5.3.1 Morphology Enabled Dipole Inversion (MEDI) 75
5.3.2 Calculation Of Susceptibility through Multiple Orientation Sampling (COSMOS) 76
5.4 Methods and Materials 77
5.4.1 Data acquisition 77
5.4.2 Field Map Estimation 78
5.4.3 Susceptibility Analysis 78
5.5 Results 80
5.6 Discussion 86
5.7 Conclusion 89
5.8 Reference 91

6 DIFFERENTIATION OF SPIO AND AIR BUBBLE 94
6.1 Abstract 94
6.2 Introduction 94
6.3 Theory 95
6.3.1 Improved COSMOS using regularization 97
6.4 Methods and Materials 98
6.4.1 Numerical simulation 98
6.4.2 Phantom and ex vivo validations 98
6.5 Results 102
6.6 Discussion 105

6.7 Conclusion 109
6.8 Acknowledgement 109
6.9 Reference 109

7 MEASUREMENT OF CEREBRAL MICROBLEED BURDEN 115
7.1 Abstract 115
7.2 Introduction 116
7.3 Methods and Materials 117
7.3.1 Data Acquisition 117
7.3.2 Data Reconstruction 118
7.3.3 Data Analysis 120
7.3.4 Statistical Analysis 122
7.4 Results 122
7.5 Discussion 126
7.6 Reference 130

8 FUTURE DIRECTIONS AND CONCLUSION 136
8.1 Future Directions 136
8.1.1 QSM at High Field 136
8.1.2 Algorithmic Improvements 136
8.1.3 Exploration of Applications 138
8.2 Conclusion 140

LIST OF FIGURES

Figure 1.1. Relationship between susceptibility source and MR signal phase. 1

Figure 2.1. Illustration of the zero cone and the ill-posed inverse problem. 13

Figure 3.1. Approximate orthogonality between dipole fields. 22
Figure 3.2. Validation in numerical simulation. 30
Figure 3.3. Validation in phantom MRI. 31
Figure 3.4. Patient brain imaging. 33

Figure 4.1. Determination of the minimum number of required rotations. 46
Figure 4.2. Color map of the matrix condition number 54
Figure 4.3. Numerical simulation of susceptibility inversion. 55
Figure 4.4. Gd-water phantom experiment 56
Figure 4.5. In vitro bone experiment 57
Figure 4.6. In vitro iron quantification. 59

Figure 5.1. A representative case of MEDI-calculated QSM. 82
Figure 5.2. Qualitative and quantitative comparison between MEDI and COSMOS. 86
Figure 5.3. A zoom-in on the cortical regions. 89

Figure 6.1. Illustration of magnetizations curves of SPIO and air. 96
Figure 6.2. Numerical simulation of a susceptibility mapping experiment 102
Figure 6.3. Phantom experimental results. 104
Figure 6.4. Mouse experimental results. 106
Figure 6.5. Magnetic moment ratios between 3T and 1.5T 107

Figure 7.1. Schematic view of the QSM reconstruction. 118
Figure 7.2. Qualitative and quantitative analysis of the QSM at different TEs. 124
Figure 7.3. Comparison with R2*map, T2*W and SWI on a representative case. 125
Figure 7.4. Comparison with R2*map, T2*W and SWI across all the patients. 126
Figure 7.5. Iron and calcium deposits on R2* and QSM. 128

LIST OF TABLES

Table 5.1. Comparison of net scan time, calculation time, CNR and image score. 81
Table 5.2. Susceptibility in different brain regions. 84

Table 6.1. Measured susceptibilities in different signal void spheres.(Mean±std) 103
Table 6.2. Calculated magnetic moments..... 104
Table 6.3. MRI measured iron mass through quantitative susceptibility mapping. ... 105

Table 7.1. CMB finding summary..... 123

LIST OF ABBREVIATIONS

BW	Band Width
CG	Conjugate Gradient
CMB	Cerebral Micro Bleed
COSMOS	Calculation Of Susceptibility through Multiple Orientation Sampling
FA	Flip Angle
FOV	Field Of View
HP	High Pass filtering
ISMRM	International Society of Magnetic Resonance in Medicine
MEDI	Mophology Enabled Dipole Inversion
MRI	Magnetic Resonance Imaging
NEX	Number of EXcitation
PDF	Projection onto Dipole Fields
QSM	Quantitative Susceptibility Mapping/Map
ROI	Region Of Interest
SNR	Signal Noise Ratio
SPIO	Super Paramagnetic Iron Oxide
SQUID	Superconducting QUantum Interference Device
SWI	Susceptibility Weighted Imaging/image
T2*W	T2* Weighted imaging/image
TE	Echo Time
TR	Repetition Time

CHAPTER 1

1 INTRODUCTION

Magnetic susceptibility (or susceptibility for conciseness) is a physical property of a material that is useful for chemical identification and quantification of specific biomarkers including iron, calcium and contrast agents. A spatially varying susceptibility distribution, when placed in an externally applied uniform magnetic field such as the one in a magnetic resonance imaging (MRI) scanner, will induce field inhomogeneity that may be recorded in the reconstructed signal phase. Therefore, MRI provides an excellent opportunity to study magnetic susceptibility.

Nevertheless, MRI does not directly measure susceptibility. As illustrated in Figure 1.1, the susceptibility source induces a local magnetic field which has a long range spatially varying distribution. Additionally, the measured magnetic field is contaminated by some background field. This non-uniform field is traditionally viewed as a source of image artifacts in MRI. Therefore, before actualizing the utility of susceptibility in general research, two technical challenges need to be overcome in the first place (red arrows in Figure 1.1).

Figure 1.1. Relationship between susceptibility source and MR signal phase.

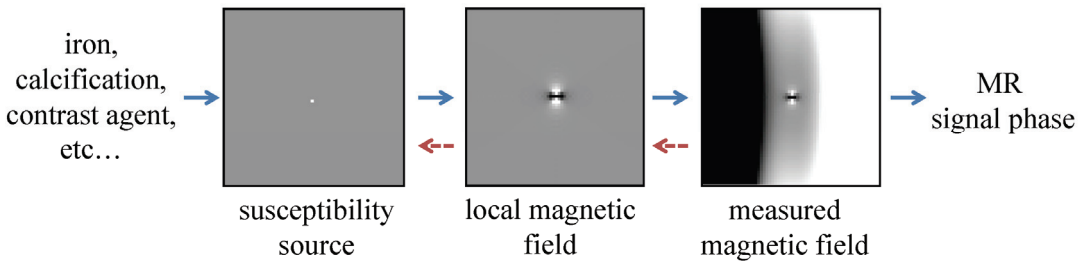

First, the background field needs to be removed. In human brain MRI, the background field arises from the interface between brain tissue and surrounding air, whose contribution to the measured magnetic field is orders of magnitude stronger than that from tissue susceptibility. For the investigation of tissue susceptibility, a robust method must be achieved to suppress the air contribution while preserving the local field.

Second, the local field reflects the change of susceptibility, but it is not an intrinsic tissue property. The field induced by an object with non-zero susceptibility depends on the shape, the orientation of the object, and in fact, many different objects may generate a same field. Due to this intrinsic ambiguity, the field-to-source process is a classical ill-posed inverse problem in electromagnetics, and a practical solution to this quantitative susceptibility mapping (QSM) is a long sought-after goal.

Because susceptibility value is linearly proportional to the density of paramagnetic or diamagnetic materials, a successful implementation of QSM in MRI will open the door for many potential applications where quantitative knowledge about concentration is essential. For example, it is of great interest to monitor the biodistribution of drugs or injected cells labeled with contrast agents in a living organism, which was almost a prohibitive task for most molecular MRI techniques that are qualitative in nature and have difficulty in differentiating an air bubble from super paramagnetic iron oxide (SPIO) particles. It may also be beneficial for gauging cerebral microbleed severity, in which traditional size measurement are semi-quantitative, and is unreliable for longitudinal patient follow-up or cross center comparison studies.

1.1 Summary of Contribution

The work in this thesis aimed to a) develop a robust and practical technique to accurately quantify susceptibility using MRI and b) explore preliminary applications to demonstrate the utility. Three new technical developments are proposed, including the suppression of the background field, a physical approach to solve the field-to-source inverse problem, and a mathematical approach that is more practical. Two potential applications are demonstrated, including an unambiguous identification of contrast agents in molecular MRI and an objective measurement of hemorrhage in patients. Specifically, the following five topics are presented:

1. Background Field Removal. Chapter 3 reports an observation that the magnetic field of a dipole outside a given region of interest (ROI) is approximately orthogonal to the magnetic field of a dipole inside the ROI. Accordingly, a nonparametric background field removal technique is proposed based on projection onto dipole fields (PDF). In this PDF technique, the background field inside an ROI is attributed to a field originating from susceptibility sources outside the ROI using the projection theorem in Hilbert space.

2. Calculation Of Susceptibility through Multiple Orientation Sampling. Chapter 4 proposed the first MRI technique to calculate arbitrary susceptibility distribution, which solves the magnetic field to susceptibility source inverse problem using a physical approach. The field created by the susceptibility distribution is sampled at multiple orientations with respect to the polarization field B_0, and the susceptibility map is reconstructed by weighted linear least squares to account for field noise and the

signal void region.

3. Morphology Enabled Dipole Inversion. Chapter 5 presented a mathematical approach to solve the inverse problem by employing a weighted L1 minimization method. The accuracy of this technique is validated in *in vivo* human brain imaging by comparing with the results calculated from COSMOS.

4. Differentiation of SPIO and air bubble. Chapter 6 introduced a novel method for unambiguous identification of SPIO in the presence of air bubble. The response of SPIO to an externally applied magnetic field is nonlinear. Magnetization of SPIO saturates at around 1 T while magnetization of water and air increase linearly with field strength. This serves as the premise to differentiate these two materials at two field strengths.

5. Measurement of cerebral microbleed burden. Chapter 7 presents a clinical study of using total susceptibility to measure cerebral microbleed (CMB) burden. It is found in this study that the quality of QSM is less dependent on the choice of echo time compared to T2* weighted image, R2* map and susceptibility weighted image. Using total susceptibility to measure CMBs overcomes the sensitive dependence on TE in CMB size measurement, offering a more objective means to characterize CMB burden.

CHAPTER 2

2 BACKGROUND

Magnetic susceptibility is a physical property of a material characterizing its degree of magnetization in response to an external magnetic field. This physical parameter is useful for deriving physiological or pathological parameters when its value can be accurately measured. This chapter briefly reviews the basics of susceptibility and previous efforts in quantifying susceptibility using other modalities. It also provides a brief overview of the opportunity of using MRI to calculate susceptibility and the difficulties. Specific issues related to Quantitative Susceptibility Mapping in MRI are discussed in details in Chapter 3~7.

2.1 Basics of Magnetic Susceptibility

Every material acquires a magnetic moment when it is put in a magnetic field **H**. Magnetic susceptibility χ, defined as $\chi = \mathbf{M/H}$, with **M** being the magnetic moment per unit volume (magnetization), is an intrinsic property of the material, reflecting its electronic perturbation by the applied magnetic field. For some materials such as gadolinium, The strong intrinsic magnetic moment of unpaired electrons give rise to paramagnetism ($\chi > 0$). For some other materials such as calcification, the precession of the paired electron spins create a magnetic field opposing the external field, giving rise to diamagnetism.

These material magnet moment is not on resonance and does not contribute directly signal in MRI, in contrast to the much weaker nuclear magnetic moment of free water

that is on resonance and directly contribute signal in MRI. To mark this distinction, the material magnetic moment is also referred as the bulk magnetic moment. Statistical quantum mechanics may allow calculation of susceptibility for some materials of given configuration. Very important for biomedical practice is an experimental method to measure tissue susceptibility.

2.2 Prior Work on Measuring Susceptibility

Magnetic susceptibility measurements of biomaterials have been investigated using a superconducting quantum interference device (SQUID) (1-5). Using superconducting detection coils, SQUID can detect small flux of the magnetic field of an object magnetized by a primary field. Assuming the object is comprised of regions of uniform susceptibility distribution, regional susceptibilities are related to SQUID coil fluxes through numerically calculated geometry factors, allowing estimation by inverting a set of linear equations(6-7). It has also been proposed that a 3D susceptibility distribution may be reconstructed by using a composite of multiple SQUID coils (5) in a manner similar to the inversion used in magnetoencephalography (MEG) (8). Because SQUID coils of finite sizes have to be placed outside the human body, the number of flux detectors is limited, the inversion reconstruction is not well behaved, and the spatial resolution of mapping static susceptibility is very poor as demonstrated in MEG. The poor spatial resolution (~ 1 cm) will make it difficult to detect subtle lesions. Furthermore, this technology is not widely available and its clinical applicability is therefore limited (2).

2.3 Measuring Susceptibility using MRI

2.3.1 Relation between Tissue Magnetization to Magnetic Field

The existence of a spatially varying susceptibility distribution will alter the applied external magnetic field. We formulate here the exact relation between tissue magnetization and magnetic field directly from the fundamental Maxwell equation (9-11). For a given magnetization distribution $\boldsymbol{m}(\boldsymbol{r})$ of tissue in an MR scanner, the corresponding macroscopic magnetic field $\boldsymbol{b}(\boldsymbol{r})$ can be derived from the Maxwell Equation of static magnetism,

$$\nabla \cdot \boldsymbol{b} = 0, \qquad [2.1a]$$

$$\nabla \times \boldsymbol{b} = \mu_0 \nabla \times \boldsymbol{m}. \qquad [2.1b]$$

It should be noted that MRI phase measures the local field $\underline{\boldsymbol{b}}$ experienced by water spins, which is different from the macroscopic field $\boldsymbol{b}$ because of the susceptible materials surrounding the water spin. The Lorentz sphere correction model may be used that gives (12-13)

$$\underline{\boldsymbol{b}} = \boldsymbol{b} - (2/3)\, \mu_0 \boldsymbol{m}. \qquad [2.2]$$

We will solve Eq.2.1 first and then apply the Lorentz correction. The two first order differential equations in Eq.2.1 can be combined into a single second order differential equation,

$$-\nabla^2 \boldsymbol{b} = \mu_0 [\nabla(\nabla \cdot \boldsymbol{m}) - \nabla^2 \boldsymbol{m}] \qquad [2.3]$$

The solution to Eq.2.3 can be easily derived in Fourier domain $\boldsymbol{b}(\boldsymbol{r}) = \int d^3\boldsymbol{k}\boldsymbol{B}(\boldsymbol{k})e^{-i\boldsymbol{k}\boldsymbol{r}} = F^{-1}[\boldsymbol{B}(\boldsymbol{k})]$, where differentiation becomes multiplication by $\boldsymbol{k}$, the k-space position vector:

$$\boldsymbol{k}^2\boldsymbol{B}(\boldsymbol{k}) = \mu_0[\boldsymbol{k}^2\boldsymbol{M}(\boldsymbol{k})-(\boldsymbol{k}\cdot\boldsymbol{M}(\boldsymbol{k}))\boldsymbol{k}], \qquad [2.4]$$

Therefore, after applying the Lorentz correction,

$$\underline{\boldsymbol{B}}(\boldsymbol{k}) = \boldsymbol{B}_0\delta(\boldsymbol{k}) + \mu_0[\boldsymbol{M}(\boldsymbol{k})/3-(\boldsymbol{k}\cdot\boldsymbol{M}(\boldsymbol{k}))\boldsymbol{k}/k^2], \qquad [2.5]$$

where the first term is the magnet B_0 field at k=0 where Eq.2.4 is problematic. For all tissues, $\chi << 1$, and magnetic susceptibility and magnetization relation can be simplified as

$$\chi(\boldsymbol{r}) \equiv \mu_0\, \boldsymbol{m}(\boldsymbol{r})/\boldsymbol{B}_0 \qquad [2.6]$$

The equilibrium directions of magnetization and magnetic fields are along z, so we will focus on the z-component of the magnetic field that can be detected from MR signal phase. For notational convenience, we introduce the relative difference field

$$\delta_B(\boldsymbol{r}) \equiv (\underline{b}_z(\boldsymbol{r}) - B_0)/B_0, \qquad [2.7]$$

whose Fourier transform $\Delta_B(\boldsymbol{k})$ can be simply expressed according to Eq.5 as

$$\Delta_B(\boldsymbol{k}) = (1/3-k_z^2/k^2)X(\boldsymbol{k}),$$

$$=D(k)\ X(\boldsymbol{k}) \qquad [2.8]$$

where $X(\boldsymbol{k})$ is the Fourier domain susceptibility $\chi(\boldsymbol{r}) = F^{-1}[X(\boldsymbol{k})]$. Using direct Fourier

transformation (14), the corresponding formulation in image space is

$$\delta_B(\boldsymbol{r}) = (1/4\pi)\int d^3\boldsymbol{r}' \,(3\cos^2\theta_{\boldsymbol{r}\boldsymbol{r}'} - 1)/|\boldsymbol{r}-\boldsymbol{r}'|^3 \chi(\boldsymbol{r}')$$

$$= d(\boldsymbol{r}) \otimes \chi(\boldsymbol{r}). \qquad [2.9]$$

The kernel that relates susceptibility to the measured relative field in the above Eq.2.9 or its Fourier form Eq.2.8 is called the dipole kernel, or the unit dipole response field:

$$d(\boldsymbol{r}) = (1/4\pi)(3\cos^2\theta - 1)/r^3 = F^{-1}[(1/3 - k_z^2/k^2)] = F^{-1}[D(\boldsymbol{k})]. \qquad [2.10]$$

It should be noted that there is an alternative and equivalent way to derive the forward problem Eq.2.9 using the magnetic field formula for a single dipole (12). The superposition principle gives the field of an arbitrary distribution $\boldsymbol{m}(\boldsymbol{r})$ as summation over all dipole contributions. The z-component along B_0 direction for the macroscopic magnetic field is (15),

$$b_z(\boldsymbol{r}) - B_0 = \int d^3\boldsymbol{r}' \mathrm{m}(\boldsymbol{r}')\mu_0/4\pi \times [(3\cos^2\theta_{\boldsymbol{r}\boldsymbol{r}'} - 1)/|\boldsymbol{r}-\boldsymbol{r}'|^3 + 8\pi/3\,\delta(\boldsymbol{r}-\boldsymbol{r}')], \qquad [2.11]$$

which leads to Eq.2.9 as its second term is canceled by the Lorentz correction in Eq.2.2.

2.3.2 Data Acquisition in MRI

In gradient echo MRI, the image formation from excited proton spins is achieved through frequency encoding. After a radio frequency excitation, the magnetization of the proton spins will precess in the transverse plane. If a loop of wire is placed close to the object being imaged to detect the magnetic flux, it follows Faraday's law of

induction that a time varying current can be detected in the wire. This excitation-detection process is applied repetitively with gradually changing parameters to form a complete image.

In each repetition, the received signal, neglecting T2 decay effect and taking into account the center frequency demodulation, can be expressed as:

$$S(\tau) = \int \rho(\boldsymbol{r}) e^{-i\Delta B(\boldsymbol{r})\gamma\tau} d\boldsymbol{r}, \qquad [2.12]$$

where τ denotes the time, ρ denotes the transverse magnetization, γ is the gyromagnetic ratio ($2\pi\times42.576\text{MHzT}^{-1}$ for hydrogen), ΔB is the strength of the additional gradient field for frequency encoding.

When Cartesian sampling strategy is used, the gradient fields vary linear in space and are constant in each repetition: $\Delta B(\boldsymbol{r}) = \boldsymbol{r}\cdot\boldsymbol{G}$ with $\boldsymbol{G}$ being the vector representation of the spatial magnetic field gradient and the dot sign denoting inner product. Therefore, the signal equation Eq. 2.12 becomes:

$$S(\tau) = \int \rho(\boldsymbol{r}) e^{-i\boldsymbol{r}\boldsymbol{G}\gamma\tau} d\boldsymbol{r}, \qquad [2.13a]$$

$$\text{or, } S(\boldsymbol{k}) = \int \rho(\boldsymbol{r}) e^{-i\boldsymbol{r}\boldsymbol{k}} d\boldsymbol{r}, \qquad [2.13b]$$

, where $\boldsymbol{k}=\boldsymbol{G}\gamma\tau$. Examining this equation, it becomes clear that the signal acquired by the MRI scanner represents the coefficients of the spatial Fourier transform of the object. In MRI, this spatial Fourier domain is referred to as *k*-space. With acquired signal in *k*-space, the restoration of the image only requires an inverse Fourier transform.

2.3.3 Measuring Magnetic Field from MR Signal Phase

The previous section described an idealized scenario where ΔB is exactly the precisely engineered gradient field. In practice, field inhomogeneity arising from spatially varying susceptibility will also contribute to ΔB:

$$S(\boldsymbol{k}) = \int \rho(\boldsymbol{r}) e^{-i\delta B(\boldsymbol{r})\gamma t} e^{-i\boldsymbol{r}\boldsymbol{k}} d\boldsymbol{r}, \qquad [2.14]$$

where $\delta B(\boldsymbol{r}) = \delta_b(\boldsymbol{r}) B_0$ denotes the field inhomogeneity, $t = \mathrm{TE} + \tau$ indicates the elapsed time from the end of excitation with TE being the echo time. With an approximation that $\delta B\gamma << \mathbf{1}\cdot\boldsymbol{G}\gamma$, which reflects the frequency bandwidth of one voxel, the signal equation can be reparameterized using substitution:

$$S(\boldsymbol{k}) = \int \rho(\boldsymbol{r}) e^{-i\delta B(\boldsymbol{r})\gamma TE} e^{-i\boldsymbol{r}\boldsymbol{k}} d\boldsymbol{r}, \qquad [2.15]$$

An inverse Fourier transform of the acquired data in *k*-space leads to the original magnetization distribution $\rho(\boldsymbol{r})$ with an additional term $e^{-i\delta B(\boldsymbol{r})\gamma \mathrm{TE}}$, whose phase $-\delta B(\boldsymbol{r})\gamma \mathrm{TE}$ encodes the field inhomogeneity.

2.3.4 Inverse Problem from Magnetic Field to Susceptibility Source

In the case of ideal field data without noise and available in continuous space, the dipole kernel defined in Eq.2.10 may be regarded as well conditioned for the field to source inverse problem of Eq.2.9 or Eq.2.10. This point may be appreciated in the following manner of examining Eq.2.9. When the dipole kernel in k-space is non zero, susceptibility can be obtained by direct division of the dipole kernel. At locations where the dipole kernel become zero, the field also becomes zero (16), and

L'Hospital's rule may be used to estimate susceptibility by taking derivative along a direction of kernel variation (17):

$$X(\boldsymbol{k}) = \Delta_B(\boldsymbol{k})/D(\boldsymbol{k}), \qquad \text{for } D(\boldsymbol{k})\neq 0$$

$$=\partial\Delta_B(\boldsymbol{k})/\partial D(\boldsymbol{k}), \qquad \text{for } D(\boldsymbol{k})=0. \qquad [16]$$

When there is noise in field data (and there is always noise in real data), L'Hospital's rule cannot be applied, and the above approach in Eq.2.16 will generate severe noise artifacts (18). The zeroes of the dipole kernel at $k_z^2=k^2/3$ form two opposing cone surfaces at the magic angle (~54.7^0 from the main magnetic field, Figure 2.1a). Noise in the neighborhood of these cone surfaces prevents determination of susceptibility, i.e., any $X(\boldsymbol{k})$ will give zero magnetic field at these cone surfaces. This causes the ill-posedness of the inverse problem (19-21). This theoretical analysis is exemplified in a case illustrated in Figure 2.1c-d when the straightforward k-space division (Eq.2.16) is used for inversion from field to source to reconstruct susceptibility map. A little noise added in the phase map (SNR = 20) leads to a totally corrupted image of susceptibility that bear no physical resemblance to the true susceptibility source (18).

To get a sense of noise propagation, we can examine the condition number of the dipole kernel that characterizes the upper bound of noise propagation (22),

$$\kappa = \max_k|1/3-k_z^2/k^2|/\ \min_k|1/3-k_z^2/k^2|= k_m/\varepsilon, \qquad [13]$$

where k_m is the maximal value of sampled k_z and ε is the closest distance the sampled point to the zero cone surface at maximal k_z. Therefore, this condition number is large, resulting in large noise propagation.

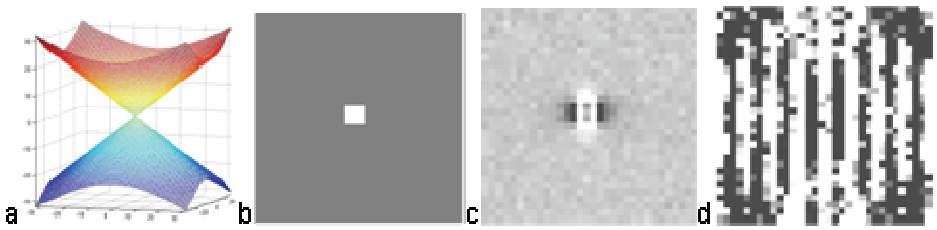

Figure 2.1. Illustration of the zero cone and the ill-posed inverse problem. a) the zero cone surfaces of the dipole kernel in k-space. b) susceptibility source. c) field map derived at SNR=20. d) direct inversion image (Eq.2.16).

2.4 Reference

1. Allen PD, St Pierre TG, Chua-anusorn W, Strom V, Rao KV. Low-frequency low-field magnetic susceptibility of ferritin and hemosiderin. Bba-Mol Basis Dis. 2000;1500(2):186-96.

2. Brittenham GM, Sheth S, Allen CJ, Farrell DE. Noninvasive methods for quantitative assessment of transfusional iron overload in sickle cell disease. Semin Hematol. 2001;38(1 Suppl 1):37-56.

3. Carneiro AAO, Fernandes JP, de Araujo DB, et al. Liver iron concentration evaluated by two magnetic methods: Magnetic resonance imaging and magnetic susceptometry. Magnet Reson Med. 2005;54(1):122-8.

4. Nielsen P, Engelhardt R, Duerken M, Janka GE, Fischer R. Using SQUID biomagnetic liver susceptometry in the treatment of thalassemia and other iron loading diseases. Transfus Sci. 2000;23(3):257-8.

5. Sepulveda NG, Thomas IM, Wikswo JP. Magnetic-Susceptibility Tomography for 3-Dimensional Imaging of Diamagnetic and Paramagnetic Objects. Ieee T Magn. 1994;30(6):5062-9.

6. Farrell DE, Allen CJ, Whilden MW, et al. A new instrument designed to measure the magnetic susceptibility of human liver tissue In vivo. Ieee T Magn. 2007;43(9):3543-54.

7. Farrell DE, Tripp JH, Zanzucchi PE, Harris JW, Brittenham GM, Muir WA. Magnetic Measurement of Human Iron Stores. Ieee T Magn. 1980;16(5):818-23.

8. Hamalainen M, Hari R, Ilmoniemi RJ, Knuutila J, Lounasmaa OV. Magnetoencephalography - Theory, Instrumentation, and Applications to Noninvasive Studies of the Working Human Brain. Rev Mod Phys. 1993;65(2):413-97.

9. de Rochefort L, Nguyen T, Brown R, et al. In vivo quantification of contrast agent concentration using the induced magnetic field for time-resolved arterial input function measurement with MRI. Med Phys. 2008;35(12):5328-39.

10. Marques JP, Bowtell R. Application of a fourier-based method for rapid calculation of field inhomogeneity due to spatial variation of magnetic susceptibility. Concept Magn Reson B. 2005;25B(1):65-78.

11. Salomir R, De Senneville BD, Moonen CTW. A fast calculation method for magnetic field inhomogeneity due to an arbitrary distribution of bulk susceptibility. Concept Magn Reson B. 2003;19B(1):26-34.

12. Jackson JD. Classical eletrodynamics. 3rd ed: John Wiley and Sons, inc., 1999.

13. Haacke EM, Brown RW, Thompson MR, Venkatesan R. Magnetic Resonance Imaging - physical principles and sequence design. New York: Wiley-Liss, 1999.

14. Lifshitz EM, Berestetskii VB, Pitaevskii LP. Quantum Electrodynamics. 2nd ed: Butterworth-Heinemann, 1982.

15. Li L, Leigh JS. Quantifying arbitrary magnetic susceptibility distributions with MR. Magn Reson Med. 2004;51(5):1077-82.

16. Haacke EM, Cheng NY, House MJ, et al. Imaging iron stores in the brain using magnetic resonance imaging. Magn Reson Imaging. 2005;23(1):1-25.

17. Li W, Wu B, Liu C. Quantitative susceptibility mapping of human brain reflects spatial variation in tissue composition. Neuroimage. 2011.

18. Kressler B, de Rochefort L, Liu T, Spincemaille P, Jiang Q, Wang Y. Nonlinear regularization for per voxel estimation of magnetic susceptibility distributions from MRI field maps. IEEE Trans Med Imaging. 2010;29(2):273-81.

19. Hanke M, Hansen PC. Regularization methods for large-scale problems. Surveys on Mathematics for Industry. 1993;3:253-315.

20. Bertero M, Boccacci P. Introduction to inverse problems in imaging: IoP, 1998.

21. Aster RC, Bochers B, Thurber CH. Parameter estimation and inverse problems: Elsevier, 2005.

22. Moon TK, Stirling WC. Matrix condition number. Mathematical Methods and Algorithms for signal processing. Upper Saddle River, New Jersey: Marsha Horton, 2000; p. 253-5.

23. Jung CW, Jacobs P. Physical and chemical properties of superparamagnetic iron oxide MR contrast agents: ferumoxides, ferumoxtran, ferumoxsil. Magn Reson Imaging. 1995;13(5):661-74.

24. de Rochefort L, Brown R, Prince MR, Wang Y. Quantitative MR susceptibility mapping using piece-wise constant regularized inversion of the magnetic field. Magn Reson Med. 2008;60(4):1003-9.

25. Smith SM. Fast robust automated brain extraction. Hum Brain Mapp. 2002;17(3):143-55.

26. Cusack R, Papadakis N. New robust 3-D phase unwrapping algorithms: application to magnetic field mapping and undistorting echoplanar images. Neuroimage. 2002;16(3 Pt 1):754-64.

CHAPTER 3

3 BACKGROUDN FIELD REMOVAL

3.1 Abstract

For optimal image quality in susceptibility weighted imaging and accurate quantification of susceptibility, it is necessary to isolate the local field generated by local magnetic sources (such as iron) from the background field that arises from imperfect shimming and variations in magnetic susceptibility of surrounding tissues (including air). Previous background removal techniques have limited effectiveness depending on the accuracy of model assumptions or information input. In this article, we report an observation that the magnetic field for a dipole outside a given region of interest (ROI) is approximately orthogonal to the magnetic field of a dipole inside the ROI. Accordingly, we propose a non-parametric background field removal technique based on projection onto dipole fields (PDF). In this PDF technique, the background field inside a ROI is decomposed into a field originating from dipoles outside the ROI using the projection theorem in Hilbert space. This novel PDF background removal technique was validated on a numerical simulation and a phantom experiment and was applied in human brain imaging, demonstrating substantial improvement in background field removal compared to the commonly used high-pass filtering method.

3.2 Introduction

The magnetic susceptibility of biomaterials generates a local magnetic field and provides a very important contrast mechanism in magnetic resonance imaging, such as T2* weighted imaging, susceptibility weighted imaging (SWI) (1) and quantitative

susceptibility mapping (QSM) (2-8). Recently, it has been reported that accurate QSM can be generated by combining information from magnitude and phase images (3). For proper phase masking in SWI and accurate susceptibility quantification in QSM (9), it is necessary to separate the local field in a given region of interest (ROI) from the background field. This background field arises from various sources including imperfect shimming and magnetic susceptibility sources outside the region of interest (both inside and outside the imaging volume). For example, in brain imaging, the air-tissue interfaces near the skull and various air cavities induce a strong background field variation extending deep into the brain. The background field is superimposed onto the local fields generated by venous blood, iron deposition and calcifications, impeding clear visualization of the local details in SWI and introducing errors in QSM.

Current background removal techniques assume the local and background fields in a space spanned by the Fourier basis (10) or polynomial functions are separable (2,11-12), or require a priori knowledge of the spatial distribution of all background susceptibility sources (13-14). The assumption of the separability between local and background field in a certain space is often violated, leading to erroneous estimation of local fields and the results depend on the choice of the basis functions (11). In practice, the knowledge of the background susceptibility source surrounding a given ROI is often not fully available or sufficiently accurate, particularly when there are significant variations in susceptibility outside the imaging field of view (FOV), leading to substantial residual background field that requires additional attention (13). A reliable background field removal method is the use of reference scans, in which an

identical object but with the susceptibility sources removed is scanned to measure the reference background field (2,7). However, it is impractical or impossible to perform a reference scan in many in vivo situations.

We recently described a method that effectively fits the background field to the field generated by dipole sources outside a certain ROI (3). This method is further confirmed by another group (15). In this paper, we provide a detailed description and justification of this new approach to background field removal, which we term here as a projection onto dipole fields (PDF) method. We observe that the inner product of the field of a background dipole outside the ROI and the field of a local dipole inside the ROI is almost zero in the ROI except for local dipoles near the boundary. This observation forms the foundation for the PDF method to differentiate the local and background field. The performance of the PDF method was validated in a numerical simulation and a phantom experiment and was applied to human brain MRI.

3.3 Theory: Approximate Dipole Field Orthogonality and Projection Theorem

For a given ROI, the local field f_L is defined as the magnetic field generated by the susceptibility distribution χ_L inside a region of interest M, and the background field f_B is defined as the magnetic field generated by the susceptibility distribution χ_B in the region $\bar{M}$, which is outside the ROI and inside a sufficiently large FOV. Note that the background field extends into the ROI, just as the local field extends outside the ROI. For human MRI, tissue susceptibility satisfies $|\chi|<<1$, making the magnetic fields generated by human tissue susceptibility variation orders of magnitudes smaller than the main field. Taking this into account, the total magnetic field is written as:

$$f = f_L + f_B = d \otimes (\chi_L + \chi_B). \quad [3.1]$$

Here, the symbol $\otimes$ denotes convolution and d is the unit dipole field, which is the magnetic field created by a unit dipole at the origin with the Lorentz sphere correction (6,16-17).

Our proposed projection onto dipole fields (PDF) method is to project the total field measured in the ROI onto the subspace spanned by all the background unit dipole fields. This was inspired by the projection theorem in Hilbert space (18), which we review briefly here. Let T be an inner product space spanned by all unit dipole responses $\{d_{\boldsymbol{r}} \mid \boldsymbol{r} \in M \cup \bar{M}\}$, where $d_{\boldsymbol{r}}$ denotes the magnetic field induced by a unit dipole located at $\boldsymbol{r}$. Hence, the total field $f \in T$. The inner product between any $f_1, f_2 \in T$ is defined as the sum of element-wise multiplication between f_1 and f_2 inside the ROI only. Following Eq. 3.1, the background field component f_B is formed of basis functions $\{ d_{\boldsymbol{r}_B} \mid \boldsymbol{r}_B \in \bar{M}\}$, which represent fields created by background unit dipoles. The subspace spanned by all the background unit dipole fields is then denoted as B. Similarly, the basis functions of the local field component f_L are $\{ d_{\boldsymbol{r}_L} \mid \boldsymbol{r}_L \in M \}$ and the subspace spanned by all the local unit dipole fields is denoted as L. According to the projection theorem (18), $\text{argmin}_{f_B \in B} \| f - f_B \|_2$ has a unique value f_B^* , and $f - f_B^*$ is orthogonal to B; if $L \perp B$, then $f - f_B = f_L$ is orthogonal to B, so f_B^*obtained by the minimization is exactly f_B, the true background field. Therefore, we propose the PDF method that estimates the background field as:

$$\text{argmin}_{\chi_B \in \bar{M}} \| f - d \otimes \chi_B \|_2 . \quad [3.2]$$

To justify the use of the projection theorem for removing background field in MRI, we evaluated the orthogonality assumption using a typical brain ROI segmented from an actual brain scan (detailed in the following in vivo brain scan section). Orthogonality requires that for each given local unit dipole field, its inner product with any possible background unit dipole field is zero. Accordingly, we evaluated the correlation quantity $c(\boldsymbol{r}_L)$ defined as the maximum absolute normalized inner product between a given local field induced by a unit dipole at $\boldsymbol{r}_L \in M$ and any possible background unit dipole field:

$$0 \le c(r_L) = \max_{r_B \in \bar{M}} | <d_{\boldsymbol{r}_L}, d_{\boldsymbol{r}_B}> /(\|d_{\boldsymbol{r}_L}\|_2 \times \|d_{\boldsymbol{r}_B}\|_2) | \le 1 \qquad [3.3]$$

This maximum absolute normalized inner product $c(\boldsymbol{r}_L)$ is almost zero ($c(\boldsymbol{r}_L) << 0.1$) except for locations within 5 voxels from the boundary as demonstrated in the realistic brain ROI (Figure 3.1a-c). Therefore, the orthogonality between the background field subspace and the local field subspace may be considered a good approximation.

3.3.1 Error analysis

The approximate orthogonality does not guarantee that the local field will be perfectly recovered by the PDF method, but it does predict that large maximum absolute normalized inner products are likely to lead to greater errors in the estimated local field. To demonstrate the spatial dependence of error, the PDF method is performed on a simulated total field consisting of a single local unit dipole field $d_{\boldsymbol{r}L}$, $\boldsymbol{r} \in M$ and a zero background field to generate an estimated background field $f^*_{b,\boldsymbol{r}_L}$. The true background field is zero and therefore, the PDF method should ideally not remove any part of the

local field. Any residual $f^*_{b,\mathbf{r}_L}$ represents an error in the background field estimated by the PDF method, which is quantified by calculating the ratio between the norms of the error ($f^*_{b,\mathbf{r}_L} - 0$) and $d_{\mathbf{r}_L}$ over the ROI: $E(\mathbf{r}_L) = \|f^*_{b,\mathbf{r}_L}\|_2 / \|d_{\mathbf{r}_L}\|_2$. This relative error is visualized for every voxel $\mathbf{r}$ inside the ROI in Figure 3.1d-f. It is observed that the error is low (E<0.1) for dipoles located at most of the voxels in the ROI and increases for dipoles near the boundary of the ROI.

Figure 3.1. Approximate orthogonality between dipole fields.

For each local dipole inside the ROI, the maximum absolute normalized inner product between its field and any background unit dipole field is plotted in a) axial, b) coronal and c) sagittal section of a typical ROI in human brain MRI (same as in the later Figure 3.4 with resolution reduced to 80×60×46 matrix for practical computing time). The inner product values are close to zero at most voxels except for those near the boundary. The relative error (see text for definition) for each local dipole is shown in the d) axial, e) coronal and f) sagittal section.

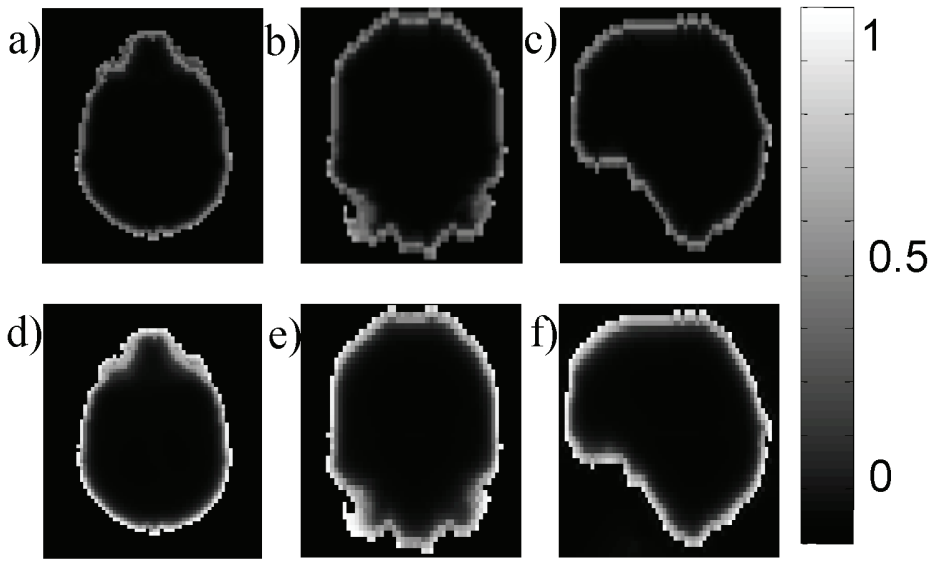

3.4 Methods and Materials

3.4.1 PDF algorithm implementation

The computation of the total field *f* from MR phase data was based on phase data from multiple echo data (2), followed by a magnitude image guided unwrapping algorithm (19). To correct for a large background field from potentially poor shimming, zeroth and first order spherical harmonic terms in the field expansion were estimated and removed from the measured total field using a weighted least square minimization (2,11). The corrected total field *f* was then used in all the following background removal methods.

We accounted for spatial variations of noise in the MR field maps by adding a weight to Eq. 3.2 to normalize the noise to a normal distribution $N(0,1)$. The weight w was derived from magnitude images across multiple echoes (5). The resulting minimization becomes:

$$\chi_B^* = \text{argmin}_{\chi_B} \|w\cdot(f - d \otimes \chi_B)\|_2, \qquad [3.4]$$

where the norm $\|.\|_2$ in Eq. 3.4 is again calculated only over the ROI M, which may be defined using image segmentation, and the dot symbol indicates point-wise multiplication between vectors.

We let N be the number of voxels in the MR image dataset, and expressed the measured total field f and the total susceptibility distribution χ as $N\times1$ column vectors. Let I be an $N\times N$ identity matrix and M an $N\times N$ diagonal matrix, where the diagonal elements are equal to 1 when they correspond to voxels inside the ROI and are equal

to zero otherwise. Then the background susceptibility was written as $\chi_B = (I - M)\chi$. D denotes an $N \times N$ matrix representing the convolution with the unit dipole field d and W denotes an $N \times N$ diagonal matrix formed by placing the weighting w on the diagonal. With this notation, the minimizer in Eq. 3.4 was found by solving (18):

$$MWD(I-M)\chi = MWf. \quad [3.5]$$

In a typical high resolution 3D brain MRI dataset with $N>10^6$ voxels, D has more than 10^{12} elements, which is impossible to explicitly form and store in computer memory. Therefore, a conjugate gradient algorithm (CG) was used in which the convolution is efficiently calculated in the Fourier domain (13-14,20-21). The forward system on the left hand side of Eq. 3.5 was made positive semi-definite by applying the Hermitian conjugate of the matrix $A=MWD(I-M)$ to both sides of Eq. 3.5 (22):

$$A^H A\chi = A^H \beta, \quad [3.6]$$

where $\beta=MWf$. The CG iteration was stopped when the norm of the residual was smaller than 50% of the expected noise level $||A^H Mu||_2$, where u was a column vector containing ones. Once $\chi^*$was estimated, the background field was calculated as:

$$f_B^* = D\chi_B^* = D(I\text{-}M)\chi^*, \quad [3.7]$$

and was subtracted from the measured total field f to estimate the local field f_L^*.

3.4.2 Comparison with High-Pass filtering

In this study, the PDF method was compared with the high-pass filtering (HP) that has been commonly used in literature. In HP, a 3D Hann window low-pass filter with

kernel size of 32×32×32 was applied to the complex MRI data when one echo was used (10). When multiple echoes were acquired, the low-pass filter was applied to a reconstructed complex MRI data set formed by setting the magnitude equal to that of the first echo and the phase equal to the unwrapped total field normalized to $[-\pi,\pi)$. The background field was estimated from the phase of the resulting low-pass filtered complex image. All the algorithms were implemented on a personal computer with Intel® Core™ i7 CPU, 6GB memory using MATLAB (2009a) code (MathWorks, Natick, MA, USA).

3.4.3 Validation of background field removal methods

The reference scan method (2,7) can be used to estimate the local field without any algorithmic bias in both numerical simulation and phantom experiments, and served as the gold standard for evaluating any background field removal method, including the proposed PDF method.

3.4.3.1 Numerical simulation

An ellipsoid whose radii were 40, 40 and 54 voxels was created in a 160×160×160 matrix to imitate the shape of a head. Five smaller ellipsoids were created inside the head-shape ellipsoid to simulate mastoid cavities, ethmoid and maxillary sinuses. The radii of these ellipsoids ranged from 10 to 15 voxels. Three cylinders with a radius of 2 voxels and a length of 20 voxels were created to simulate veins and were placed inside the head shape ellipsoid along the x, y and z directions, respectively. A sphere with a radius of 5 voxels was created in the mid-brain to mimic a hemorrhage. Complex MRI data was simulated from this geometry. A uniform intensity of 100 was

assigned to the “head” region, while the “air” cavities were assigned zero. Susceptibility in the “head” region was chosen to be the zero reference, the susceptibility of “air” was 9.4parts per million (ppm) (2), the vessels were 0.3ppm (9), and the hemorrhage was 1.2ppm (3). The total field was calculated using a forward calculation (14,20-21). The reference background field was obtained by repeating the total field calculation in the same numerical phantom but with the vessels and the hemorrhage removed. The phase image was calculated from the total field by assuming a TE=30ms and a scanner field strength B0 equal to 1.5T. Zero-mean Gaussian white noise with a standard deviation of 1 was added to both the real and imaginary parts of the complex images independently. Noise was not added to the reference scan. Finally, an 80×80×80 volume in the upper middle part was cropped from the 160×160×160 matrix to emulate a prescribed FOV that narrowly encompasses the brain (Figure 3.2a-d). The 80×80×80 matrix was then used for the subsequent simulations. The total field, the reference background field, and the reference local field (obtained by subtracting the reference background field from the total field) are shown in Figure 3.2a-c. An ROI M was chosen as the “air-free” region (white regions in Figure 3.2d) and $\bar{M}$ was the “air” region (black regions in Figure 3.2d). Estimated background fields were then calculated using both techniques, and subtracted from the total field to generate the estimated local fields. For quantitative comparison, relative errors of the background field were calculated to assess the goodness of the background removal. Relative errors were calculated by taking the norm of the difference between the estimated background field and the reference background field, and then normalized by the norm of reference background field. The norms were calculated inside the ROI only. The attenuation of the local field due to

the background removal processes was calculated as one minus the ratio between the norm of the estimated local field and the norm of the reference local field. The norms were calculated inside a manually defined rectangular volume comprising the susceptibility sources of interest to capture the local attenuation of the local field while ignoring the amplification elsewhere, e.g. near the boundary of the ROI.

3.4.3.2 Phantom MRI experiment

A cylindrical water phantom (diameter = 10 cm, height = 8.5cm) was constructed. Three vials (diameter = 1.2cm, height = 6cm) with 1% concentrated gadolinium (Gd; Magnevist, Berlex Laboratories, Wayne, NJ, USA) were placed vertically in the water container to mimic three vessels. A waterproof plastic air box (2.5×2.5×1.5cm3) was glued to the bottom of the water container to imitate an air cavity. The phantoms were scanned on a 1.5T clinical MRI scanner (General Electric Excite HD; GE Healthcare, Waukesha, WI, USA) using a 5-inch surface coil for signal reception. A dedicated 3D gradient-echo sequence was designed to sample at different TEs in an interleaved manner. Scanning parameters were: FOV 15×15×10 cm3, matrix size = 150×150×100, bandwidth ±62.50 kHz, TR 30ms, and flip angle 30°. Four TEs (1.7, 2.2, 4.2 and 14.2ms) were used to achieve a balance between the precision of the estimated total field and the total scan time. After this scan was completed, the three vials were removed from the water phantom. The scan was repeated with identical imaging parameters to acquire a reference background field. The scanner gradient shimming was kept constant between the two scans. The background air region without MR signal was segmented as $\bar{M}$ (background black region in Figure 3.3d), and the rest was denoted as M. Noise was estimated from $\bar{M}$. Similar to the numerical simulation,

estimated background fields were compared qualitatively and quantitatively with the reference background field.

3.4.3.3 In vivo brain scan

This study was approved by our institutional IRB. In vivo MRI was performed on 15 patients with histories of hemorrhagic stroke on a 3T clinical MRI scanner (General Electric Excite HD; GE Healthcare, Waukesha, WI, USA). Standardized data acquisition and data processing were performed on all the patients in the following manner. Data were acquired using an eight channel head coil and a multiple echo spoiled gradient echo sequence with 3D flow compensation. Imaging parameters were TE=3.5, 7, 10.5, 14, 17.5 21ms, TR=40 ms, slice thickness=2 mm, flip angle = 15º, number of slices = 70 axially through the brain. The imaging matrix was 240×180×70, with a pixel bandwidth of 520 Hz per pixel and a FOV of 24×18×14cm3. The phase images were used to fit the total field. The brain region was segmented and denoted as the ROI M while the remaining regions in the imaging volume were considered to comprise $\bar{M}$. Estimated background fields were obtained and removed using both techniques. The 3D brain data was reformatted to coronal sections for inspection. To quantitatively assess the improvement of the PDF method, field contrasts were calculated from PDF and HP processed field maps. Rectangular volumes immediately superior to the hemorrhages and volumes on the right of the hemorrhages were drawn, and the difference between the mean values insides these two regions were calculated, respectively. These two regions fall inside two lobes of the dipole field that have opposite signs. The resulting contrast measurements were compared between the HP and the PDF method over the 15 patients using a two tailed paired t test with

significance level p=0.01.

3.5 Results

The results of the numerical simulation are shown in Figure 3.2. The PDF method successfully removed the background field, leaving the local fields from "veins" and the "hemorrhage" intact, leading to the distinct dipole pattern in the local field (Figure 3.2g). There was little discernable visual difference between the local field estimated by the PDF method and the reference local field (Figure 3.2h). In contrast, the high-pass filtering (HP) left substantial residual background field in regions close to the "ethmoid sinus" and "mastoid cavities" (Figure 3.2j) and indiscriminatingly removed the slowly varying component of the field induced by the "hemorrhage" (Figure 3.2i&k, arrows). The relative errors between the estimated and the reference background field were 23.51% and 3.21% for the HP and PDF methods, respectively, and the attenuation of the local fields were 41.1% and 1.2%. The CG algorithm of the PDF method converged with 10 iterations in 0.7s.

The results for the phantom experiment are shown in Figure 3.3. The estimated background field by the PDF method was in good agreement with the reference background field (Figure 3.3h) while the estimated background field by the HP method contained substantial amount of the local field (Figure 3.3i&k, arrow). The relative errors between the estimated and the reference background field were 18.36% and 5.53% for the HP and PDF methods, respectively, and the attenuation of the local fields were 43.0% and 3.2%. The CG algorithm of the PDF method converged with 43 iterations in 17.0s.

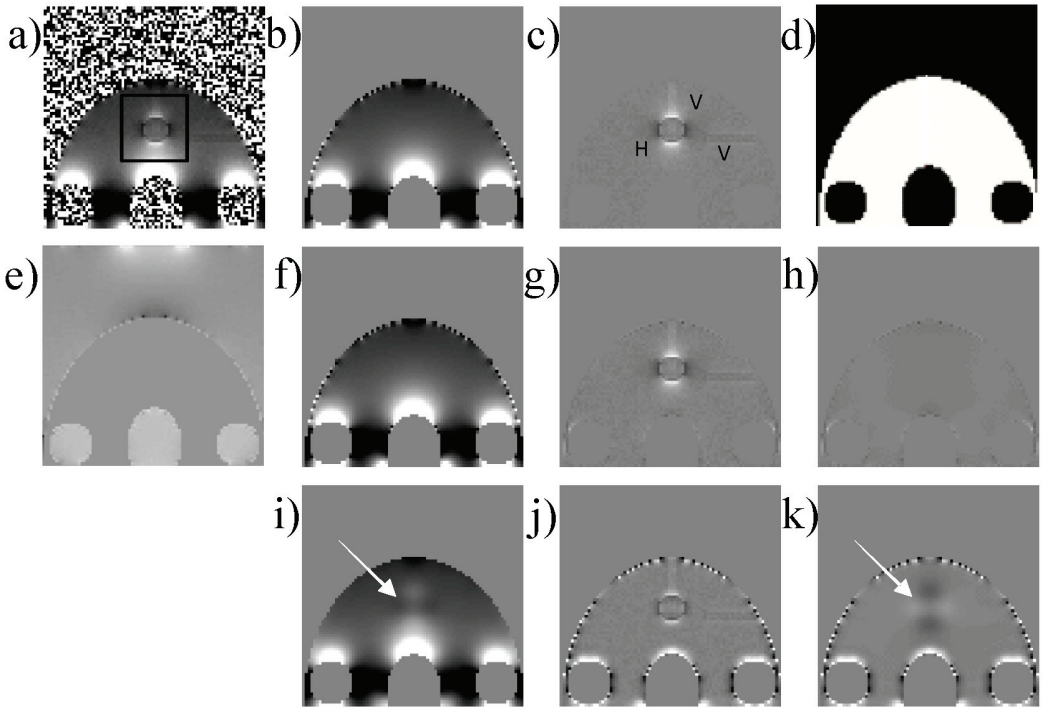

Figure 3.2. Validation in numerical simulation.

The numerical brain phantom is shown in a prescribed FOV in coronal view with a) the simulated total field, b) the corresponding reference background field, c) the reference local field with annotated hemorrhage (H) and veins (V), and d) the defined ROI (white area). The PDF method is used to estimate e) the background susceptibility distribution. f) The PDF estimated background field, g) the PDF estimated local field and h) the corresponding difference with the reference showed substantial improvement over the HP method (i, j and k, corresponding HP estimated background field, estimated local field and the difference with reference). The relative errors were 23.51% and 3.21% for the HP and PDF methods, respectively. The black box in a) indicates the region where the attenuation of the local field is measured.

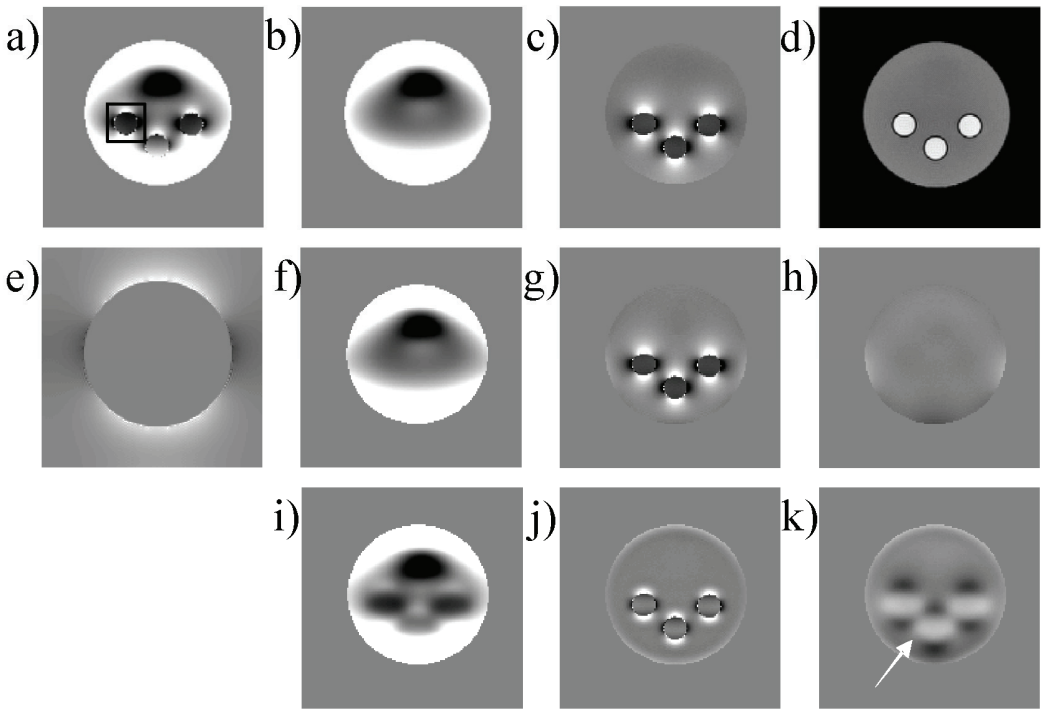

Figure 3.3. Validation in phantom MRI.

Acquired 3D data were shown in a coronal section with a) the total field, b) the corresponding reference background field, c) the reference local field and d) the magnitude image (with the large circular disk as ROI). The PDF method is used to estimate e) the background susceptibility distribution. f) The PDF estimated background field, g) the PDF estimated local field and h) the corresponding difference with the reference showed substantial improvement over the HP method (i, j and k, corresponding HP estimated background field, estimated local field and the difference with reference). The relative errors were 18.36% and 5.53% for the HP and PDF methods, respectively. The black box in a) indicates the region where the attenuation of the local field is measured.

Hemorrhages were found in all patients, with an example illustrated in Figure 3.4. Compared to the estimated local field by the PDF method (Figure 3.4f), the estimated local field by the HP method contained substantially more field variation at the periphery of the brain ROI, which might be interpreted as high spatial frequency residual background field due to the air-tissue interface (Figure 3.4h, white arrow). The strength of the estimated local fields arising from the hemorrhagic lesion by the PDF method was stronger than that by the HP method (black arrows), resulting in a better contrast in the field maps between the hemorrhage and the surrounding tissue by the PDF method. Quantitatively, the PDF processed image has higher field contrast than the HP processed image for each of the 15 cases (21±8Hz vs. 12±5 and $p<0.001$).

3.6 Discussion

Our preliminary data demonstrate that this non-parametric background removal technique, projection onto dipole fields (PDF), is successful in removing the background field while allowing an accurate estimation of the local field. Compared to the high-pass filtering (HP) method, the PDF method estimates the background fields with smaller errors and results in less attenuation of the local field with respect to the reference scan method in a numerical simulation and a phantom experiment. The PDF method provides superior local field maps for in vivo brain imaging with less artifacts near tissue-air boundaries and more contrast in local fields induced from different brain structures.

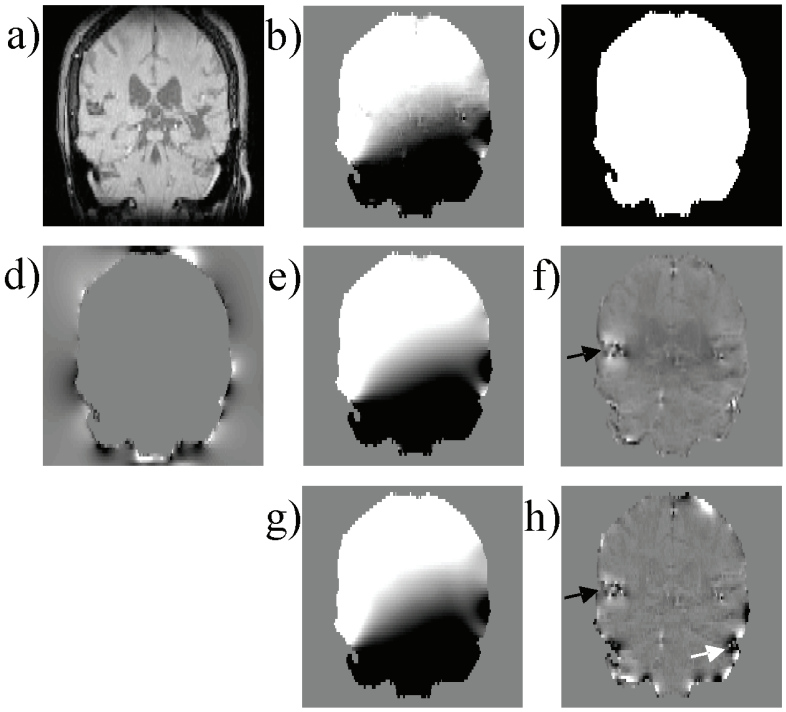

Figure 3.4. Patient brain imaging.

Acquired 3D data were shown in a coronal section with a) magnitude image, b) the total field, and c) the ROI (white region). d) Estimated background susceptibility distribution using the PDF method; e&f) the background and local field estimated by the PDF method; g&h) the background and local field estimated by the HP method. The estimated local field generated by the PDF method provides better depiction of the hemorrhage (black arrows) with a higher visual contrast between the hemorrhage and the surrounding tissue and with less artifacts (white arrow).

The HP method performs background removal using the Fourier bases. The HP method does not distinguish the source of the slowly varying components of the total field, either from the background or from the ROI. Hence, HP suffers when there are overlaps between the Fourier spectra of the background and local fields. In general, the background field may contain high-spatial frequency components and the local

field may contain low-spatial frequency components. Consequently, the HP method may fail to remove the high-spatial frequency components of the background field near air tissue boundaries in brain imaging (Figure 3.4h, white arrow), and may erroneously remove the low-spatial frequency components of the local field as demonstrated in Figure 3.3i where the uniform local field inside the vials and slowly varying local fields outside the vials were removed. Therefore, the HP method might not be suitable for visualizing local fields of large brain structures such as basal ganglia or hemorrhage and brain structures near the brain ROI boundary. In addition, it has also been convincingly demonstrated that the results of the HP method depend on the choice of the kernel size (10-11,15). Increasing the kernel size can improve removing unwanted background field, but at the cost of attenuating the local field.

The advantage of the PDF method over the HP method lies in the fact that there is substantial separation in the dipole field representations of the background and local fields, as measured by their approximate orthogonality (Figure 3.1). According to the dipole equation (17), the strength of a dipole field decays on the order of r^3 with r being the distance to the dipole, so the impact of the dipole is strong within its immediate vicinity and diminishes rapidly. Hence, if a local and a background dipole are far away in space, their spatial overlap as measured by the normalized inner product is very small. The separation between local and background fields may be fundamentally explained by Maxwell's Equation, which states that the field generated by the background dipoles is a harmonic function inside the region of interest, but the field generated by the local dipoles is non-harmonic (23). Therefore, the background and local fields may be separable in an ideal harmonic function space. In the PDF

method, the estimated background field generated by background dipoles is guaranteed to be a harmonic function. In comparison, the estimated background field by the HP method may violate the harmonic condition. Recently, Schweser et al. (24) presented a background removal technique that exploits the mean value property of harmonic functions. A full comparison between this method and the proposed PDF method is beyond the scope of the manuscript but is the subject of ongoing research. The projection of the measured field on to a subspace generated by dipoles was also used by Wharton et al (15), where 300 dipoles were manually positioned around the ROI.

This approximate orthogonality property provides a reasonable separability between the background and the local fields as demonstrated in experimental results reported here. The PDF method's applicability to general MRI may be confirmed by evaluating the correlation quantity (Eq. 3.3) for a desired ROI shape numerically. This separability holds very well for the interior of the ROI (Figure 3.1), making it very useful for brain imaging where most of the strong susceptibility sources caused by brain iron deposits tend to be located deeper inside the brain. The PDF method also performed better than the HP method (Figure 3.2h&k, Figure 3.3h&k, Figure 3.4f&h) near the ROI boundary, where the PDF performance may be further improved by means such as dilating the ROI by a few voxels to convert voxels near the original ROI boundary into interior points of the enlarged ROI.

Because a given magnetic field may arise from many susceptibility distributions due to the non trivial null-space of the dipole kernel convolution (25), the intermediate background susceptibility distribution estimated during the PDF process may not

correspond to the actual susceptibility distribution outside the ROI (Figure 3.2e, Figure 3.3e, Figure 3.4d). However, this does not affect the final calculation of the background field, which is our sole concern here. For instance, the Fourier aliasing in Figure 3.2e (visible as the two white regions near the top of the FOV) is not a problem: its presence effectively modeled the background field at the bottom of the FOV that was in reality caused by susceptibility sources further below the FOV.

3.7 Conclusion

In this study, we have proposed a non-parametric technique that removes the background field from the measured total field in an ROI by projecting the total field inside that ROI to the fields generated by dipoles outside the ROI. This novel projection onto dipole fields (PDF) method was validated in numerical simulation and phantom study and was demonstrated to be applicable for *in vivo* human brain imaging.

3.8 Acknowledgement

This investigation was supported in part by grant R01HL064647, R01HL062994 and UL1RR024996 of the Clinical and Translation Science Center at Weill Cornell Medical College.

3.9 Reference

1. Haacke EM, Xu Y, Cheng YC, Reichenbach JR. Susceptibility weighted imaging (SWI). Magn Reson Med 2004;52(3):612-618.

2. de Rochefort L, Brown R, Prince MR, Wang Y. Quantitative MR susceptibility mapping using piece-wise constant regularized inversion of the magnetic field. Magn Reson Med 2008;60(4):1003-1009.

3. de Rochefort L, Liu T, Kressler B, Liu J, Spincemaille P, Lebon V, Wu J, Wang Y. Quantitative susceptibility map reconstruction from MR phase data using bayesian regularization: validation and application to brain imaging. Magn Reson Med 2010;63(1):194-206.

4. de Rochefort L, Nguyen T, Brown R, Spincemaille P, Choi G, Weinsaft J, Prince MR, Wang Y. In vivo quantification of contrast agent concentration using the induced magnetic field for time-resolved arterial input function measurement with MRI. Med Phys 2008;35(12):5328-5339.

5. Kressler B, de Rochefort L, Liu T, Spincemaille P, Jiang Q, Wang Y. Nonlinear Regularization for Per Voxel Estimation of Magnetic Susceptibility Distributions From MRI Field Maps. IEEE Trans Med Imaging 2009.

6. Li L, Leigh JS. Quantifying arbitrary magnetic susceptibility distributions with MR. Magnetic Resonance in Medicine 2004;51(5):1077-1082.

7. Liu T, Spincemaille P, de Rochefort L, Kressler B, Wang Y. Calculation of susceptibility through multiple orientation sampling (COSMOS): a method for conditioning the inverse problem from measured magnetic field map to susceptibility source image in MRI. Magn Reson Med 2009;61(1):196-204.

8. Shmueli K, de Zwart JA, van Gelderen P, Li TQ, Dodd SJ, Duyn JH. Magnetic susceptibility mapping of brain tissue in vivo using MRI phase data. Magn Reson Med 2009;62(6):1510-1522.

9. Fernandez-Seara MA, Techawiboonwong A, Detre JA, Wehrli FW. MR susceptometry for measuring global brain oxygen extraction. Magn Reson Med 2006;55(5):967-973.

10. Wang Y, Yu Y, Li D, Bae KT, Brown JJ, Lin W, Haacke EM. Artery and vein separation using susceptibility-dependent phase in contrast-enhanced MRA. J Magn Reson Imaging 2000;12(5):661-670.

11. Langham MC, Magland JF, Floyd TF, Wehrli FW. Retrospective correction for induced magnetic field inhomogeneity in measurements of large-vessel hemoglobin oxygen saturation by MR susceptometry. Magn Reson Med 2009;61(3):626-633.

12. Yao B, Li TQ, Gelderen P, Shmueli K, de Zwart JA, Duyn JH. Susceptibility contrast in high field MRI of human brain as a function of tissue iron content. Neuroimage 2009;44(4):1259-1266.

13. Neelavalli J, Cheng YC, Jiang J, Haacke EM. Removing background phase

variations in susceptibility-weighted imaging using a fast, forward-field calculation. J Magn Reson Imaging 2009;29(4):937-948.

14. Koch KM, Papademetris X, Rothman DL, de Graaf RA. Rapid calculations of susceptibility-induced magnetostatic field perturbations for in vivo magnetic resonance. Phys Med Biol 2006;51(24):6381-6402.

15. Wharton S, Schafer A, Bowtell R. Susceptibility mapping in the human brain using threshold-based k-space division. Magn Reson Med 2010;63(5):1292-1304.

16. Haacke EM, Brown RW, Thompson MR, R V. Objects in external fields: the Lorentz sphere. Magnetic resonance imaging: physical principles and sequence design: New York: Wiley-Liss; 1999. p 749-757.

17. Jackson JD. Classical electrodynamics, third edition: John Wiley and Sons, inc.; 1999.

18. Moon TK, Stirling WC. Pseudoinverses and the SVD. Mathematical Methods and Algorithms for signal processing: Prentice Hall; 2000. p 116-117.

19. Cusack R, Papadakis N. New robust 3-D phase unwrapping algorithms: application to magnetic field mapping and undistorting echoplanar images. Neuroimage 2002;16(3 Pt 1):754-764.

20. Marques JP, Bowtell R. Application of a Fourier-based method for rapid calculation of field inhomogeneity due to spatial variation of magnetic susceptibility. Concepts in Magnetic Resonance Part B: Magnetic Resonance Engineering 2005;25B(1):65-78.

21. Salomir R, De Senneville BD, Moonen CTW. A fast calculation method for magnetic field inhomogeneity due to an arbitrary distribution of bulk susceptibility. Concepts in Magnetic Resonance Part B-Magnetic Resonance Engineering 2003;19B(1):26-34.

22. Björck A, Björck Å. Iterative Methods For Least Squares Problems. Numerical methods for least squares problems: Society for Industrial Mathematics; 1996. p 269-270, 290-292.

23. Li L, Leigh JS. High-precision mapping of the magnetic field utilizing the harmonic function mean value property. J Magn Reson 2001;148(2):442-448.

24. Schweser F, Lehr BW, Deistung A, Richenbach JR. A Novel Approach for Speration of Background Phase in SWI Phase Data Utilizing the Harmonic Function Mean Value Property. 2010; Stockholm, Sweden. Proc. Intl. Soc. Mag. Reson. Med. p 142.

25. Haacke EM, Cheng NY, House MJ, Liu Q, Neelavalli J, Ogg RJ, Khan A, Ayaz M, Kirsch W, Obenaus A. Imaging iron stores in the brain using magnetic resonance imaging. Magn Reson Imaging 2005;23(1):1-25.

CHAPTER 4

4 CALCULATION OF SUSCEPTIBILITY THROUGH MULTIPLE ORIENTATION SAMPLING

4.1 Abstract

Magnetic susceptibility differs among tissues based on their contents of iron, calcium, contrast agent and other molecular compositions. Susceptibility modifies the magnetic field detected in the MR signal phase. The determination of an arbitrary susceptibility distribution from the induced field shifts is an inverse problem that is challenging due to its ill-posedness. A method for Calculation Of Susceptibility through Multiple Orientation Sampling (COSMOS) is proposed to stabilize this inverse problem. The field created by the susceptibility distribution is sampled at multiple orientations with respect to the polarization field B_0, and the susceptibility map is reconstructed by weighted linear least squares to account for field noise and the signal void region. Numerical simulations, phantom and *in vitro* imaging validations demonstrated that COSMOS is a stable and precise approach to quantify a susceptibility distribution using MRI.

4.2 Introduction

With the recent development of iron-based contrast agents and biomarkers for drug delivery (1) and molecular imaging (2), a robust technique to quantify iron content has become an increasingly important need. Iron oxides as well as other magnetic biomarkers may be mapped in MRI by identifying the corresponding susceptibility distributions that modify the MR signal. Indeed, susceptibility has been investigated to

reveal information about oxygen saturation level in blood, and to measure calcium or iron concentration in tissue, especially in the brain and bone (3-8). Therefore, there has been a major interest in quantifying susceptibility in MRI in general as it could lead to a unique quantitative tool and provide a novel contrast mechanism.

Quantifying arbitrary susceptibility distributions by inverting the measured magnetic field remains challenging because susceptibility inversion is intrinsically ill-posed (9). To circumvent this issue, several techniques have been proposed. Some of these techniques assume a uniform susceptibility distribution, or further require a well-defined geometric shape (3-5,10-12). A voxel-based inversion has been proposed assuming there are sufficient measurement points (13), but it is computationally intensive and no experimental work applying this technique has been published. The numerical difficulty may be sidestepped by recasting the inverse problem as an iterative model fitting problem, but such a solution underestimates susceptibility by 50% (14). The inverse problem is further complicated by the non-uniform noise in the field measurement and by the high phase noise in regions with strong susceptibility due to signal voids caused by T2* effects. An experimentally robust voxel-based susceptibility quantification of arbitrary distribution remains to be developed.

Here the ill-posed nature of this field to source inverse problem is analyzed and a novel method to stabilize the inversion by imaging the object at multiple orientations with respect to B_0 is presented. Theoretical considerations and experimental validations on various objects are shown to examine the robustness of this technique.

4.3 Theory

4.3.1 Relationship between Susceptibility and Magnetic Field

In the following, susceptibility refers to volume susceptibility. The spatially varying susceptibility distribution χ in an applied external uniform magnetic field changes the local field experienced by a spin in MRI. It can be shown from Maxwell magneto-static equations and the Lorentz correction for media effects that the susceptibility distribution affects the local field component along the main magnetic field B_0 according to

$$\delta_B(\boldsymbol{r}) = (1/4\pi)\int d^3\boldsymbol{r}' \, (3\cos^2\theta_{\boldsymbol{r}\boldsymbol{r}'} - 1)/|\boldsymbol{r}-\boldsymbol{r}'|^3 \chi(\boldsymbol{r}'), \qquad [4.1]$$

where $\boldsymbol{r}$ is the spatial coordinate vector, θ is the angle between $\boldsymbol{r}-\boldsymbol{r}'$ and the applied field, and δ_B is the relative difference field given by

$$\delta_B(\boldsymbol{r}) = (\underline{b_z}(\boldsymbol{r}) - B_0)/B_0, \qquad [4.2]$$

where $\underline{b_z}$ is the local magnetic field component along the main magnetic field (which coincides with the z direction) (9,13). The induced field may be interpreted as a convolution of the susceptibility distribution with a unit dipole response $(3\cos^2\theta\text{-}1)/4\pi|\boldsymbol{r}|^3$.

In Fourier domain, this convolution becomes a point-wise multiplication with a kernel (15,16)

$$\Delta_B(\boldsymbol{k}) = (1/3\text{-}k_z^2/k^2)X(\boldsymbol{k}), \qquad [4.3]$$

where Δ_B is the Fourier transform of the normalized field shift δ_B, X is the Fourier transform of χ and $(1/3\text{-}k_z^2/k^2)$ is the dipole response to an external magnetic field in the Fourier domain. k is the magnitude of a Fourier domain coordinate vector $\boldsymbol{k}$ and k_z is the projection of $\boldsymbol{k}$ onto the z-axis (the direction of the main magnetic field).

4.3.2 Inversion from Multiple Orientations

A direct point-wise division was suggested in (6) but is challenging to use in practice. The dipole response function $(1/3\text{-}k_z^2/k^2)$ has zeroes on two conic surfaces at the magic angle (≈54.7° from the main magnetic field). Directly inverting Δ_B to get X involves calculating $(1/3\text{-}k_z^2/k^2)^{-1}$ in the Fourier domain, which is not defined at those zeroes. If the imaging problem is appropriately discretized, the sampling points can be chosen to avoid the zeroes (6). However, the discrete problem is still ill-conditioned (17) as the dipole response in Fourier space may still be arbitrarily close to zero, resulting in severe noise amplification (18).

We propose to stabilize this inverse problem by rotating the object with respect to the main magnetic field and resampling the data. In the object's frame of reference, whose Fourier domain coordinate system is affixed with the object itself, Eq. 4.3 is therefore rewritten as

$$\Delta_B(\boldsymbol{k}) = (1/3\text{-}k_{zp}^2/k^2)X(\boldsymbol{k}), \qquad [4.4]$$

where k_{zp} is the projection of the object coordinate vector $\boldsymbol{k}$ onto the direction of the main magnetic field (Figure 4.1). Assume that, for simplicity of the derivations that follow, we limit ourselves to rotations of the object around the x-axis only. Then for a

α degree rotation, $k_{zp} = k_z \cos\alpha + k_y \sin\alpha$. Accordingly, if the object is sampled from N different angles, the multiple measurements can be used to determine the susceptibility value at a given location in Fourier space $X(\boldsymbol{k})$:

$$\begin{bmatrix} 1/3-k_{zp1}^2/k^2 \\ 1/3-k_{zp2}^2/k^2 \\ \cdots \\ 1/3-k_{zpN}^2/k^2 \end{bmatrix} \cdot X(\boldsymbol{k}) = \begin{bmatrix} \Delta_{B1} \\ \Delta_{B2} \\ \cdots \\ \Delta_{BN} \end{bmatrix}. \qquad [4.5]$$

A Fourier domain point-wise direct inversion is applicable as long as there exists a non-zero element among $(1/3-k_{zpn}^2/k^2)$, n=1, 2…N. A set of angles $\alpha_1,\ldots, \alpha_N$ exist to fulfill this criterion for every point in Fourier domain when N is greater than or equal to 3. A proof of this statement is provided in the appendix. There is also an intuitive explanation for the proof as illustrated in Figure 4.1c. The zeroes in the Fourier domain kernel make the inversion unstable, and preferably they should be eliminated. Sampling from two orientations is insufficient because the solid angle of each cone is greater than 90° ($\approx 2\times 54.7°$), leading to inevitable interceptions among the 4 zero-cone surfaces associated with any two-angle sampling. The intercept is a collection of lines through the Fourier domain origin. Sampling from a third angle may sample the Fourier domain points in those locations with a rotated dipole kernel away from zero. One special point that needs further attention is the Fourier domain origin because the kernel $(1/3-k_{zp}^2/k^2)$ is not defined at this point. However, the origin only defines a constant offset in the image and will not affect relative susceptibility differences, therefore in the inversion the Fourier domain origin is set to zero. The remaining issue is to determine the optimal sampling orientations.

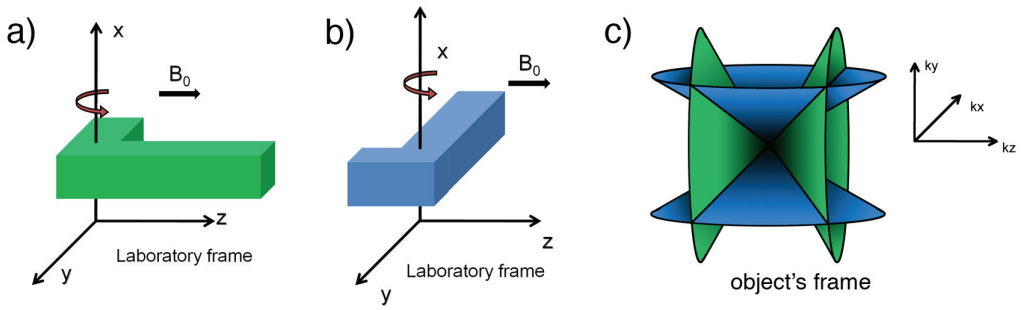

Figure 4.1. Determination of the minimum number of required rotations. a) The object is scanned at the first position. Then, the object is rotated around the x-axis. b) The scan is repeated at the second orientation. The rotation-scanning process repeats until the required number of rotations is reached. Subsequent rotations are not shown in this figure. c) The dipole response kernel function in the Fourier domain (fixed with respect to the object) has zeroes located on a pair of cone surfaces (the green pair for the first sampling and the blue pair for the second sampling). The presence of these zeroes makes the inversion extremely susceptible to noise and they need to be avoided when possible. Sampling from two orientations is insufficient because these two pairs of cone surfaces will still intercept, resulting in lines of common zeroes. Sampling from an appropriate third angle can eliminate all the common zeroes in the dipole kernels except the origin, which only defines a constant offset but does not change the relative susceptibility difference between tissues in the image.

4.3.3 Stability of Inversion and Optimal Sampling Orientations

Equation [5] may be used to solve independently for all points in the Fourier domain. However, if we want to minimize the upper bound of total error in X over the entire Fourier domain, all the points should be grouped together. Thus Eq. 4.5 is

reformulated into

$$CX = \Delta_B, \qquad [4.6]$$

where X is the vector representation of the all the $X(\boldsymbol{k})$, Δ_B is the vector representation of all the $\Delta_{Bn}(\boldsymbol{k})$ in Eq. 4.5, and C is a block diagonal matrix representing point-wise multiplication, in which each diagonal block is the corresponding left hand side vector in Eq. 4.5.

In analyzing error propagation in discrete inverse problems, a useful property to consider is the condition number. For a non-square but column full ranked matrix C, the condition number is defined as $\kappa(C)=\sigma_{max}/\sigma_{min}$, the ratio of the largest and smallest singular value of the matrix C. In the presence of noise, the actual measurement is given by $\Delta_{Bmeas} = \Delta_B+e\Delta_B$, where $e\Delta_B$ is a vector representation of the error in the measured data. When pseudo inverting the system, the hope is that $X_{inv} = X+eX = C^{+}(\Delta_B+e\Delta_B)$ is close to the true X, where eX is the error in the reconstructed that propagates from the measurement error, and $C^{+}=(C^{H}C)^{-1}C^{H}$ is the Moore-Penrose pseudoinverse of C . To analyze error propagation, $eX = C^{+}e\Delta_B$ must be bounded. The normalized error in the estimated X can be bounded as

$$\frac{||eX||_2}{||X||_2} \leq \frac{||e\Delta_B||_2}{||\Delta_B||_2}\cdot\left\{\frac{2\cdot\kappa(C)}{\cos\beta}+\tan\beta\cdot\kappa^2(C)\right\}+O\left[\left(\frac{||e\Delta_B||_2}{|\Delta_B||_2}\right)^2\right], \qquad [4.7]$$

where $\sin\beta=||CX-\Delta_B||_2/||\Delta_B||_2$ (18). From this equation, it is shown that the condition number directly determines the upper bound of relative error propagation, so it needs to be minimized for best performance.

Since the matrix C is already a block diagonal matrix whose blocks are column vectors, $C^H C$ is a diagonal matrix whose diagonal elements are

$\Lambda_{k_x, k_y, k_z}=\sum_{i=1}^{N}[1/3-(k_z\cos\alpha_i+k_y\sin\alpha_i)^2/k^2]^2$. Therefore, the singular values of C are

$\sigma_{k_x, k_y, k_z}=\sqrt{\Lambda_{k_x, k_y, k_z}}=\sqrt{\sum_{i=1}^{N}[1/3-(k_z\cos\alpha_i+k_y\sin\alpha_i)^2/k^2]^2}$ (19). Then the condition number for a particular set of sampling orientations $\{\alpha_n\}, n=1,2,...,N$ is

$$\kappa_{\alpha_1, \alpha_2,..., \alpha_N} = \frac{\max\limits_{k_x, k_y, k_z}\sqrt{\sum_{i=1}^{N}[1/3-(k_z\cos\alpha_i+k_y\sin\alpha_i)^2/k^2]^2}}{\min\limits_{k_x, k_y, k_z}\sqrt{\sum_{i=1}^{N}[1/3-(k_z\cos\alpha_i+k_y\sin\alpha_i)^2/k^2]^2}}. \quad [4.8]$$

The optimal sampling orientations are $\{\alpha^*_n\}=\text{argmin}_{\{\alpha_n\}, n=1,2,...,N}\kappa_{\alpha1, \alpha2..., \alpha N}$, $n=1,2,...,N$.

4.3.4 Noise Considerations

The field shift δ_B is calculated from MR phase images. The standard deviation of phase noise in a voxel is approximately inversely proportional to the signal intensity at that voxel (20). To account for this varying phase noise, the error between the measured data and the model needs to be minimized in a weighted least square manner. The goal is to find a susceptibility distribution X that satisfies

$$X^*=\text{argmin}_X||W\cdot F^{-1}(CX-\Delta_B)||_2 , \quad [4.9]$$

where symbol · denotes matrices point-wise multiplication, W is a weighting matrix that determines the penalty for deviation at a given measured point. The signal intensity map in image space can be conveniently used for constructing the weighting matrix.

A direct solution of Eq. 4.9 involves inverting a large matrix. For example, for an image with 100×100×100 unknown values and 3 acquisitions, the matrix is 3×10^6 by 10^6 , so direct inversion is computationally prohibitive. On the other hand, calculating the forward problem does not require explicitly forming such a large matrix, and can be greatly facilitated using the Fast Fourier Transform, allowing an iterative solution. Because the system is usually well-conditioned after over sampling using different orientations, the iterative method converges rapidly to a reasonable solution.

4.4 Materials and Methods

4.4.1 Optimal Sampling Orientations

An analytical solution of $\{\alpha^*_n\}$, $n = 1,2,...,N$ was not straightforward so a numerical simulation was conducted to search for the optimal angles. N was set to be the minimum required 3 in both simulation and experiments. Following the theory section, rotation is also limited in the y-z plane only. Without loss of generality and because of symmetry, the first angle α_1 was set to be 0°. The second angle α_2 increased from 0° to 180° with a 1° increment and α_2 increased from α_2 to 180° with a 1° increment as well. The Fourier domain kernel was generated by Eq. 4.6 and the condition number was calculated according to Eq. 4.8. Each dimension of k_x,k_y,k_z ranged from -16 to 15 with a step increment of 1. $\log(\kappa_{\alpha_2,\alpha_3})$ was plotted to identify

the smallest condition number and optimal sampling orientations.

4.4.2 Numerical Simulation

A matrix space of 128*128*64 voxels was used. The middle 10 slices (z=28~37) had susceptibility distributions in the shape of the Shepp-Logan phantom(21), whose highest value is one and smallest non-zero value is 0.2. The susceptibility of all other slices was set to zero. The direction of B_0 was constrained to the y-z plane. Sampling from only one angle, and sampling using the optimal set of angles found in the previous section were simulated using Eq. 4.4 to generate the field maps $\delta_B(\boldsymbol{r})$. Then, zero mean Gaussian white noise with a standard deviation of 0.01 was added to the simulated field maps.

4.4.3 MRI Experiments

4.4.3.1 Phantom preparation

Three experiments were conducted to validate this technique. The first experiment was susceptibility quantification of different concentrations of gadolinium (Magnevist, Berlex Laboratories, Wayne, NJ). A water phantom containing 5 vials with concentrations of gadolinium (Gd) ranging from 1% to 5% with 1% increment was constructed. The corresponding susceptibilities were expected to be linearly spaced from 1.63ppm to 8.15ppm (22). The second experiment was in vitro susceptibility mapping of bone. A section of bone was excised from the center part of a swine's thigh. The length of the bone was approximately 6.5cm and the diameter was 2.7cm. Bone marrow was removed prior to the scan. The entire bone was embedded in a 1.5%

agarose gel phantom. The third experiment was in vitro iron quantification in animal tissue. In this experiment, 10% concentrations of Feridex (Advanced Magnetics Inc., Cambridge, MA) solutions were injected into chicken breast muscle with volumes of 1μL, 2μL, 3μL and 4μL using a micro syringe. The iron-oxide density of 10% Feridex is 1.12μg/μL. The entire muscle was immersed in a water container.

4.4.3.2 Data Acquisition

All experiments were conducted on a 1.5T clinical MRI scanner (General Electric Excite HD, GE Healthcare, Waukesha, WI) using a 3inch or a 5inch surface coil for signal reception. The phantoms were rotated with respect to the magnetic field. After the first orientation was sampled, the phantom was rotated twice in the coronal plane using the optimal angles identified in the first section, and for each orientation the data acquisition was repeated. In order to obtain the best quantitative results, phantoms without the target objects but otherwise identical were also scanned. These reference scans were used to measure the field inhomogeneity induced by the phantom-air interface and field inhomogeneity. A dedicated 3D gradient echo sequence was designed to sample at different TEs in an interleaved manner. Fields of view were $10.8\times10.8\times8.6cm^3/10.0\times10.4\times12.8cm^3/7.0\times7.0\times3.8cm^3$ for Gd-water phantom, bone and tissue imaging, respectively. Resolutions were $1mm^3/1mm^3/0.5mm^3$. Bandwidth and TR were 62.50 kHz/62.50 kHz/31.25 kHz and 30ms/40ms/30ms. The flip angle was 30° for all three experiments. Four TEs were used for each scan to achieve a balance between the precision of the field map estimation and the total scan time: 1.7, 2.2, 4.2, 14.2ms/1.7, 2.2, 4.2, 14.2ms/3.0, 3.8, 5.4, 10.2ms.

4.4.3.3 Data Processing

Phase information was extracted from images. Because the first and the last TE are around 10ms apart, the phase of a voxel will wrap around if the field off-resonance frequency on that voxel is greater than 50Hz. Thus the phase needs to be unwrapped. By fitting the phase evolution, the field off-resonance frequency was estimated and converted to parts per million (ppm) by the following equation $\delta_{\text{ppm}} = \delta f / \gamma B_0 \times 10^6$, where γ is the gyromagnetic ratio and δf is the off-resonance frequency. Afterwards, a manual image registration was performed to place the phantoms in a consistent location across rotations. Hence, all subsequent calculations were done in the same frame of reference. Reference scans were subsequently subtracted from the field maps to obtain δ_B. A mask was created by removing voxels whose intensities were less than 10% of the maximum intensity. The weighting matrix W was taken as the intensity map point-wise multiplied by the mask. An algorithm for sparse linear equations and sparse least squares (LSQR) was used to solve this minimization problem (23). The maximum number of iterations was set to 30.

Susceptibility values were measured on the reconstructed images. In a central slice of the Gd-water image, each vial and the surrounding water area were selected as Regions of Interest (ROIs). Susceptibility was measured as the mean values in these ROIs. Estimated susceptibilities versus expected susceptibilities were also plotted. For bone reconstruction, a threshold equal to -1 was placed on the reconstructed susceptibility images to delineate the geometry of the bone for measuring the mean and standard deviation of bone susceptibility. On the reconstructed susceptibility image of animal tissue, a simple threshold was used to segment Feridex regions. The

mean susceptibility value of the background (chicken muscle) was subtracted from the Feridex regions. Susceptibility was converted to iron-oxide density by the conversion factor $\chi_{\text{Feridex}}/\rho = \mu_0 M_{\text{Fe}}(B_0)/B_0 = 64.7\text{ppm } \mu\text{L}/\mu\text{g}$, where μ_0 is the vacuum permeability. $M_{\text{Fe}}(B_0)$ denotes the magnetization of the compound at B_0 expressed in electromagnetic units per gram, which was reported to be $77.3\text{emu}\cdot\text{g}^{-1}$ (24). The iron-oxide mass of each injection was integrated over each iron-oxide (Feridex) region.

4.5 Results

4.5.1 Optimal Sampling Orientations

The results of the simulation to determine the optimal orientations are shown in Figure 4.2. The smallest condition number is 2.031 and the corresponding optimal sampling orientations are . This is consistent with the intuition that uniformly distributed orientations perform best because sampling directions should be cylindrically symmetric to the anterior-posterior direction.

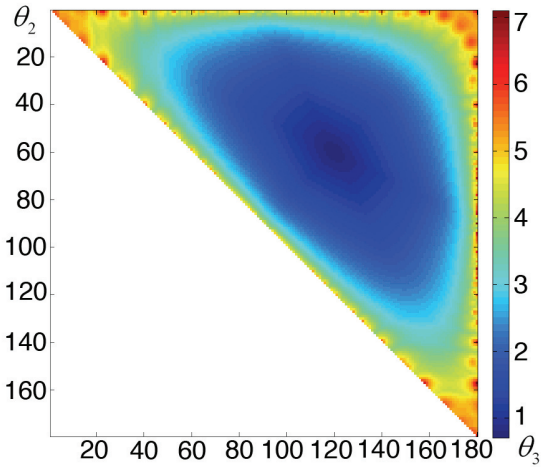

Figure 4.2. Color map of the matrix condition number

The vertical axis represents α_2 while the horizontal axis represents α_3 (see text for notation). Colormap is in log-scale for display purpose. The optimal angle combination was found on this map to be at (0°, 60°, 120°) .

4.5.2 Numerical Phantom

Images are shown in Figure 4.3. Inverting the dipole field using only one orientation yielded results that cannot be interpreted (Figure 4.3c). In contrast, inverting from 3 orientations returned satisfactory results (Figure 4.3d). The distracting streaking artifact at the magic angle (54.7°) that is often associated with susceptibility reconstruction was not observed (6,14). The error between the reconstructed and true susceptibility has a mean value of 4.62×10^{-3}, which is negligible compared to the value of the true susceptibilities.

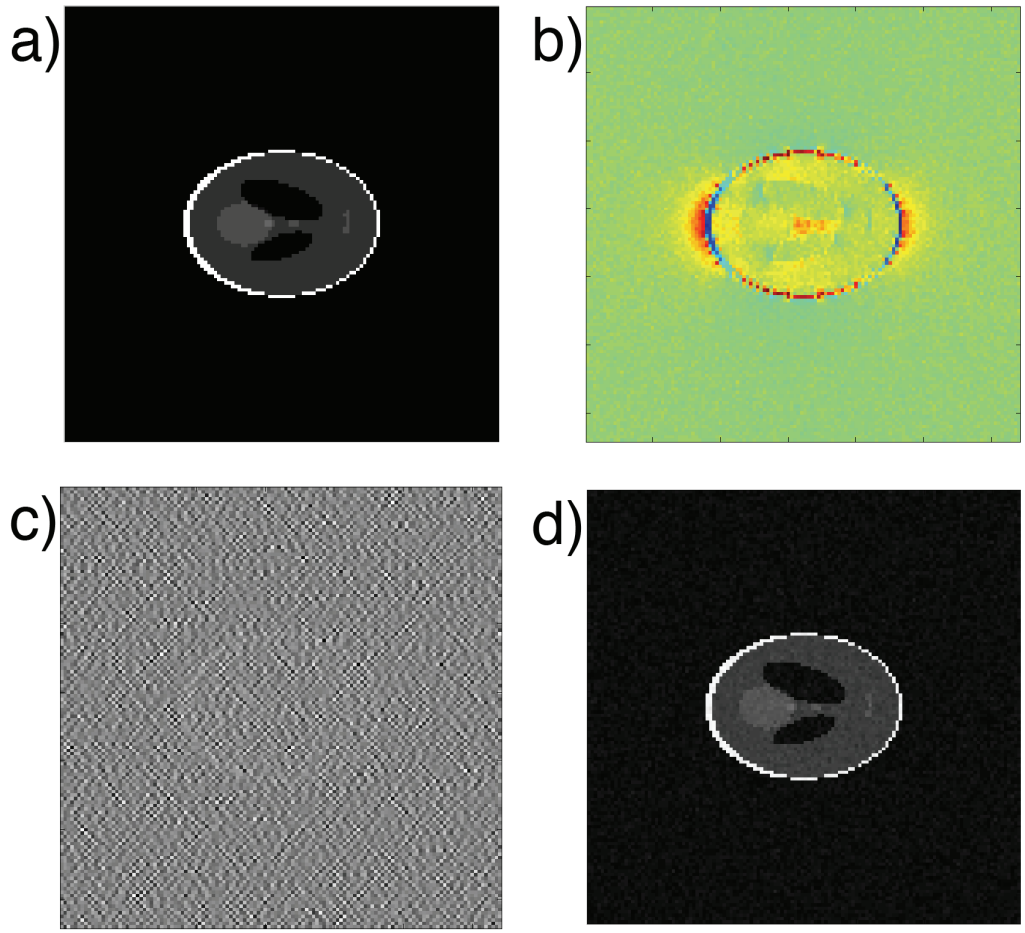

Figure 4.3. Numerical simulation of susceptibility inversion.

(a) True susceptibility distribution. (b) Simulated δ_B with noise. (c) Reconstructed susceptibility map from one orientation with direct Fourier domain division. (d) Reconstructed susceptibility map from three orientations.

4.5.3 Experimental results

The 3D images for the three experiments were successfully reconstructed with 30 iterations and each took less than 10 minutes on a Pentium 4 personal computer with

3GB of memory using MATLAB (MathWorks, Natick, MA).

Figure 4.4. Gd-water phantom experiment

(a) Magnitude of the gradient echo image of the Gd-Water phantom. Note that different concentrations of Gd have similar intensities. (b) δ_B of Gd-water phantom. Strong noise is seen on both the background air region, and the glass wall (indicated by red arrows). (c) Reconstructed susceptibility map from three orientations. (d) Graph displaying estimated susceptibility versus expected susceptibility.

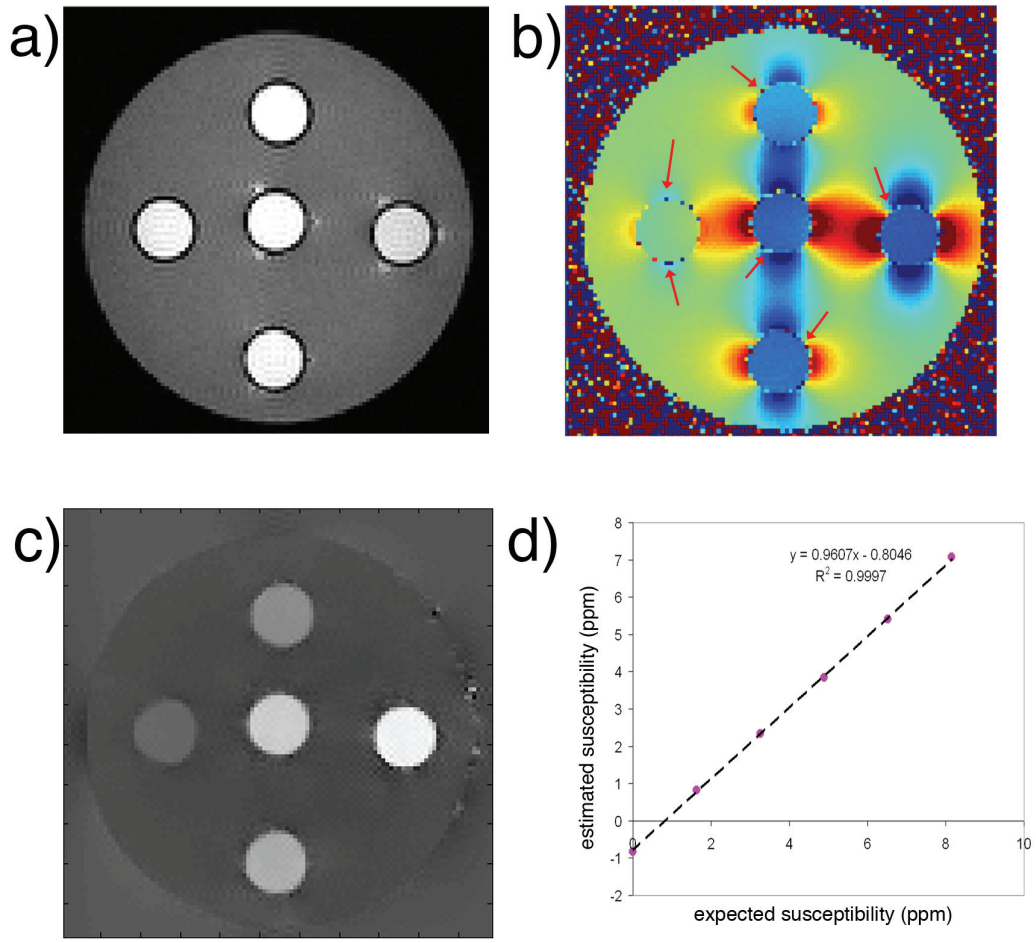

4.5.3.1 Gadolinium Susceptibility quantification

The measured δ_B in Figure 4.4b shows a conspicuous dipole pattern surrounding the vials with different gadolinium concentrations. COSMOS provided satisfactory images (Figure 4.4c). Different Gd concentrations were clearly resolved and no streaking artifacts were observed. The relation between estimated and expected susceptibility is plotted in Figure 4.4d. The result fits well with the linear model (R^2=0.9997), and provides a fair estimation of susceptibility (slope is 0.96, close to unity).

4.5.3.2 In vitro Bone Imaging

Figure 4.5a shows a gradient echo image obtained from the bone phantom and Figure 4.5c is the corresponding susceptibility reconstruction. Compact bone susceptibility was found to be -2.44±0.89ppm relative to water. This susceptibility value is in fair agreement with previous *in vitro* work (-2.39 ppm) (7).

Figure 4.5. In vitro bone experiment

(a) Magnitude of the gradient echo image of the bone-gel phantom. (b) δ_B of bone-gel phantom. (c) Reconstructed susceptibility map from three orientations.

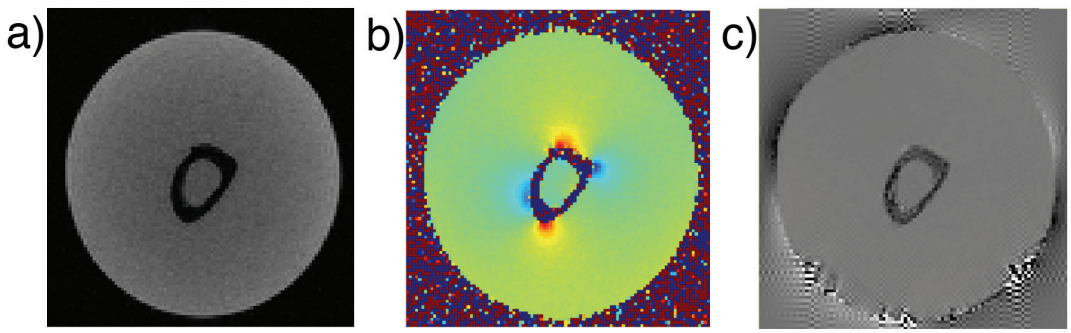

4.5.3.3 In vitro Iron Quantification in Animal Tissue

A representative slice is shown in Figure 4.6c. The bright regions corresponding to the 2μL, 3μL and 4μL iron-oxide injections are visible on this image (1μL region not shown in this slice). Measured iron mass are 1.23μg, 2.09μg, 3.32μg and 4.34μg. The relation between estimated and expected total magnetic moment is plotted in Figure 4.6d. Again, this result fits the linear model well (R^2=0.9959), and indicates that the technique provides a good estimation of iron-oxide mass (slope is 0.94). The small non-zero y-intercept may be explained by noise, error during injection, or temperature changes during the scan.

4.6 Discussion

In this article, a voxel-based Calculation Of Susceptibility through Multiple Orientation Sampling (COSMOS) was presented. Theoretical analysis and experimental validation showed that the ill-posedness of the inverse problem of calculating a susceptibility map from the measured field map was overcome using multiple orientation oversampling. COSMOS works in the presence of noise, suppresses the common streaking artifact at , generates positive contrast for magnetic contrast agents such as gadolinium and Feridex, and provides a robust method to quantify magnetic biomarkers in biological tissues.

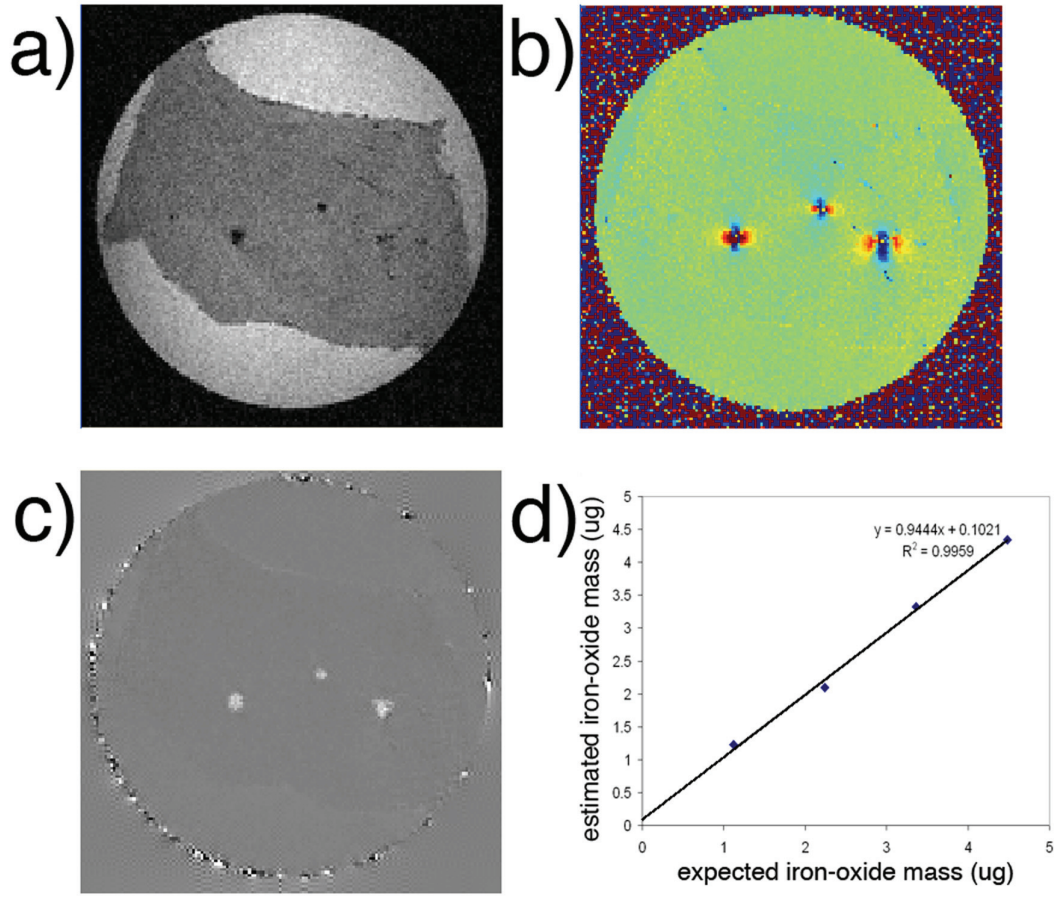

Figure 4.6. In vitro iron quantification.

(a) Magnitude of the gradient echo image of the animal tissue. (b) The corresponding δ_B field (c) Reconstructed susceptibility map from three orientations. Bright dots in the center of the slice from left to right are 2μL, 4μL and 3μL Feridex injections, respectively. (d) Estimated iron-oxide mass versus expected iron-oxide mass.

Preliminary bone imaging here suggests that COSMOS provides a novel susceptibility tissue contrast mechanism for investigating bone in MRI. Using a single susceptibility value to characterize bone tissue has been reported for bone assessment (4,7,8). Here, COSMOS enables quantitative high-resolution 3D susceptibility mapping. Our susceptibility map indicates not only the average bone susceptibility in agreement with literature but also some variation of susceptibility within the bone volume.

The ability to quantify iron content is directly beneficial for cell tracking (25-27). Magnetic nanoparticles have been increasingly used to aid the detection and characterization of cell therapy. Hypointensity caused by strong T2* effects associated with the local fields of nanoparticles are typically used to visualize magnetic nanoparticles. This hypointensity contrast is inherently difficult to quantify and could be misinterpreted as artifact. Various approaches (28-33) have been proposed to generate positive contrast by sampling off-resonance frequency information using advanced pulse sequences. Because off-resonance frequency depends on nanoparticle distribution geometry and the density of free water in the surrounding, these positive contrasts may not be quantitative. To the best of our knowledge, the COSMOS approach described here enables for the first time direct and accurate quantification of arbitrary iron distributions in tissue.

While oversampling from different orientations can avoid inverting zeroes at the dipole kernel, it cannot create new signal in signal void regions, including regions occupied by materials of high susceptibility such as Feridex and regions of little or no spins such as bone or air. It may be necessary to position observable spins next to the susceptibility source in an experimental setting for susceptibility determination. It

should be noted that resolving susceptibility distribution in regions of no observable spins may not be possible in principle. For instance, two distinct uniform concentric spheres for which the product of susceptibility with volume is constant generate almost indistinguishable outside fields. Similarly, infinitely long uniform concentric cylinders that have the same product of cross section area with susceptibility, will have identical outside fields as well (9). However, the integral of susceptibility over its distributed volume or the total magnetization can be determined from MR signal phases of spins positioned outside these susceptibility sources using the COSMOS approach.

We are very encouraged by the preliminary results of the multiple orientation sampling approach. Further development of COSMOS may be required to make it readily applicable in complex in vivo situations. Chemical shifts, primarily from fat, cause field shifts that may mix with the susceptibility effect. Susceptibility differences create a long range dipole field while chemical shifts create only local shifts, which could allow separation between susceptibility and chemical shift. Water-fat separation methods (34-37) may be adopted for the COSMOS approach.

In addition to noise, there are other sources of errors in our experiments. When performing registration, translation precision was limited to voxel and rotation was also limited to . A direct result of imperfect registration is signal dispersion, leading to underestimation in the final reconstructed susceptibility image. Also, large field inhomogeneity induced by susceptibility and chemical shift distorts voxels along the readout direction. This voxel distortion may be compensated using off resonance phase correction in the image reconstruction to provide more precise quantification of

susceptibility.

The consistent but slight underestimation of the slope between estimated and expected value in our experiments may be explained by two other factors. One factor is from the RF heating during data acquisition. During the scan, the target object absorbs energy from the radio frequency pulse causing an increase in temperature. According to Curie's law (22), susceptibility is inversely proportional to temperature, thus susceptibility will decrease during the scan. A second cause of underestimation may stem from choosing the stopping criteria in the minimization algorithm. Early termination is an implicit regularization (17), which is similar to Tikhonov regularization and tends to minimize the l_2 norm of the reconstruction.

Regularization is a general method to stabilize an ill-conditioned inversion problem. A commonly used regularization technique is Tikhonov regularization, in which the norm of the solution is minimized along with the residual. However, for susceptibility calculation, the true susceptibility distribution may not have a low l_2 norm, for instance in the Gadolinium experiment where there is a substantial Gadolinium distribution. Consequentially, Tikhonov regularization may result in qualitatively acceptable but quantitatively underestimated results. In general, the final reconstructed susceptibility map is dependent on the regularization parameter (38). The complexities and subtleties of various regularization techniques (38,39) make their comparisons with COSMOS beyond the scope of this paper, and the choice of the regularization parameter that generates accurate quantitative results is a known open question.

In the field of medical imaging, using rotation to stabilize ill-posed problems has been

well-known for a number of years. Computerized Tomography (CT) uses rotation to reconstruct a 3D volume from a series of 2D projection images. The COSMOS approach presented here for quantitative susceptibility mapping in MRI needs only three rotations, which differs from the many projections needed for angular resolution in CT. For the purpose of susceptibility quantification, Sepulveda (40) reported SQUID based susceptibility tomography in 1994. Nevertheless, the technique was not MR based and could not quantify susceptibility by just changing the angle between the object and the field. It was brought to our attention after our presentation of this work at ISMRM 2008 that the idea of sampling at two or more orientations was mentioned in the discussion of (16).

In this article, all the simulation and experiments used 0°, 60°, 120° sampling orientations because this combination yields the best noise suppression. While orientations for a human in a standard tunnel magnet are limited, such large angles are not required for susceptibility mapping. Smaller angles are feasible at the expense of a larger condition number, as could be seen from Figure 4.2, resulting in larger noise propagation and lower SNR in the final reconstruction. COSMOS could potentially be applied to human brain scan or extremity scans. Nevertheless, COSMOS would be applicable for human imaging in open magnets and for small animal imaging in most magnets.

4.7 Conclusion

COSMOS has been developed to stabilize the inverse problem from measured magnetic fields to corresponding magnetic susceptibility sources by sampling from

multiple orientations. It allows quantitative mapping of arbitrary susceptibility distributions. Susceptibility images can be reconstructed from COSMOS data by accounting for noise effects using a weighted least squares method. Simulations and MRI experiments in phantoms and in vitro confirmed that this COSMOS approach is robust and accurate for quantitative susceptibility imaging.

4.8 Appendix

4.8.1 Sampling from 2 different directions is insufficient to eliminate all the zeroes in the Fourier domain kernel

The object is placed in the magnetic field B_0 for the first scan, and the direction of the magnetic field B_0 is denoted by a unit vector $\boldsymbol{k}_{zp1}$ in the object's frame. Afterwards, the object is reoriented with respect to the magnetic field B_0 for the second scan. Consequently, the direction of B_0 is also altered in the object's frame and is represented by another unit vector $\boldsymbol{k}_{zp2}$. $\boldsymbol{k}_{zp2}$ is not parallel to $\boldsymbol{k}_{zp1}$. From these two vectors, an orthonormal basis ($\boldsymbol{e}_{k_x}$, $\boldsymbol{e}_{k_y}$, $\boldsymbol{e}_{k_z}$) is designed in the object's frame in the following manner to facilitate the calculation of the Fourier domain kernel. $\boldsymbol{e}_{k_z}$ coincides with $\boldsymbol{k}_{zp1}$. $\boldsymbol{e}_{k_x}$ is perpendicular to the plain spanned by $\boldsymbol{k}_{zp1}$ and $\boldsymbol{k}_{zp2}$, such that in the object's frame, the external magnetic field is rotated about k_x-axis. $\boldsymbol{e}_{k_y}$ is uniquely determined so that $\boldsymbol{e}_{k_y}$ is perpendicular to both $\boldsymbol{e}_{k_x}$ and $\boldsymbol{e}_{k_z}$ and this orthonormal basis follows right-hand rule.

Recall from Eq. 4.5, the Fourier domain kernel is

$$\begin{cases} 1/3-k_{zp1}^2/k^2 \\ 1/3-k_{zp2}^2/k^2 \end{cases} \Rightarrow \begin{cases} 1/3-k_z^2/k^2 \\ 1/3-(\cos\alpha\cdot k_z+\sin\alpha\cdot k_y)^2/k^2 \end{cases}$$, where α is the angle between $\boldsymbol{k}_{zp1}$and

$\boldsymbol{k}_{zp2}$. To find the zeroes, this equation needs to be solved, and the result is

$$\begin{aligned} k_x^2 &= t^2\left(\frac{3\cos^2\alpha \pm 4\cos\alpha + 1}{\sin^2\alpha}\right) \\ k_y^2 &= t^2 \\ k_z^2 &= t^2\left(\frac{\cos\alpha \pm 1}{\sin\alpha}\right)^2 \end{aligned} \quad , t \in \mathbf{R}, \text{ or}$$

$$k_x = \begin{cases} \pm\left|\frac{t}{\sin\alpha}\right| \sqrt{3\cos^2\alpha - 4\cos\alpha + 1}\ , \cos\alpha \in (-1, -1/3) \\ \pm\left|\frac{t}{\sin\alpha}\right| \sqrt{3\cos^2\alpha \pm 4\cos\alpha + 1}\ , \cos\alpha \in [-1/3, 1/3) \\ \pm\left|\frac{t}{\sin\alpha}\right| \sqrt{3\cos^2\alpha + 4\cos\alpha + 1}\ , \cos\alpha \in (1/3, 1) \end{cases} , t \in \mathbf{R}.$$

$$\begin{aligned} k_y &= \pm|t| \\ k_z &= \pm\left|t\left(\frac{\cos\alpha \pm 1}{\sin\alpha}\right)\right| \end{aligned}$$

The solution always exists and the zeroes will appear on a collection of lines.

4.8.2 Sampling from 3 different directions will eliminate all the zeroes in the Fourier domain kernel except the origin.

Given the previous two sampling directions $\boldsymbol{k}_{zp1}$ and $\boldsymbol{k}_{zp2}$, let the third sampling direction $\boldsymbol{k}_{zp3}$ be the same as $\boldsymbol{e}_{k_y}$. If $\boldsymbol{k}_{zp2}$ also happens to be parallel to $\boldsymbol{e}_{k_y}$, then let $\boldsymbol{k}_{zp2}$ be on k_y-k_z plain and is α degree apart from $\boldsymbol{k}_{zp1}$ and swap $\boldsymbol{k}_{zp2}$ and $\boldsymbol{k}_{zp3}$. To find the zeroes in the kernel, recall from Eq. 4.5, the following equation needs to be solved:

$$\begin{cases} \frac{1}{3} - \frac{k_{zp1}^2}{k^2} = 0 \\ \frac{1}{3} - \frac{k_{zp2}^2}{k^2} = 0 \\ \frac{1}{3} - \frac{k_{zp3}^2}{k^2} = 0 \end{cases} \Rightarrow \begin{cases} \frac{1}{3} - \frac{k_z^2}{k^2} = 0 \\ \frac{1}{3} - \frac{(\cos\alpha \cdot k_z + \sin\alpha \cdot k_y)^2}{k^2} = 0. \\ \frac{1}{3} - \frac{k_y^2}{k^2} = 0 \end{cases}$$

The result is $\begin{cases} k_x^2=k_y^2=k_z^2 \\ \sin 2\alpha \cdot k_z^2=0 \\ k_x^2+k_y^2+k_z^2\neq 0 \end{cases}$. However, since $\alpha \neq n\pi/2, n\in \mathbf{Z}$, this system of equations does not have a valid solution, i.e., the zero-cone surfaces of the three Fourier domain kernels do not intercept simultaneously.

4.9 Reference

1. Arepally A. Targeted drug delivery under MRI guidance. J Magn Reson Imaging 2008;27(2):292-298.

2. Kraitchman DL, Gilson WD, Lorenz CH. Stem cell therapy: MRI guidance and monitoring. J Magn Reson Imaging 2008;27(2):299-310.

3. Chu Z, Cohen AR, Muthupillai R, Chung T, Wang ZJ. MRI measurement of hepatic magnetic susceptibility-phantom validation and normal subject studies. Magn Reson Med 2004;52(6):1318-1327.

4. Chung HW, Hwang SN, Yeung HN, Wehrli FW. Mapping of the magnetic-field distribution in cancellous bone. Journal of magnetic resonance 1996;113(2):172-176.

5. Fernandez-Seara MA, Techawiboonwong A, Detre JA, Wehrli FW. MR susceptometry for measuring global brain oxygen extraction. Magn Reson Med 2006;55(5):967-973.

6. Haacke EM, Cheng NY, House MJ, Liu Q, Neelavalli J, Ogg RJ, Khan A, Ayaz M, Kirsch W, Obenaus A. Imaging iron stores in the brain using magnetic resonance imaging. Magn Reson Imaging 2005;23(1):1-25.

7. Hopkins JA, Wehrli FW. Magnetic susceptibility measurement of insoluble solids by NMR: magnetic susceptibility of bone. Magn Reson Med 1997;37(4):494-500.

8. Schick F, Seitz D, Machann J, Lutz O, Claussen CD. Magnetic resonance bone densitometry. Comparison of different methods based on susceptibility. Investigative radiology 1995;30(4):254-265.

9. Haacke EM, Brown RW, Thompson MR, Venkatesan R. Objects in External Fields: the Lorentz Sphere. Magnetic Resonance Imaging: Physical Principles and Sequence Design New York: Wiley-Liss; 1999. p 749-757.

10. Beuf O, Briguet A, Lissac M, Davis R. Magnetic resonance imaging for the determination of magnetic susceptibility of materials. Journal of magnetic resonance 1996;112(2):111-118.

11. Cheng YC, Hsieh CY, Neelavalli J, Liu Q, Dawood MS, Haacke EM. A complex sum method of quantifying susceptibilities in cylindrical objects: the first step toward quantitative diagnosis of small objects in MRI. Magn Reson Imaging 2007;25(8):1171-1180.

12. Wang ZJ, Li S, Haselgrove JC. Magnetic resonance imaging measurement of volume magnetic susceptibility using a boundary condition. J Magn Reson 1999;140(2):477-481.

13. Li L, Leigh JS. Quantifying arbitrary magnetic susceptibility distributions with MR. Magn Reson Med 2004;51(5):1077-1082.

14. Morgan J, Irarrazaval P. Efficient solving for arbitrary susceptibility distributions using residual difference fields. 2007; Berlin, Germany. p 35.

15. Salomir R, Senneville BDd, Moonen CT. A Fast Calculation Method for

Magnetic Field Inhomogeneity due to an Arbitrary Distribution of Bulk Susceptibility. Concepts Magn Reson B 2003;19B:26-34.

16. Marques JP, Bowtell R. Application of a Fourier-Based Method for Rapid Calculation of Field Inhomogeneity Due to Spatial Variation of Magnetic Susceptibility. Concepts in Magnetic Resonance Part B 2005;25B(1):65-78.

17. Hanke M, Hansen PC. Regularization methods for large-scale problems. Surveys on Mathematics for Industry 1993;3:253-315.

18. Demmel JW. Perturbation Theory for the Least Squares Problem. Applied Numerical Linear Algebra. Berkeley, California: SIAM; 1997. p 117-118.

19. Moon TK, Stirling WC. Theory of the SVD. Mathematical Methods and Algorithms for Signal Processing. Upper Saddle River, New Jersey: Prentice Hall; 1999. p 369-370.

20. Conturo TE, Smith GD. Signal-to-noise in phase angle reconstruction: dynamic range extension using phase reference offsets. Magn Reson Med 1990;15(3):420-437.

21. Shepp LA, Logan BF. The Fourier Reconstruction of a Head Section. IEEE Trans on Nuclear Science 1974(21):21-43.

22. O'Handley RC. Quantum Paramagnetism and Diamagnetism. Modern Magnetic Materials Principles and Applications. New York: John Wiley & Sons; 2000. p 92, 492,.

23. Paige CC, Saunders MA. LSQR: An algorithm for sparse linear equations and sparse least squares. ACM Transactions on Mathematical Software 1982;8(1):43-71.

24. Jung CW, Jacobs P. Physical and chemical properties of superparamagnetic iron oxide MR contrast agents: ferumoxides, ferumoxtran, ferumoxsil. Magn Reson Imaging 1995;13(5):661-674.

25. Arbab AS, Bashaw LA, Miller BR, Jordan EK, Bulte JW, Frank JA. Intracytoplasmic tagging of cells with ferumoxides and transfection agent for cellular magnetic resonance imaging after cell transplantation: methods and techniques. Transplantation 2003;76(7):1123-1130.

26. Arbab AS, Yocum GT, Kalish H, Jordan EK, Anderson SA, Khakoo AY, Read EJ, Frank JA. Efficient magnetic cell labeling with protamine sulfate complexed to ferumoxides for cellular MRI. Blood 2004;104(4):1217-1223.

27. Rad AM, Arbab AS, Iskander AS, Jiang Q, Soltanian-Zadeh H. Quantification of superparamagnetic iron oxide (SPIO)-labeled cells using MRI. J Magn Reson Imaging 2007;26(2):366-374.

28. Cunningham CH, Arai T, Yang PC, McConnell MV, Pauly JM, Conolly SM. Positive contrast magnetic resonance imaging of cells labeled with magnetic nanoparticles. Magn Reson Med 2005;53(5):999-1005.

29. Edelman RR, Storey P, Dunkle E, Li W, Carrillo A, Vu A, Carroll TJ. Gadolinium-enhanced off-resonance contrast angiography. Magn Reson Med 2007;57(3):475-484.

30. Faber C, Heil C, Zahneisen B, Balla DZ, Bowtell R. Sensitivity to local dipole fields in the CRAZED experiment: an approach to bright spot MRI. J Magn Reson 2006;182(2):315-324.

31. Koktzoglou I, Li D, Dharmakumar R. Dephased FLAPS for improved visualization of susceptibility-shifted passive devices for real-time interventional MRI. Physics in medicine and biology 2007;52(13):N277-286.

32. Mani V, Briley-Saebo KC, Itskovich VV, Samber DD, Fayad ZA. Gradient echo acquisition for superparamagnetic particles with positive contrast (GRASP): sequence characterization in membrane and glass superparamagnetic iron oxide phantoms at 1.5T and 3T. Magn Reson Med 2006;55(1):126-135.

33. Stuber M, Gilson WD, Schar M, Kedziorek DA, Hofmann LV, Shah S, Vonken EJ, Bulte JW, Kraitchman DL. Positive contrast visualization of iron oxide-labeled stem cells using inversion-recovery with ON-resonant water suppression (IRON). Magn Reson Med 2007;58(5):1072-1077.

34. Glover GH, Schneider E. Three-point Dixon technique for true water/fat decomposition with B0 inhomogeneity correction. Magn Reson Med 1991;18(2):371-383.

35. Hernando D, Haldar JP, Sutton BP, Ma J, Kellman P, Liang ZP. Joint estimation of water/fat images and field inhomogeneity map. Magn Reson Med 2008;59(3):571-580.

36. Reeder SB, McKenzie CA, Pineda AR, Yu H, Shimakawa A, Brau AC,

Hargreaves BA, Gold GE, Brittain JH. Water-fat separation with IDEAL gradient-echo imaging. J Magn Reson Imaging 2007;25(3):644-652.

37. Reeder SB, Wen Z, Yu H, Pineda AR, Gold GE, Markl M, Pelc NJ. Multicoil Dixon chemical species separation with an iterative least-squares estimation method. Magn Reson Med 2004;51(1):35-45.

38. Kressler B, de Rochefort L, Spincemaille P, Liu T, Wang Y. Estimation of Sparse Magnetic Susceptibility Distributions from MRI using Non-linear Regularization. 2008 April; Toronto. p 1514.

39. Shmueli K, van Gelderen P, Li T, Duyn J. High Resolution Human Brain Susceptibility Maps Calculated from 7 Tesla MRI Phase Data. 2008 April; Toronto. p 642.

40. Sepulveda NG, Thomas IM, John P. Wikswo J. Magnetic Susceptibility Tomography for Three-Dimensional Imaging of Diamagnetic and Paramagnetic Objects. IEEE TRANSACTIONS ON MAGNETICS 1994;30(6):5062-5069.

CHAPTER 5

5 MORPHOLOGY ENABLED DIPOLE INVERSION

5.1 Abstract

Magnetic susceptibility varies among brain structures and provides insights into the chemical and molecular composition of brain tissues. However, the determination of an arbitrary susceptibility distribution from the measured MR signal phase is a challenging, ill-conditioned inverse problem. Although a previous method named COSMOS has solved this inverse problem both theoretically and experimentally using multiple angle acquisitions, it is often impractical to carry out on human subjects. Recently the feasibility of calculating the brain susceptibility distribution from a single-angle acquisition was demonstrated using morphology enabled dipole inversion (MEDI). In this study, we further improved the original MEDI method by sparsifying the edges in the QSM that do not have a corresponding edge in the magnitude image. Quantitative susceptibility maps generated by the improved MEDI were compared qualitatively and quantitatively with those generated by COSMOS. The results show a high degree of agreement between MEDI and COSMOS, and the practicality of MEDI allows many potential clinical applications.

5.2 Introduction

Magnetic susceptibility is a physical property of a material that may help to detect and quantify specific biomarkers such as iron, calcium and gadolinium for assessing brain physiology and pathology. The susceptibility of non-ferromagnetic biomaterial along the main magnetic field generates a local field that is equal to the convolution of the

volume susceptibility distribution with a unit dipole field (1-3). Because the dipole field has values equal or close to zero at the magic angle in the Fourier domain, the field to susceptibility source inverse problem is ill-conditioned, resulting in severe noise amplification (4).

A unique and accurate "Calculation Of Susceptibility" is achievable through "Multiple Orientation Sampling" (COSMOS) (5-6). This model-free calculation method keeps full fidelity to the measured data but requires multiple acquisitions and reorienting the anatomy of interest with respect to the main magnetic field. The impracticality of re-positioning human subjects in a standard magnet limits the use of COSMOS. Alternatively, a unique solution may be selected among many possibilities using truncated k-space division (7), or regularization that encodes a priori information. Different regularization strategies have been attempted including and assumptions of a localized (8), smooth (4), sparse (4) or piece-wise constant solution (9). All these single orientation calculation techniques are more practical from a data acquisition point of view for human brain imaging, but their solutions are subject to systematic biases when the assumed mathematical properties do not agree with the physical reality. In-vivo validation of these techniques is crucial for establishing a technical standard and has yet to be performed.

In this study, we aim to demonstrate the feasibility of generating a quantitative susceptibility map (QSM) from a single angle acquisition with comparable quality to the one generated by COSMOS in human brain imaging by incorporating the morphological information that is already available in the magnitude images. Our previous study showed that this Morphology Enabled Dipole Inversion (MEDI)

method successfully suppressed the streaking artifacts that often appear in quantitative susceptibility maps (QSM) (10). This technique was further improved for better quantitative accuracy as well as image quality by sparsifying the edges in the QSM that do not correspond to an edge in the magnitude image (11). The first in-vivo validation of this technique was performed by comparing it with COSMOS in healthy volunteers.

5.3 Theory

5.3.1 Morphology Enabled Dipole Inversion (MEDI)

The MEDI method makes use of the observation that the locations of the interfaces (or edges) in the susceptibility distribution are nearly the same as those in magnitude images obtained in the same acquisition, and we consider their discordance to be sparse. To promote this sparsity, we employ a weighted l1 minimization that penalizes a susceptibility at those voxels that are not part of an interface in the magnitude image. The minimization is constrained by data fidelity ensuring that the local field induced by the estimated susceptibility distribution agrees with the local field as measured from the phase image (11):

$$\min_{\chi} \|M\nabla\chi\|_1$$

$$\text{s.t. } \|W(\delta_B - F_D\chi)\|_2 = \varepsilon \qquad [5.1]$$

Here ∇ is a 3D gradient operator on the vectorized susceptibility distribution χ; M is a binary gradient weighting diagonal matrix, where the diagonal elements are equal to 0 when they correspond to non-negligible gradients in the magnitude image (defined as

5 times greater than the background noise standard deviation in the magnitude image) and are equal to 1 otherwise; F_D is a matrix encoding the convolution with the unit dipole field : $F_D=F^{-1}DF$, where D is the dipole kernel expressed in the Fourier domain. When the Lorentz sphere correction is taken into account, D can be written as $D(\boldsymbol{k}) = 1/3 - k_z^2/k^2$ with $D(\mathbf{0}) = 0$, where k is the magnitude of a Fourier domain coordinate vector $\boldsymbol{k}$, and k_z its projection onto the direction of the main field. The calculation of F_D is facilitated by the 3D Fast Fourier transform F (4); δ_B is the measured local field map and W is a data weighting matrix to account for the non-uniform phase noise. The data weighting W and the expected noise level ε are derived from the magnitude images across all the echoes by calculating the error propagation from the phase noise to the field noise during a weighted least-squares fitting as described in the methods section (see below) (4,10).

The solution of the constrained convex optimization problem Eq. 5.1 coincides with the unconstrained Lagrangian problem with a properly chosen parameter λ:

$$\chi^* = \text{argmin}_\chi ||M\nabla\chi||_1 + \lambda||W(\delta_B - F_D\chi)||_2^2, \qquad [5.2]$$

where χ^* is the solution of susceptibility distribution to the minimization problem. The value of λ is chosen such that $||W(\delta_B - F_D\chi)||_2 \approx \varepsilon$ (12). Eq. 5.2 was solved using a lagged diffusivity fixed point method (13).

5.3.2 Calculation Of Susceptibility through Multiple Orientation Sampling (COSMOS)

The ill-conditioned inverse problem of determining an arbitrary susceptibility

distribution from the measured local magnetic field can also be addressed by multiple orientation sampling. The inverse problem is subsequently formulated as a minimization problem:

$$\chi^* = \text{argmin}_\chi = \sum_{i=1}^{N} ||W_i(\delta_{Bi} - F_{Di}\chi)||_2^2 \quad , \qquad [5.3]$$

where δ_{Bi}, W_i, and F_{Di} are the local field map, data weighting and the corresponding dipole convolution matrix, respectively for each of the various angles with i denoting the i-th of N orientations; N is greater than 2 to ensure that the inversion is overdetermined. This minimization problem is solved using a conjugate gradient algorithm (5).

5.4 Methods and Materials

5.4.1 Data acquisition

The human study was approved by our Institutional Review Board. Nine healthy volunteers were recruited (4 female, 5 male, the mean age was 26 years and its standard deviation was 4.3 years) to perform MR brain imaging on a 3.0 T scanner (HDx, GE Healthcare, Waukesha, WI, USA) with a single channel birdcage head coil. A 3D multi-echo spoiled gradient echo sequence was used, sampling multiple TEs in one TR. The polarity of the readout gradients were the same for all the TEs. Imaging parameters were as follows: TEs = 3.5, 7.0, 10.5, 14.0, 17.5, 21.0 ms; TR = 40 ms; voxel size = 1×1×3 mm3; matrix size = 240×240×60; BW = ±62.5kHz, FA = 15° and NEX = 1. The prescribed axial volume was not rotated between the different orientation. In the first acquisition, the head was in the neutral position. In order to use

COSMOS, we performed two additional scans using identical imaging parameters on each volunteer by instructing them to bring their left ear to their left shoulder for the second scan, and then bring their right ear to their right shoulder for the third scan. The raw k-space data was used for processing, and a 3D Fourier transform was applied immediately to the k-space data to reconstruct the images.

5.4.2 Field Map Estimation

The phase images were first extracted from the complex MRI data. To estimate the field map, a 1-D temporal unwrapping of the phase was performed in each voxel followed by a weighted least-squares fit of the temporally unwrapped phases in each voxel over TE (4,9). To address the frequency aliasing on the field map, a magnitude map guided spatial unwrapping algorithm was subsequently applied (14). In order to separate the local field generated by local magnetic sources from the background field, the latter was removed by applying a projection onto dipole fields procedure, where all the voxels inside the field of view but outside the brain region were assumed to be responsible for the background field inside the brain, and the strength of the dipole in each background voxel was determined through a weighted least-squares fit to the field inside the brain (10,15). The corrected field served as the input for the field to source inverse problem (Eqs. 5.2&5.3).

5.4.3 Susceptibility Analysis

For the in-vivo brain comparison, the COSMOS method was applied using all three acquired 3D volumes. The 3D dataset acquired at the neutral head position was also used for the MEDI calculation. Calculations were performed in MATLAB

(MathWorks, Natick, MA, USA) on a personal computer with an Intel® Core™ i7 processor and 6 GB of memory, and the calculation time of both methods was recorded. The co-registration required by COSMOS was accomplished using the co-registration component of the Statistical Parametric Mapping software (Wellcome Department of Cognitive Neurology, London, UK) (16). The susceptibility maps calculated by MEDI and COSMOS on these volunteers were displayed in a randomized order for image quality inspection. Considering streaking artifacts and blurring, an experienced image reader, blinded to the method used to calculate each susceptibility map, rated the image quality using the following score system: 1 = free of artifacts or blurring, excellent quality, 2 = minor artifacts or blurring, good quality, 3 = modest artifacts or blurring, diagnosable quality, 4 = severe artifacts or blurring, non-diagnostic. A paired Wilcoxon rank sum test was performed to determine significant differences in image quality between MEDI and COSMOS. For each method, the average image score and standard deviation across all the volunteers were calculated.

On the calculated susceptibility maps, we first performed a region of interest (ROI) based quantitative comparison, where susceptibility values were measured relative to that of white matter (immediately above the corpus callosum). Iron-rich structures including caudate nucleus, putamen, globus pallidus (a), substantia nigra and red nucleus (b), were identified on the magnitude images from the gradient echo acquisition. The great vein of galen was also identified from the reformatted sagittal plane of the magnitude image (d). Manually drawn contours of these brain regions were transferred to the calculated QSM images. Because of the relative lack of

contrast between gray and white matter in the magnitude images, selected gray matter and white matter regions of the cortex were identified on the COSMOS-calculated QSM images and then transferred to the MEDI image. For each subject and for each ROI, the average susceptibility was measured inside the regions on both the COSMOS and the MEDI-calculated QSMs. Linear regression and Bland-Altman analysis were performed in these pre-identified regions to assess the agreement of the average susceptibility values between these two methods. We also defined the contrast to noise ratio (CNR) of each QSM as the mean susceptibility in the globus pallidus (χ_{GP}) divided by the standard deviation of the susceptibility of white matter in the ROI above the corpus callosum($\sigma_{\chi_{WM}}$): CNR = $\frac{\chi_{GP}}{\sigma_{\chi_{WM}}}$. A paired t-test was performed to evaluate whether there was any statistically significant difference in CNR between MEDI and COSMOS. For each method, the average CNR and standard deviation across all the volunteers were calculated. Finally, for each brain region and each susceptibility calculation method, the mean and standard deviation of the susceptibilities in this group of healthy volunteers was recorded.

In addition to the ROI-based quantitative comparison, a voxel-based linear regression and a Bland Altman analysis were also performed across all brain voxels in all volunteers to assess the agreement between the two methods.

5.5 Results

Net scan time and susceptibility calculation time are reported in Table 5.1. The net scan time of COSMOS was three times that of MEDI due to the two additional scans,

not including the time taken between scans to allow the volunteers to re-position their heads. The QSM calculation time for MEDI was approximately five times that of COSMOS because MEDI requires about 600 iterations for convergence while COSMOS needs about 40 iterations.

A representative MEDI-calculated QSM is shown in . The magnitude image (a-d) provided structural information regarding the susceptibility distribution, and local field map (from which the susceptibility distribution was calculated) is shown in e-h. Iron-rich brain structures including veins and basal ganglia were clearly depicted in the QSM images (i-l). The streaking artifacts along the magic angle that are often seen in the coronal or sagittal plane (7) were successfully suppressed (k&l).

Table 5.1. Comparison of net scan time, calculation time, CNR and image score.

	Net Scan Time (min)	Calculation Time (min)	CNR	Image score
MEDI	9.6	20±10	24±13	1.78±0.44
COSMOS	28.8	4±1	26±8	1.56±0.53

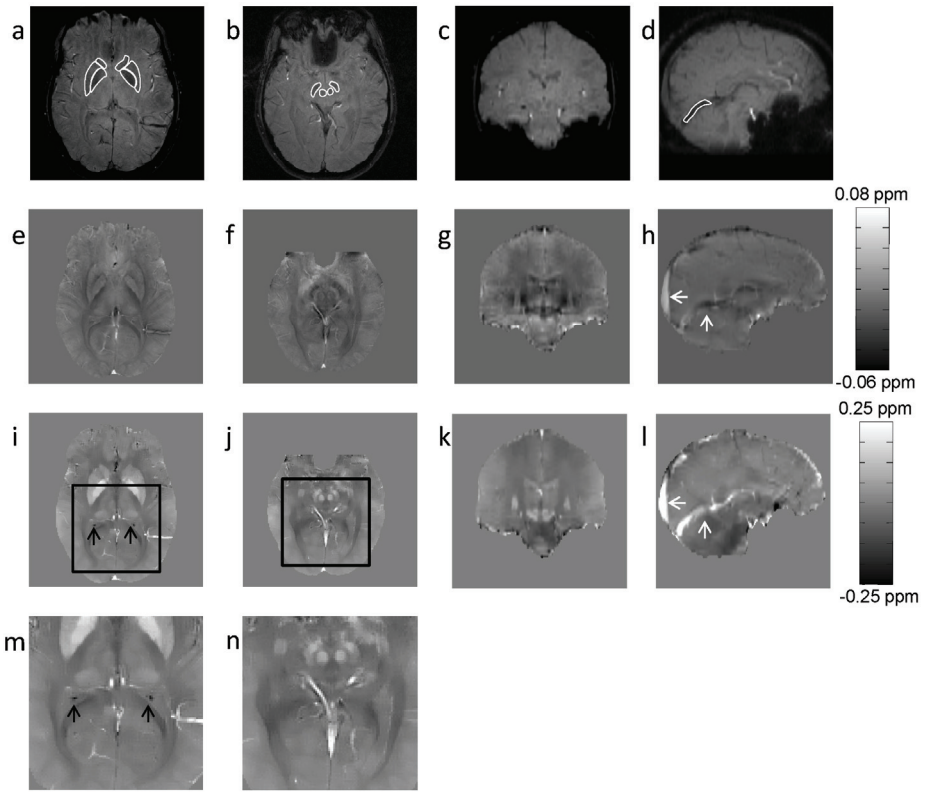

Figure 5.1. A representative case of MEDI-calculated QSM.

The axial, coronal and sagittal sections of the magnitude images of the 5th echo (TE = 17.5ms) are shown in a, b, c and d, with manually delineated brain structures.(a. Globus pallidus, putamen and caudate nucleus. b. Red nucleus and substantia nigra. d. The great vein of galen.) The superior-inferior direction is linearly interpolated to achieve an isotropic resolution for display purposes only. The corresponding field maps are exhibited in e-h. Calculated QSMs in these sections (i-l) eliminates the blooming dipole effects seen in the field maps, and the susceptibility of the veins (white arrows) does not depend on the angle of the vein with respect to the main magnetic field as shown in h. Negative susceptibility is often found as small clusters in the lateral ventricles (black arrows) as shown in m, which is a zoom-in of the black box in i. Similarly, n is a zoom-in of the black box in j.

For the qualitative in-vivo brain comparison, all volunteers achieved enough rotation in the coronal plane (approximately 20° as measured by the co-registration algorithm) to reconstruct an artifact-free QSM using the reference COSMOS method. Both methods provided similar image quality and virtually identical contrasts for most brain structures except the background cortex region where COSMOS revealed slightly more details (Figure 5.2a). Iron-rich tissues including globus pallidus, putamen, caudate nucleus, thalamus, substantia nigra, red nucleus, dentate nucleus, venous blood and cortex show positive values on both COSMOS and MEDI-calculated QSMs. Negative susceptibility values were often found as small clusters in the posterior horn of lateral ventricles (black arrows in Figure 5.1i), and are consistently distributed within the white matter in both COSMOS- and MEDI-calculated QSMs. COSMOS and MEDI were rated identically (either 1 or 2) in 7 of the 9 volunteers. In the other 2 cases, COSMOS got a more favorable score than MEDI (1 for COSMOS compared to 2 for MEDI in both cases). Average image scores are listed in Table 5.1. No statistically significant difference was found in the image quality ($p = 0.62$).

In the ROI-based quantitative comparison, the slope of the linear regression between COSMOS and MEDI was close to unity and the intercept was close to zero. The correlation coefficient was also close to one, indicating a good agreement between the MEDI and COSMOS susceptibility measurements (Figure 5.2b). The Bland-Altman plot exhibited no significant bias or trend between MEDI and COSMOS. The 95% limit of agreement between MEDI and COSMOS was -0.039 to 0.028ppm over the range of approximately 0 to 0.31ppm (Figure 5.2c). Both methods provided similar CNR without statistically significant differences ($p = 0.32$) (Table 5.1). Average

susceptibility values in different brain regions across all the volunteers are summarized in Table 5.2.

In the voxel-based quantitative comparison, the slope of the linear regression between COSMOS and MEDI showed 13% underestimation of the susceptibility by MEDI with respect to COSMOS and had an intercept close to zero. The correlation coefficient was $r = 0.86$ (Figure 5.2d). The 95% limit of agreement between MEDI and COSMOS was -0.032 to 0.033ppm over the range of approximately -0.3 to 0.5ppm (Figure 5.2e).

Table 5.2. Susceptibility in different brain regions.

Unit ppm	MEDI		COSMOS	
	Mean	Std	Mean	Std
Cortex Gray Matter	0.046	0.018	0.053	0.012
Red Nucleus	0.077	0.045	0.087	0.023
Putamen	0.082	0.022	0.086	0.041
Caudate Nucleus	0.089	0.019	0.080	0.020
Substantia Nigra	0.115	0.030	0.130	0.029
Globus Pallidus	0.187	0.018	0.187	0.017
Venous Blood	0.277	0.020	0.287	0.026

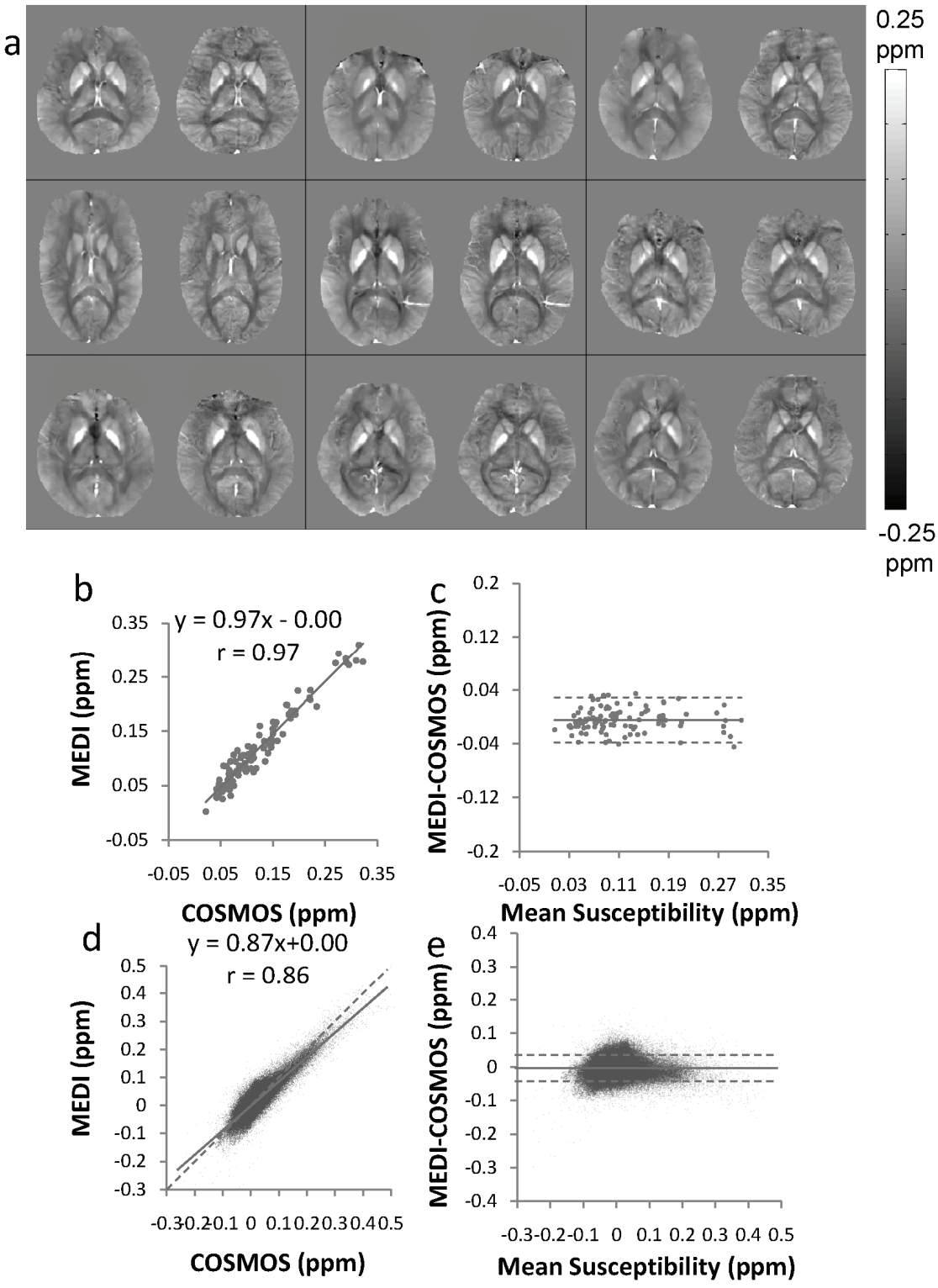
a
0.25 ppm
-0.25 ppm
b
y = 0.97x - 0.00
r = 0.97
MEDI (ppm)
COSMOS (ppm)
c
MEDI-COSMOS (ppm)
Mean Susceptibility (ppm)
d
y = 0.87x+0.00
r = 0.86
MEDI (ppm)
COSMOS (ppm)
e
MEDI-COSMOS (ppm)
Mean Susceptibility (ppm)

Figure 5.2. Qualitative and quantitative comparison between MEDI and COSMOS. A QSM slice that clearly showed globus pallidus was selected from each of the 9 volunteers, and all such slices are shown in a). For each case, the left image is the MEDI-calculated QSM and the right image is the COSMOS-calculated QSM. Both b) linear regression and c) Bland-Altman analysis demonstrate excellent agreement between MEDI and COSMOS regional susceptibility measurements. The voxel-based linear regression (d) performed shows small underestimation of the susceptibility by MEDI as compared to COSMOS, and the Bland-Altman analysis is displayed in (e). The solid lines in b&d are the trend lines of the linear regression and the dashed line in d is the line of equality. The solid and dashed lines in c&e indicate the mean difference ± 2× the standard deviation of the difference, respectively.

5.6 Discussion

The results here presented the first in vivo validation of a practical quantitative susceptibility mapping (QSM) technique. Both the quality and the quantitative susceptibility measurements of the MEDI reconstructed QSM were comparable to the reference COSMOS method. The susceptibility of venous blood was 0.28±0.02ppm, which is in the same range of literature value (0.31±0.07ppm (17)). MEDI is able to utilize additional anatomical information to compensate for the mild ill-conditioning caused by the zeros at the magic angle. Without the cumbersome brain reorientation required by COSMOS, MEDI provided a practical solution to study brain susceptibility that is likely to have various clinical applications.

The image quality of MEDI and COSMOS was similar, as observed in Figure 5.2a and as indicated by the image scores in Table 5.1. The major difficulty in obtaining a high

quality QSM arises from the zeros in the dipole kernel. These may lead to streaking artifacts in the QSM images (7). Accordingly, we defined the noise in the CNR measurement as the standard deviation of susceptibility over a uniform anatomical region to reflect the severity of streaking artifacts. Therefore, the virtually identical contrasts and the similar CNRs in Table 5.1 suggest that both methods achieved a similar noise level, or comparable streaking artifact suppression.

Nevertheless, it should be noted COSMOS and MEDI achieved streaking artifact suppression through distinct mechanisms. COSMOS eliminated the streaking artifacts by oversampling and keeps full fidelity to the sampled data, but the l_1 solver in the MEDI suppressed the streaking artifacts by penalizing small variations that were not reflected in magnitude images (13). The difference between these two mechanisms is best demonstrated in a cortical region shown in Figure 5.3, where MEDI-calculated QSM appears to be smoother. Although MEDI successfully removed the streaking artifact, it also reduced the susceptibility contrast in the cortex where the interface information from the gradient echo magnitude image was ambiguous and the gray-white matter phase contrast at 3T was not as prominent as that of other iron-rich brain structures. Without regularization, COSMOS was able to preserve such details. On the other hand, we also observed that when the susceptibility contrast is stronger than the size of the confidence interval of the Bland-Altman analysis (0.065ppm), such as the ROIs shown in Figure 5.1 and the comparison in Figure 5.2a, MEDI does not tend to underestimate the susceptibility in such regions as caudate nucleus even though the edge information is vague on the anatomical image. This preferential underestimation may also explain the discrepancy between the ROI-based and the voxel-based linear

regression as shown in Figure 5.2. In the voxel-based linear regression, most of the brain voxels are in the parenchyma region, which are expected to be underestimated in MEDI due to the weak susceptibility contrast. If voxels whose value is smaller than 0.065ppm are excluded from the linear regression, the slope is 0.95 and the correlation coefficient is 0.92.

For subtle brain lesions whose susceptibility and magnitude contrasts are both low, the susceptibility estimation of MEDI may not be as accurate as that of COSMOS. Indeed, due to the over-sampling in COSMOS, the accuracy of the COSMOS should always be superior to that of MEDI. However, all our subjects indicated that it was uncomfortable to hold their heads in rotated non-neutral positions. The long scan time required by COSMOS makes it difficult to perform in clinical practice. So far we have not been able to get any patient in our medical center agreed to perform multiple-angle acquisition, though we have obtained many MEDI cases (n>50) from our brain stroke protocol and of Parkinson's Disease. The single-orientation acquisition of the MEDI method can always be used to reconstruct a QSM for preview in numerous potential clinical applications when data are incomplete for COSMOS. In patients with microbleeds, hemorrhages or venous malformations, the susceptibility arising from hemosiderin or deoxygenated hemoglobin is potentially strong enough to be accurately quantified by the MEDI method and to be used as an auxiliary tool for disease stratification. Similarly, the MEDI method may be used to evaluate the excessive iron deposition in various brain structures in patients with Parkinson's disease, Alzheimer's disease or Huntington's chorea (18).

The small clusters with negative susceptibility values often found in the posterior horn

of lateral ventricles may arise from calcium accumulation. The negative susceptibility of calcification has been confirmed experimentally for cortical bone samples (5,9), and the calcification in this location is usually a benign finding. Several white matter tracts also exhibited negative susceptibility values, most noticeably the corpus callosum, corticospinal tract, and optic radiation. This negative value may reveal directional information regarding white matter fibers (19-20). To further improve the calculation performance in the white matter area, a generalized Lorentzian correction may be required to account for the field induced by the fiber bundles (21).

5.7 Conclusion

In this study, we have demonstrated that the Morphology Enabled Dipole Inversion (MEDI) method is able to generate a high quality quantitative susceptibility map by solving the inverse problem from magnetic field to susceptibility source. The human brain imaging results showed high degree of agreement with a reference method (COSMOS). The MEDI method provides a practical solution to QSM, and is readily applicable to clinical investigations.

Figure 5.3. A zoom-in on the cortical regions.

a) and b) are QSMs calculated by COSMOS and MEDI. On the COSMOS-calculated QSM, the white matter area above the corpus callosum and a region in the cortex gray matter are manually identified as described in the method section, and is shown in c, which is a spatial zoom of the black box in a. Similarly, d is the spatial zoom of the black box in b. e) MEDI- and COSMOS-calculated susceptibility variations along the line drawn on d is shown in e. MEDI method preserves the high contrasts relatively well with some underestimation of the low contrasts.

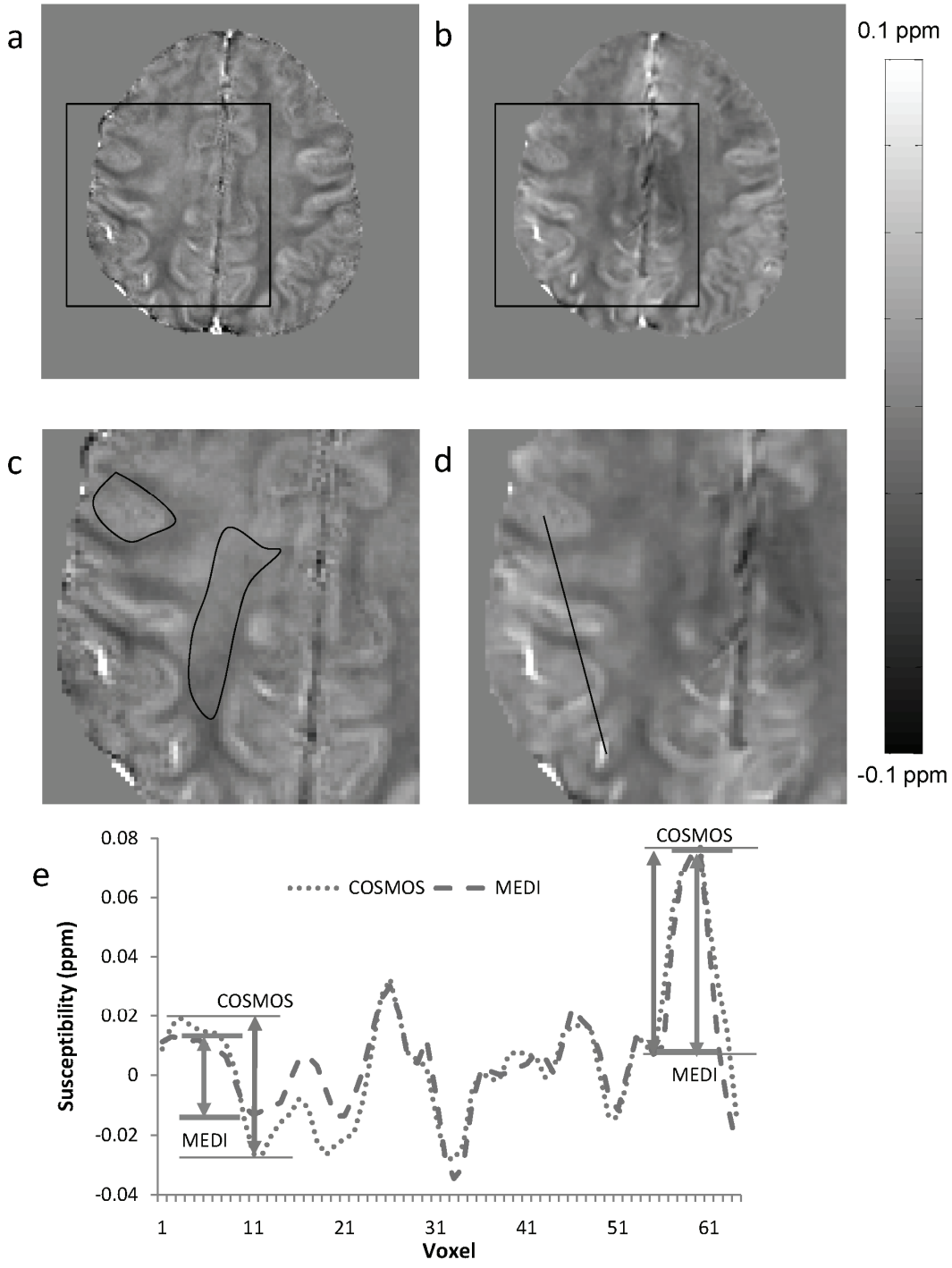
a
b
0.1 ppm
-0.1 ppm
c
d
e
COSMOS
MEDI
Susceptibility (ppm)
0.08
0.06
0.04
0.02
0
-0.02
-0.04
1
11
21
31
41
51
61
Voxel

5.8 Reference

1. Koch KM, Papademetris X, Rothman DL, de Graaf RA. Rapid calculations of susceptibility-induced magnetostatic field perturbations for in vivo magnetic resonance. Phys Med Biol 2006;51(24):6381-6402.

2. Marques JP, Bowtell R. Application of a Fourier-based method for rapid calculation of field inhomogeneity due to spatial variation of magnetic susceptibility. Concepts in Magnetic Resonance Part B: Magnetic Resonance Engineering 2005;25B(1):65-78.

3. Salomir R, De Senneville BD, Moonen CTW. A fast calculation method for magnetic field inhomogeneity due to an arbitrary distribution of bulk susceptibility. Concepts in Magnetic Resonance Part B-Magnetic Resonance Engineering 2003;19B(1):26-34.

4. Kressler B, de Rochefort L, Liu T, Spincemaille P, Jiang Q, Wang Y. Nonlinear regularization for per voxel estimation of magnetic susceptibility distributions from MRI field maps. IEEE Trans Med Imaging 2010;29(2):273-281.

5. Liu T, Spincemaille P, de Rochefort L, Kressler B, Wang Y. Calculation of susceptibility through multiple orientation sampling (COSMOS): a method for conditioning the inverse problem from measured magnetic field map to susceptibility source image in MRI. Magn Reson Med 2009;61(1):196-204.

6. Wharton S, Schafer A, Bowtell R. Susceptibility mapping in the human brain using threshold-based k-space division. Magn Reson Med 2010;63(5):1292-1304.

7. Shmueli K, de Zwart JA, van Gelderen P, Li TQ, Dodd SJ, Duyn JH. Magnetic susceptibility mapping of brain tissue in vivo using MRI phase data. Magn Reson Med 2009;62(6):1510-1522.

8. Li L, Leigh JS. Quantifying arbitrary magnetic susceptibility distributions with MR. Magn Reson Med 2004;51(5):1077-1082.

9. de Rochefort L, Brown R, Prince MR, Wang Y. Quantitative MR susceptibility mapping using piece-wise constant regularized inversion of the magnetic field. Magn Reson Med 2008;60(4):1003-1009.

10. de Rochefort L, Liu T, Kressler B, Liu J, Spincemaille P, Lebon V, Wu J, Wang Y. Quantitative susceptibility map reconstruction from MR phase data using bayesian regularization: validation and application to brain imaging. Magn Reson Med 2010;63(1):194-206.

11. Liu J, Liu T, de Rochefort L, Khalidov I, Prince MR, Wang Y. Quantitative Susceptibility Mapping by Regulating the Field to Source Inverse Problem with a Sparse Prior Derived from the Maxwell Equation: Validation and Application to Brain 2010. Proceedings of the 18th Annual Meeting of ISMRM. p 4996.

12. Lustig M, Donoho D, Pauly JM. Sparse MRI: The application of compressed sensing for rapid MR imaging. Magn Reson Med 2007;58(6):1182-1195.

13. Vogel CR, Oman ME. Iterative methods for total variation denoising. Siam Journal on Scientific Computing 1996;17(1):227-238.

14. Cusack R, Papadakis N. New robust 3-D phase unwrapping algorithms:

application to magnetic field mapping and undistorting echoplanar images. Neuroimage 2002;16(3 Pt 1):754-764.

15. Liu T, Khalidov I, de Rochefort L, Spincemaille P, Liu J, Wang Y. Improved background field correction using effective dipole fitting. 2010. Proceedings of the 18th Annual Meeting of ISMRM. p 141.

16. Ashburner J, Friston K. Multimodal image coregistration and partitioning--a unified framework. Neuroimage 1997;6(3):209-217.

17. Fernandez-Seara MA, Techawiboonwong A, Detre JA, Wehrli FW. MR susceptometry for measuring global brain oxygen extraction. Magn Reson Med 2006;55(5):967-973.

18. Zecca L, Youdim MB, Riederer P, Connor JR, Crichton RR. Iron, brain ageing and neurodegenerative disorders. Nat Rev Neurosci 2004;5(11):863-873.

19. Lee J, Shmueli K, Fukunaga M, van Gelderen P, Merkle H, Silva AC, Duyn JH. Sensitivity of MRI resonance frequency to the orientation of brain tissue microstructure. Proc Natl Acad Sci U S A 2010;107(11):5130-5135.

20. Liu C. Susceptibility tensor imaging. Magn Reson Med 2010;63(6):1471-1477.

21. He X, Yablonskiy DA. Biophysical mechanisms of phase contrast in gradient echo MRI. Proc Natl Acad Sci U S A 2009;106(32):13558-13563.

CHAPTER 6

6 DIFFERENTIATION OF SPIO AND AIR BUBBLE

6.1 Abstract

Superparamagnetic iron oxide (SPIO) particles generate signal void regions on gradient echo images due to their strong magnetization. In practice, the signal void region might be indistinguishable from that generated by air. However, the response of SPIO to an externally applied magnetic field is non-linear. Magnetization of SPIO saturates at around 1 Tesla while magnetization of water and air increase linearly with field strength. Phantom experiment and mice experiments demonstrated the feasibility of a non-ambiguous identification of superparamagnetic contrast agents.

6.2 Introduction

Superparamagnetic iron oxide (SPIO) nanoparticles have been widely used as an MRI contrast agent (1-3). The strong magnetization of SPIO particles generates a local disturbance to the uniformly applied B0 field. This field disturbance leads to spin dephasing, resulting in signal void regions on MRI images (3). Therefore, T2* weighted pulse sequences have been used to image SPIO and have been considered to be the most sensitive. Recently, many efforts have been put into the detection and the estimation of SPIO (4-12). However, in general, it may prove difficult for gradient echo imaging to distinguish signal voids created by SPIO clusters from other sources of signal void such as the ones created by air. This becomes particularly problematic in molecular MRI when SPIO labeled cells are frequently embedded in porous gel phantoms for validation experiment (13) or when various air cavities obscure the

presence of nearby SPIO in animal experiments. In such procedures, an additional optical histological examination may be needed after MRI to validate the presence and location of SPIO particles (14).

Air bubbles create signal void regions because of both their lack of spins and the strong positive magnetization difference with the surrounding tissue ($\chi_{\text{air-water}}$ = 9.41ppm) (12). The magnetization of a SPIO cluster at practical concentrations may be very similar to that of air (relative to water), leading to similar dephasing and T2* effects. Therefore, the ambiguity may not be reliably solved.

In this study, we aim to improve the specificity of gradient echo based SPIO imaging. We hypothesize that by quantifying the magnetic moment of the signal void regions at two different field strengths, air and SPIO are distinguishable because the magnetization of SPIO saturates at around 1 Tesla while magnetization of air, water and tissue increase linearly with field strength. As part of the work, we introduce an improved quantitative susceptibility mapping (QSM) technique: improved Calculation Of Susceptibility through Multiple Orientation Sampling (iCOSMOS), and applied it to confirm the presence of SPIO by imaging at two different field strengths and exploiting the nonlinear response of SPIO. Phantom experiment and ex vivo mice experiments were conducted to demonstrate the feasibility of a non-ambiguous identification of SPIO particles.

6.3 Theory

A major magnetic characteristic of SPIO is its nonlinear response to the applied polarization magnetic field. SPIO in contrast agent Feridex (ferumoxides) saturates at

around 1T (2). For instance, the magnetization of ferumoxides at a concentration of 4mM Fe is 17.3A/m at 1.5T and 18.7A/m at 3T (2). However, magnetizations of air, water and tissue increase linearly with field strength. Figure 6.1 illustrates the magnetization and volume susceptibility curves of SPIO and air, where susceptibility is defined as (15):

$$\chi = M \times \mu_0 / B_0 \qquad [6.1]$$

We hypothesize that the difference in magnetizations obtained from two different fields can be used to distinguish non-linear SPIOs from other linear materials such as air and water. One way to demonstrate this difference is through quantitative susceptibility mapping. Here, we use an improved COSMOS method for reconstructing QSMs.

Figure 6.1. Illustration of magnetizations curves of SPIO and air. a) The magnetization of SPIO is calculated for ferumoxides at a concentration of 4mM Fe (23). The magnetization of air is proportional to the field strength with a constant susceptibility of 9.4ppm (24) b) Susceptibility curves of SPIO and air. Susceptibility values were calculated from Eq. 6.1

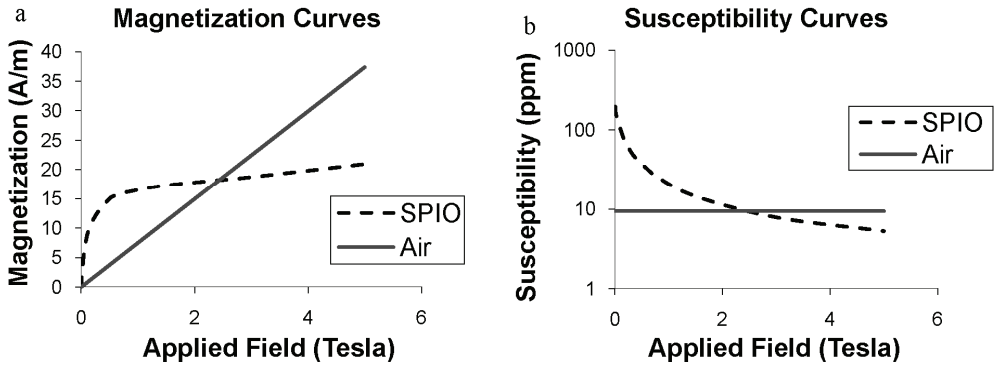

6.3.1 Improved COSMOS using regularization

Previously, we have demonstrated that by oversampling from multiple orientations, susceptibility is accurately quantifiable from the measured field map by eliminating the non-trivial null space in the dipole kernel (11). Nevertheless, oversampling cannot create new signal in signal void regions, including regions occupied by materials of high susceptibility, such as Feridex, and regions of little or no spins, such as air. In such situation, we make an assumption that susceptibility in a signal void region should be homogeneous because the materials in the void exhibit similar signal decay. Therefore, a smooth solution is favored in an isolated signal void region to eliminate solutions with sharp discontinuities.

To mathematically model this assumption, a Bayesian regularized quantitative susceptibility mapping technique that utilizes the gradient information from magnitude image was proposed in (16). This image gradient regularization is adopted with COSMOS, and the minimization problem is formulated as:

$$\chi^* = \text{argmin}_\chi \sum_{i=1}^{N} ||W_i(\delta_{Bi} - F_{Di}\chi)||_2^2 + \lambda^2 ||E\nabla\chi||_2^2 \qquad [6.2]$$

Where ∇ denotes a gradient operator and E is the weighting matrix derived from the magnitude image acquired at the first orientation. The detailed derivation of ∇ and E was elaborated in (16). λ is the regularization parameter. The regularization term provides a high penalty to the cost function if an edge on the reconstructed QSM does not have a corresponding edge on the magnitude image. It has been shown in (16) that the quantity of the solution is fairly independent of the choice of λ over two orders of

magnitude. Here, λ is fixed at 0.1 throughout the following experiments. After the QSM is derived, magnetization can be calculated from Eq. 6.1.

6.4 Methods and Materials

6.4.1 Numerical simulation

A numerical 3D phantom was designed to evaluate the influence of the regularization term to COSMOS. The phantom (Figure 6.2) consisted of a large sphere mimicking a water phantom, and multiple internal small spheres mimicking signal voids with radii ranging from 1 to 6 voxels. A uniform intensity of 20 was assigned to the "water" region. Susceptibility of the large sphere was set to 0 because water was usually chosen as reference. Then the background susceptibility and the susceptibility of the small spheres were set to 9.4ppm to simulate air. The field map was generated 3 times by using a forward calculation (15,17-18) and changing the direction of B_0 to 0º, 120º and 240º to simulate the reorientation process. A phase map was calculated from the field map assuming a TE of 1ms and B_0 of 1.5T. Zero-mean Gaussian white noise with a standard deviation of 1 was added to both the real and imaginary parts of the intensity image independently.

QSMs were subsequently reconstructed from the simulated MR data using original COSMOS and iCOSMOS by setting λ to 0 and 0.1, respectively. Means and standard deviations of the relative susceptibility values inside each small sphere were measured and compared.

6.4.2 Phantom and ex vivo validations

Two virtually identical cylindrical water containers were filled with tap water. The diameter of the containers was 70mm and the height was 25mm. Five vertical straws (diameter = 2.5mm, height = 25cm) were glued to the bottom of one of the container. One straw was left open to the outside air, while the four other straws were filled with 1.5, 3.0, 4.5 and 6.0% concentration of a Feridex solution (Advanced Magnetics, Inc., Cambridge, MA, USA) respectively.

A euthanized wild type adult mouse was imaged. The use of the mouse was approved by Institutional Animal Care and Use Committee (IACUC). 5μL of Feridex at a dilution factor of 10 was injected to the left thigh using a 100μL micro syringe immediately after the mouse was sacrificed. The mouse was subsequently immersed in a 50mL Falcon tube (Becton-Dickinson, Franklin Lake, N.J.) containing a saline solution. A second Falcon tube filled with the same volume of saline solution was used as a reference.

6.4.2.1 Data acquisition

The samples were scanned at both 1.5T and at 3T using clinical scanners. (General Electric Excite HDx; GE Healthcare, Waukesha, WI, USA). A dedicated 3D gradient-echo sequence was designed to sample at different TEs in an interleaved manner.

For the phantom scan, eight channel wrist coils with identical geometries (Invivo Corporation, Gainesville, FL) were used at both field strengths. Imaging parameters were identical at both field strengths. Field of view and matrix size were adjusted to achieve an isotropic resolution of 500mm. Bandwidth, TR, flip angle and number of excitations were ±125kHz/20ms/30º/1. Four TEs were chosen to achieve a balance

between the precision of the field map estimation and the total scan time: 2.3, 2.8, 4.8, and 14.84 ms. In order to use iCOSMOS as described in (11) for image analysis, the phantom was scanned from three orientations. After the first scan was finished, the phantom was rotated in the coronal plane by 120º for the second and by -120º for the third scan. The water phantom without the straws was also scanned as a reference scan to remove background inhomogeneity and the susceptibility effect caused by the air-phantom interface.

For the mouse scan, the tube containing the animal was placed vertically in a home-built birdcage mouse coil. Field of view and matrix size were adjusted to achieve an isotropic resolution of 500μm. At 1.5T, bandwidth, TR, flip angle and the number of excitations were ±31.25kHz/25ms/30º/2. Three TEs were acquired (2.8, 7.34, and 20.98ms). Note that TE spacing was an integer multiple of 4545μs, a period in which water and fat have consistent phase difference at 1.5T. Therefore, water fat separation (19) is not required to obtain the field map necessary for the iCOSMOS processing. At 3T, to achieve similar SNR and dephasing effects, the TR and the number of excitations were set to 15.6ms and 1. Three TEs were acquired (2.8, 5.07, and 11.89ms). The tube was also rotated in the coronal plane by 120º and -120º for the second and third scan, respectively. The tube filled with only water was also scanned as a reference to remove background field inhomogeneity and susceptibility effect from air-phantom interface.

6.4.2.2 Qualitative and Quantitative Distinction

Because the susceptibility of SPIO varies with field strength, while the susceptibilities

of other materials are field-strength independent, we subtract the QSMs reconstructed at 3T from the QSM reconstructions at 1.5T to obtain SPIO-specific images for qualitative distinctions.

Magnetization maps for 1.5T and 3T were directly calculated by scaling the QSMs with field strengths to determine the quantitative distinctions, as described in Eq. 6.1. As magnetization is the density of magnetic moment, it is subject to volume measurement errors, such as those caused by blooming artifacts (20). On the contrary, the magnetic moment is a physical quantity less sensitive to volume measurement errors. Therefore, on the reconstructed images, regions of interest (ROIs) were drawn over the signal void regions and magnetic moments in each ROI were calculated. Specifically, on the phantom data, five circles were drawn to cover the straws on the middle slice. Magnetic moment inside each circle was calculated by summing the magnetization of all the voxels, and multiplying the voxel size. On the mouse data, ellipses were drawn to cover the lungs and SPIO injection regions. Magnetic moments were calculated in a similar manner. Magnetic moment were subsequently converted to iron mass by the conversion factor $M = 77.3\times10^{-3}A\cdot m^2/g$ at 1.5T and $M = 83.65\times10^{-3}A\cdot m^2/g$ at 3T (2). Because the selected volume of each of the straws is 2.45 μL and iron concentration of pure Feridex is 11.2 mg/mL, expected iron mass inside the straws with the different Feridex concentrations (see above) is 0.41, 0.82, 1.24 and 1.65 μg, respectively. For the mouse injection, expected iron mass was 5.6μg. For both experiments, the ratio between the magnetic moments at 3T and 1.5T was calculated.

6.5 Results

For the numerically simulated experiment, QSM results are shown in Figure 6.2, and the means and standard deviations of measured susceptibilities in the signal voids are listed in Table 6.1. The regularization did not change the average susceptibility value (mean in Table 6.1), but it drastically reduced the susceptibility variations in the signal void (standard deviation in Table 6.1 and Figure 6.2c vs Figure 6.2d).

Figure 6.2. Numerical simulation of a susceptibility mapping experiment a) is the magnitude image. b) is the phase image). c) is the susceptibility map reconstructed from original COSMOS. d) is the susceptibility map reconstructed from regularized COSMOS. Note that regularized COSMOS has smoother distributions in signal voids.

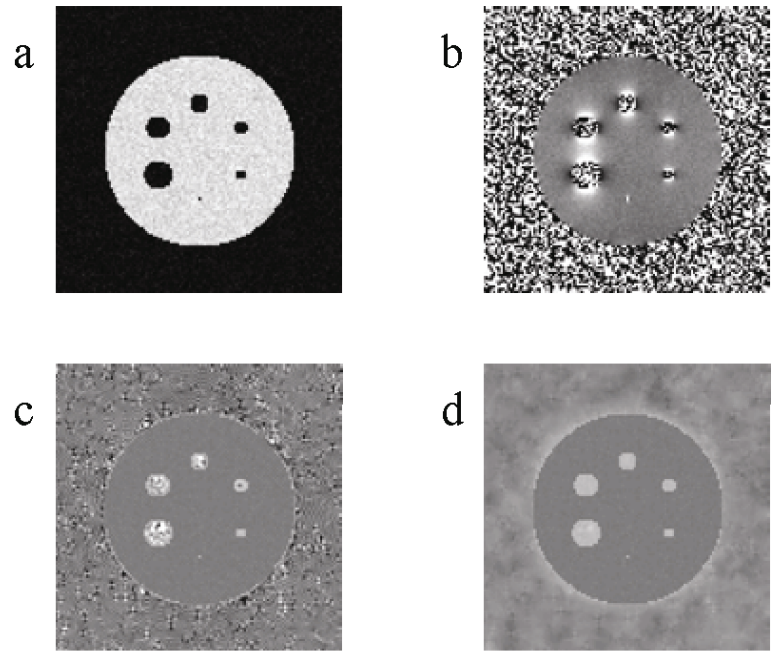

Table 6.1. Measured susceptibilities in different signal void spheres.(Mean±std)

Unit ppm	Radius = 1	Radius = 2	Radius = 3	Radius = 4	Radius = 5	Radius = 6
COSMOS	9.66	9.48±0.76	9.37±8.48	9.39±5.09	9.42±4.59	9.40±6.81
iCOSMOS	9.63	9.45±0.46	9.41±0.50	9.40±0.50	9.42±0.52	9.40±0.67

For the phantom experiment, Figure 6.3a&b show the magnitude of the gradient echo image. The straw containing air as well as the straws with high Feridex concentrations (above 3%) appeared as signal void regions. On the QSMs, both air and Feridex solution demonstrated positive susceptibility relatively to water. For qualitative distinction, straw containing air was almost cancelled out on the difference image due to the constant susceptibility difference between air and water, while Feridex-containing straws remained clearly visible because the susceptibility of SPIO varies with field strength (Figure 6.3e). For quantitative distinction, estimated magnetic moments and converted iron mass are listed in Table 6.2 and Table 6.3, respectively. The ratio of magnetic moments at 3T and 1.5T for air is approximately 2, indicating air's linear response to the applied field. The ratio of magnetic moments at 3T and 1.5T for Feridex is approximately 1, demonstrating SPIO's saturated response to applied field.

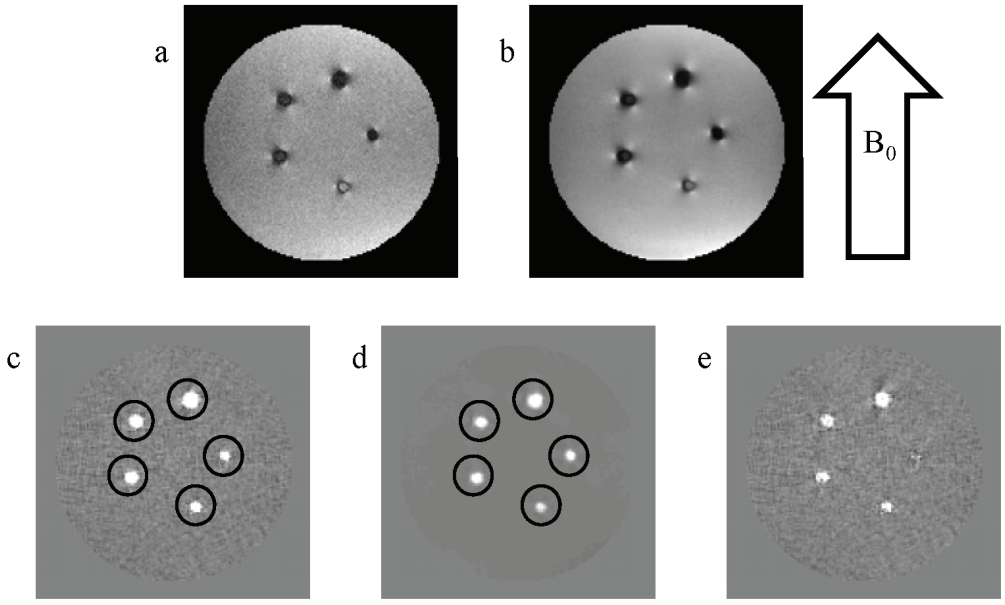

Figure 6.3. Phantom experimental results.

a) and b) are gradient echo images from 1.5T and 3T, respectively. The rightmost signal void region is the air straw, while other signal void regions contain Feridex solutions 1.5%, 3.0%, 4.5% and 6.0% in clockwise order. Air is indistinguishable from high concentrated Feridex solution on gradient echo images. Figures c) and d) show the quantitative susceptibility maps from 1.5T and 3T. The difference between 1.5T and 3T is shown on Fig e).

Table 6.2. Calculated magnetic moments.

Unit $nA \cdot m^2$	1.5% SPIO	3.0% SPIO	4.5% SPIO	6.0% SPIO	Air straw	Fe injection	Lung (air)
1.5T	35.1	67.8	93.2	124.6	27.0	273.8	101.0
3T	36.9	70.9	105.7	136.4	52.2	278.9	198.1

Table 6.3. MRI measured iron mass through quantitative susceptibility mapping.

Unit μg	1.5% SPIO	3% SPIO	4.5% SPIO	6% SPIO	Air straw	Fe injection	Lung (air)
1.5T	0.45	0.88	1.21	1.61	N/A	3.54	N/A
3T	0.44	0.85	1.26	1.63	N/A	3.33	N/A

In the mouse experiment, similar effects were observed. Air in the lung demonstrated an almost constant susceptibility, while susceptibility of SPIO varied with field strength. Magnetic moments and converted iron mass are listed in Table 6.2 and Table 6.3, respectively. The magnetic moment ratio between 3T and 1.5T was approximately 2 for air and approximately 1 for Feridex.

6.6 Discussion

Our preliminary data demonstrate that nonlinear SPIO can be distinguished from linear air by reconstructing the QSMs at two field strengths. Both air and highly concentrated SPIO regions appear as simple signal voids in standard magnitude gradient echo images. The susceptibility of air is independent of magnetic field strength, but the susceptibility of SPIO is approximately inversely proportional to the field strength. Using QSMs at 1.5T and 3T, SPIO can be differentiated from air, and the mass of the SPIO can be obtained.

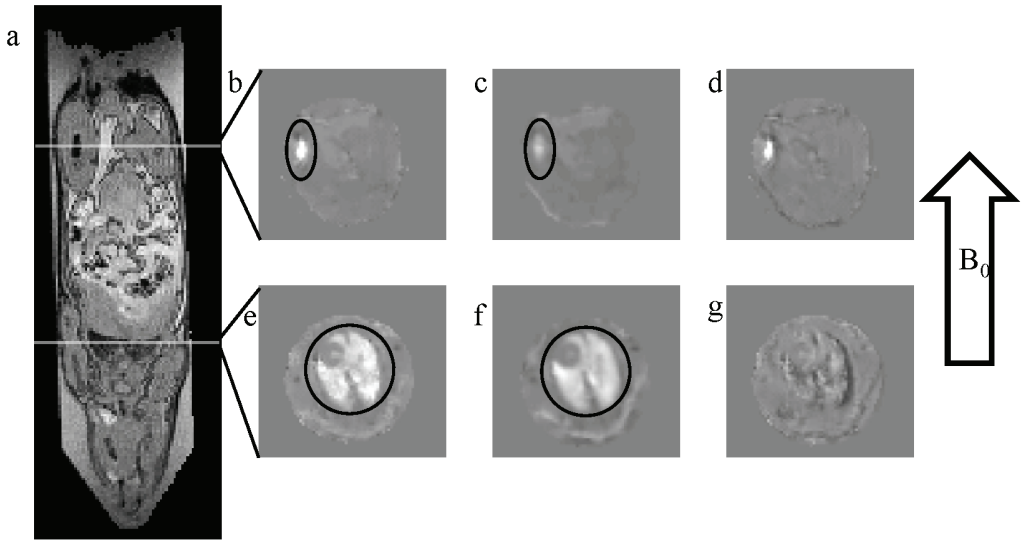

Figure 6.4. Mouse experimental results.

a) gradient echo image of a mouse at 3T. Both lung and the SPIO injection region appear to be signal void regions. b), c) susceptibility reconstructions at the cross section that contains the SPIO injection region from 1.5T and 3T, respectively. d) the difference between b) and c). e), f) susceptibility reconstructions at the cross section that contains lung. g) the difference between e) and f).

In the phantom experiment, the measured iron mass were in fair agreement with expected iron mass. In the mouse experiment, the measured iron mass was lower than the expected value by 37%. This discrepancy was consistent across two different field strengths, and was likely due to the injection protocol. Some Feridex solution may have diffused into the channel created by needle, or was displaced when the needle was withdrawn as commonly observed in such procedures.

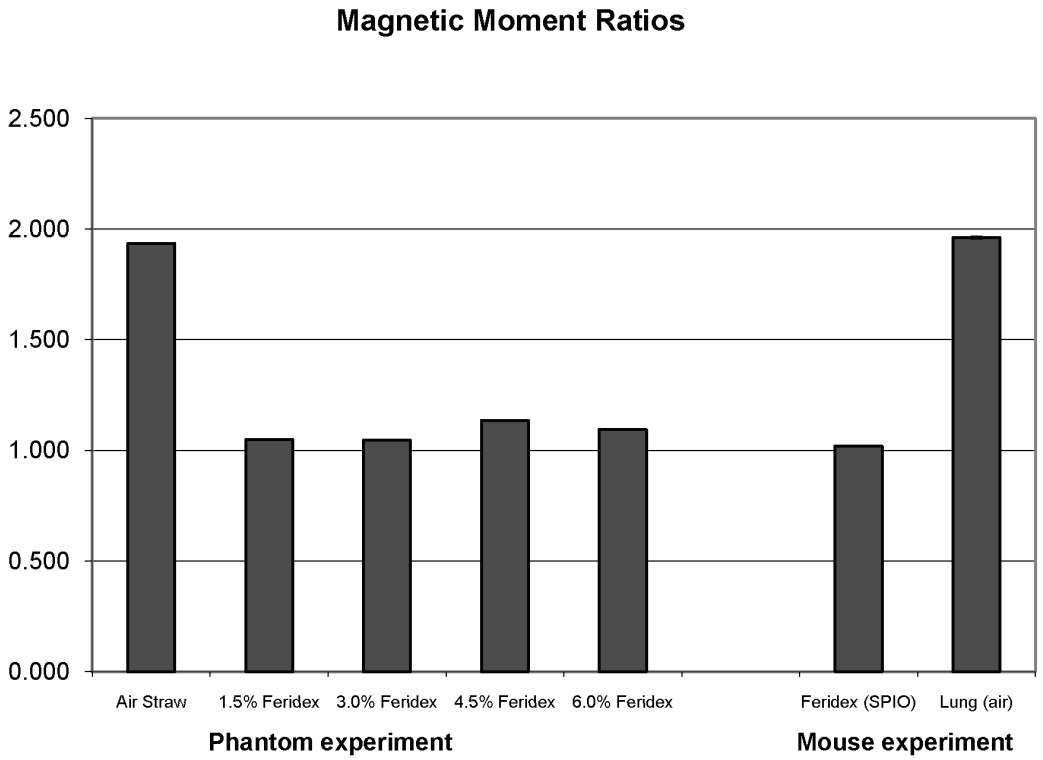

Figure 6.5. Magnetic moment ratios between 3T and 1.5T.

The left five columns are data from the phantom experiment. The right two columns are data from the ex vivo mouse experiment. Error bars, which correspond to the estimated noise level in the quantification, are smaller than the error of graphical display.

QSM in regions of no observable spins is intrinsically difficult, because only the total magnetic moment may be uniquely determined for a signal void region. For instance, two concentric spheres or long cylinders with different radii generate almost indistinguishable outside fields as long as they have identical magnetic moments (11,21). In this study, we introduced a regularization that preferred a smooth distribution in the signal void region for the COSMOS reconstruction method. The

gradient of the traditional magnitude image is used to identify the signal void region for smooth susceptibility assignment. A small regularization parameter that weighed heavily on data fidelity was chosen for the iCOSMOS. It has been shown in (16) that in this gradient regularization, the quantitative outcome is fairly insensitive to the choice of regularization parameter. The smallest regularization parameter tested in (16) was chosen and fixed throughout the experiment (λ=0.1).

Although the experiments were conducted at two specific field strengths 1.5T and 3T, in principle any two sufficiently different field strengths above 1T can be used, a condition satisfied by most current commercial scanners. A larger field difference would make the magnetic moment ratio greater for air, thus making it easier to distinguish SPIO from air. Currently, 1.5T and 3T scanners are widely available in all major medical centers, rendering applicability to general preclinical and clinical investigations.

The experimental results confirmed our hypothesis that air and SPIO are distinguishable in MRI by exploiting their different magnetization properties. Further improvement on the magnetization quantification is achievable to make the concept more practical. Several background field removal techniques that do not require reference scans have been proposed recently (22-24). Additionally, quantitative susceptibility mapping (QSM) is currently a research area progressing rapidly (25-27). Especially with advanced regularization techniques (16,27-29), only one scan at each field strength is required for susceptibility quantification, reducing the total scan time by 75%.

The idea of exploiting the nonlinear response of magnetic particles was inspired by the recent development of magnetic particle imaging (MPI). In MPI, the magnetic field oscillates and the electromagnetic response from a certain point in the space is received (30). Only magnetic particles with nonlinear response will cause higher harmonics to be recorded. The image space is sequentially scanned in a point-by-point manner. This MPI device provides a high scanning speed to verify SPIO with sensitivity and resolution warranting further investigation. The lack of background reference in MPI may require additional MRI or CT scans, while QSM through MRI conveniently provide relative susceptibility distribution to the background and anatomical structure.

6.7 Conclusion

In this study, we demonstrated that using quantitative susceptibility mapping in MRI at two field strengths, the non-linear response of SPIO particles allows distinction of SPIO from linear materials such as air, water and tissue. Quantifying susceptibility at two different field strengths allows SPIO-specific imaging.

6.8 Acknowledgement

This investigation was supported in part by grant UL1RR024996 of the Clinical and Translation Science Center at Weill Cornell Medical College.

6.9 Reference

1. Bulte JW, Kraitchman DL. Iron oxide MR contrast agents for molecular and cellular imaging. NMR Biomed 2004;17(7):484-499.

2. Jung CW, Jacobs P. Physical and chemical properties of superparamagnetic iron oxide MR contrast agents: ferumoxides, ferumoxtran, ferumoxsil. Magn Reson Imaging 1995;13(5):661-674.

3. Wang YX, Hussain SM, Krestin GP. Superparamagnetic iron oxide contrast agents: physicochemical characteristics and applications in MR imaging. Eur Radiol 2001;11(11):2319-2331.

4. Cunningham CH, Arai T, Yang PC, McConnell MV, Pauly JM, Conolly SM. Positive contrast magnetic resonance imaging of cells labeled with magnetic nanoparticles. Magn Reson Med 2005;53(5):999-1005.

5. Edelman RR, Storey P, Dunkle E, Li W, Carrillo A, Vu A, Carroll TJ. Gadolinium-enhanced off-resonance contrast angiography. Magn Reson Med 2007;57(3):475-484.

6. Faber C, Heil C, Zahneisen B, Balla DZ, Bowtell R. Sensitivity to local dipole fields in the CRAZED experiment: an approach to bright spot MRI. J Magn Reson 2006;182(2):315-324.

7. Koktzoglou I, Li D, Dharmakumar R. Dephased FLAPS for improved visualization of susceptibility-shifted passive devices for real-time interventional MRI. Phys Med Biol 2007;52(13):N277-286.

8. Mani V, Briley-Saebo KC, Itskovich VV, Samber DD, Fayad ZA. Gradient echo acquisition for superparamagnetic particles with positive contrast (GRASP): sequence characterization in membrane and glass superparamagnetic iron oxide

phantoms at 1.5T and 3T. Magn Reson Med 2006;55(1):126-135.

9. Stuber M, Gilson WD, Schar M, Kedziorek DA, Hofmann LV, Shah S, Vonken EJ, Bulte JW, Kraitchman DL. Positive contrast visualization of iron oxide-labeled stem cells using inversion-recovery with ON-resonant water suppression (IRON). Magn Reson Med 2007;58(5):1072-1077.

10. Dixon WT, Blezek DJ, Lowery LA, Meyer DE, Kulkarni AM, Bales BC, Petko DL, Foo TK. Estimating amounts of iron oxide from gradient echo images. Magn Reson Med 2009.

11. Liu T, Spincemaille P, de Rochefort L, Kressler B, Wang Y. Calculation of susceptibility through multiple orientation sampling (COSMOS): a method for conditioning the inverse problem from measured magnetic field map to susceptibility source image in MRI. Magn Reson Med 2009;61(1):196-204.

12. de Rochefort L, Brown R, Prince MR, Wang Y. Quantitative MR susceptibility mapping using piece-wise constant regularized inversion of the magnetic field. Magn Reson Med 2008;60(4):1003-1009.

13. Shapiro EM, Skrtic S, Sharer K, Hill JM, Dunbar CE, Koretsky AP. MRI detection of single particles for cellular imaging. Proc Natl Acad Sci U S A 2004;101(30):10901-10906.

14. Heyn C, Ronald JA, Mackenzie LT, MacDonald IC, Chambers AF, Rutt BK, Foster PJ. In vivo magnetic resonance imaging of single cells in mouse brain with optical validation. Magn Reson Med 2006;55(1):23-29.

15. Marques JP, Bowtell R. Application of a Fourier-based method for rapid calculation of field inhomogeneity due to spatial variation of magnetic susceptibility. Concepts in Magnetic Resonance Part B: Magnetic Resonance Engineering 2005;25B(1):65-78.

16. de Rochefort L, Liu T, Kressler B, Liu J, Spincemaille P, Lebon V, Wu J, Wang Y. Quantitative susceptibility map reconstruction from MR phase data using bayesian regularization: validation and application to brain imaging. Magn Reson Med 2010;63(1):194-206.

17. Koch KM, Papademetris X, Rothman DL, de Graaf RA. Rapid calculations of susceptibility-induced magnetostatic field perturbations for in vivo magnetic resonance. Phys Med Biol 2006;51(24):6381-6402.

18. Salomir R, De Senneville BD, Moonen CTW. A fast calculation method for magnetic field inhomogeneity due to an arbitrary distribution of bulk susceptibility. Concepts in Magnetic Resonance Part B-Magnetic Resonance Engineering 2003;19B(1):26-34.

19. Glover GH, Schneider E. Three-point Dixon technique for true water/fat decomposition with B0 inhomogeneity correction. Magn Reson Med 1991;18(2):371-383.

20. Akter M, Hirai T, Hiai Y, Kitajima M, Komi M, Murakami R, Fukuoka H, Sasao A, Toya R, Haacke EM, Takahashi M, Hirano T, Kai Y, Morioka M, Hamasaki K, Kuratsu J, Yamashita Y. Detection of hemorrhagic hypointense foci in the brain on susceptibility-weighted imaging clinical and phantom studies. Acad Radiol

2007;14(9):1011-1019.

21. Haacke EM, Brown RW, Thompson MR, R. V. Objects in external fields: the Lorentz sphere. Magnetic resonance imaging: physical principles and sequence design. New York: Wiley-Liss; 1999. p 749-757.

22. Wharton S, Schafer A, Bowtell R. Susceptibility mapping in the human brain using threshold-based k-space division. Magn Reson Med 2010;63(5):1292-1304.

23. Liu T, Khalidov I, Rochefort Ld, Spincemaille P, Liu J, Wang Y. Improved Background Field Correction Using Effective Dipole Fitting. ISMRM. Stockholm, Sweden; 2010. p 141.

24. Schweser F, Lehr BW, Deistung A, Reichenbach JR. A Novel Approach for Separation of Background Phase in SWI Phase Data Utilizing the Harmonic Function Mean Value Property. ISMRM. Stockholm, Sweden; 2010. p 142.

25. Schweser F, Hütten M, Lehr BW, Deistung A, Güllmar D, Reichenbach JR. Resolving Phase: Inversion of SWI-Phase Data in Order to Obtain Its Sources Utilizing the Concept of a Generalized Lorentzian Approximation. ISMRM. Stockholm, Sweden; 2010. p 5003.

26. Liu C. Susceptibility Tensor Imaging. ISMRM. Stockholm, Sweden; 2010. p 700.

27. Liu J, Liu T, Rochefort Ld, Khalidov I, Prince MR, Wang Y. Quantitative Susceptibility Mapping by Regulating the Field to Source Inverse Problem with a Sparse Prior Derived from the Maxwell Equation: Validation and Application to Brain

ISMRM. Stockholm, Sweden; 2010. p 4996.

28. Kressler B, de Rochefort L, Liu T, Spincemaille P, Jiang Q, Wang Y. Nonlinear Regularization for Per Voxel Estimation of Magnetic Susceptibility Distributions From MRI Field Maps. IEEE Trans Med Imaging 2009.

29. Shmueli K, de Zwart JA, van Gelderen P, Li TQ, Dodd SJ, Duyn JH. Magnetic susceptibility mapping of brain tissue in vivo using MRI phase data. Magn Reson Med 2009;62(6):1510-1522.

30. Gleich B, Weizenecker J. Tomographic imaging using the nonlinear response of magnetic particles. Nature 2005;435:1214-1217.

CHAPTER 7

7 MEASUREMENT OF CEREBRAL MICROBLEED BURDEN

7.1 Abstract

Purpose: To study the feasibility of using quantitative susceptibility mapping (QSM) for the characterization of cerebral microbleed (CMB) burden in MRI.

Materials and Methods: Our institutional review boards approved this retrospective HIPAA-compliant study. Ten patients were imaged with a multi-echo gradient echo sequence on 3T scanners. QSM was performed for various ranges of echo times (TE) using both the magnitude and phase components by the morphology enabled dipole inversion (MEDI) method. CMB sizes were measured by a neuroradiologist on QSM, T2* weighted images (T2*W), susceptibility weighted images (SWI) and R2* maps calculated using different TE values. The total susceptibility of each CMB was also estimated on QSM.

Results: When TE was increased from approximately 20ms to 40ms, the measured CMB volume increased by a factor of 1.25±0.37, 1.66±0.60, 2.02±0.97 and 2.14±1.06 for QSM, R2*, T2*W and SWI, respectively ($P<0.01$ for each). However, the measured total susceptibility did not show any significant dependence on the choice of echo time ($P=0.36$).

Conclusion: The total susceptibility of CMB is a physical property independent of echo time and this is experimentally confirmed on QSM. Using total susceptibility to measure CMBs overcomes the sensitive dependence on TE in CMB size

measurement, offering a more objective means to characterize CMB burden.

7.2 Introduction

Cerebral microbleeds (CMB) indicate prior extravasation of blood from rupture of cerebral arterioles damaged by hyaline degeneration and microaneurysm formation caused by longstanding hypertension or aging, and signify the presence of an underlying bleeding-prone microangiopathy (1-4). There are substantial research interests in the predictive value of CMB severity for the incidence or the recurrence of primary intracerebral hemorrhage (5-8), and its association with hypertension, diabetes mellitus, cerebral amyloid angiopathy, cognitive deficits (9-10), neurologic outcome after nonaccidental childhood trauma (11) and traumatic brain injury (12). Additionally, recent studies also indicate that CMB burden is strongly and independently related to intracerebral hemorrhage incidence in patients with anticoagulants (13-14). Thus, there is a pressing need to assess the diagnostic and prognostic utility of CMB and determine whether they influence treatment.

T2* weighted (T2*W) gradient echo (GRE) magnetic resonance imaging (MRI) is the method of choice to study CMB (3). However, CMB appearances as small hypointensity regions vary significantly with field strength, flip angle, slice gap and slice thickness, and there are inconsistencies in defining CMB size (3). The presence, number, distribution and especially the size of round parenchymal signal voids have been traditionally used to characterize CMB burden (3, 15), but this characterization is very sensitive to the choice of echo time (TE) that substantially affect the size of the signal void (16). There is an urgent need to establish “a shared set of standards for the

detection of microbleeds that will enable informative cross-study comparisons and robust longitudinal data collection" (3, 17). Advanced image processing including SWI can improve the conspicuity of CMB (18), but the resulting image is still highly TE dependent.

In this study, we hypothesize that hemosiderin deposits in CMB can be quantified independent of TE using quantitative susceptibility mapping (QSM). Susceptibility is an intrinsic physical property of a material that can be determined from local magnetic field by deconvolution with a dipole kernel (19-29). We retrospectively analyzed 40 CMB detected in 10 patients by comparing QSM with R2*, T2*W and SWI to investigate whether QSM can overcomes the sensitive dependence on TE for measuring the CMB burden.

7.3 Methods and Materials

7.3.1 Data Acquisition

This retrospective analysis of existing patient data was approved by our Institutional Review Boards in compliance with the Health Insurance Portability and Accountability Act. Ten patients with CMBs were imaged on 3.0T MR scanners (HDx, GE Healthcare, Waukesha, WI, USA) using an 8-channel birdcage head coil and a 3D multi-echo spoiled gradient echo sequence (SWAN). Imaging parameters included axial planes covering the brain; number of TEs: 7~10; first TE: 4.9~13 ms; uniform TE spacing (Δte): 3.8~5.2 ms; TR: 39.8~67.6 ms; flip angle: 15°~25°; bandwidth per pixel: 244 Hz; field of view: 24cm ×19.2~24cm ×7.2~18 cm; acquisition matrices: 240~448 ×180~384 ×36~60. Parallel imaging (ASSET) was used

with a reduction factor of two.

7.3.2 Data Reconstruction

The reconstruction of QSM from measured phase data is an ill-posed inverse problem that many solutions can generate a field that is virtually identical to the field derived from phase data (30). Here, we formulate this inverse problem as a weighted l1 minimization problem (31-32). Among all the candidate solutions, the estimated susceptibility distribution χ^* (Figure 7.1f) is the one whose edges have the sparsest differences from those of the anatomical image. This spatial prior helps to eliminate solutions with spurious edges resulting from streaking artifacts often seen in QSM (26), and determines a solution that is physically meaningful. A schematic view of this morphology enabled dipole inversion (MEDI) approach is shown in Figure 7.1. For each patient and for each echo time *te*, a quantitative susceptibility map (QSM) was calculated using all echoes up to *te*.

Figure 7.1. Schematic view of the QSM reconstruction.

The square root of the sum of squares of the magnitude images from multiple echoes (a) formed an anatomical image P (b). An automatic brain extraction algorithm (25) was used to mask out the non brain region. A simple threshold method was used to set the non-negligible gradients on P to zero while others to one to generate the gradient weighting term M (b). Both the magnitude (a) and phase images (c) were use to estimate the data weighting term W (d) and field map f (e)(18). The spatial unwrapping of the field map was accomplished using a quality map guided region growing algorithm (26). The Projection onto Dipole Fields method was subsequently

used to estimate the local magnetic field f_L. Finally, the QSM (f) was reconstructed using the morphology enabled dipole inversion method.

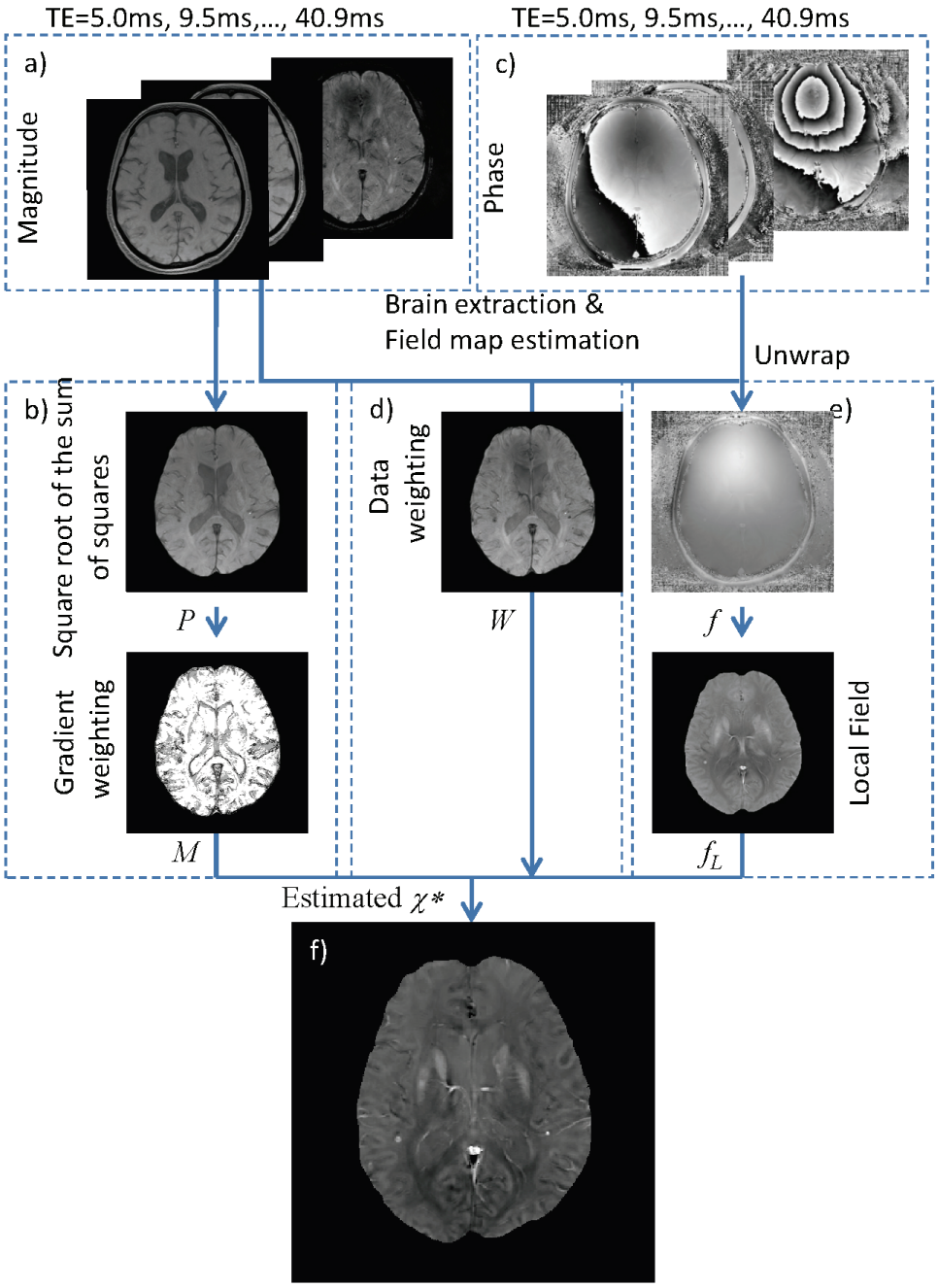

7.3.3 Data Analysis

7.3.3.1 Evaluation of the QSM

To analyze the variations of both the contrast and noise of QSM over a range of TEs, the reconstructed QSM were plotted over TE for visual inspection to assess the TE dependence. For each patient, one slice of globus pallidus was manually segmented on QSM at TE≈40ms, and the segmented template was applied to other echoes. The contrast of the QSM is defined as the mean susceptibility value of globus pallidus, and the noise of the QSM at TE=*te* was defined as the standard deviation of the difference between the QSM at TE=*te*-Δ*te* and the QSM at TE=*te*. For each patient, contrast measured at TE≈40ms was divided by contrast measured at TE≈20ms to obtain a contrast ratio dependence on TE, and a similar noise ratio dependence on TE was obtained.

An experienced neuroradiologist identified all the microbleeds on the magnitude image at TE≈40ms in the following manner. A round or ovoid hypointense lesion whose diameter was greater than 2mm but smaller than 10mm was considered to be a microbleed. The ROIs were subsequently co-registered to the QSM. For each ROI, a 1×1×1cm3 cubic ROI was placed at the center of the microbleed to calculate the CMB's total susceptibility. Voxels inside the cube whose susceptibility values were greater than 0.05ppm were considered as part of the microbleed, and the susceptibility of all selected voxels was summed up to calculate the total susceptibility: $m = \sum_R \chi \times \Delta v$, where m denotes the total susceptibility of a CMB, R denotes the region of selected voxels and Δv is the voxel size. The total susceptibility was further used as an

indicator of CMB burden and was compared with the size measurement in the next section.

QSM profiles traversing the globus pallidus, the internal capsule and the thalamus were examined for the influence of TE on the susceptibility variation. A linear regression was performed between the total susceptibility and TEs. The noise on the QSM was fitted to a power function.

7.3.3.2 Comparison with R2* map, SWI and T2*W:

Similar to the QSM, an R2* map using a monoexponential fit was obtained for each echo time *te* by selecting all echoes up to this echo time. For each echo time, a Susceptibility Weighted Image (SWI) was generated by multiplying the magnitude image with a corrected phase image raised to the 4^{th} power (33), and a T2*W images was retained. The diameter d_M of each microbleed was measured on QSM, R2*, SWI and T2*W for each TE to assess TE dependence. For a consistent comparison with the total susceptibility over a volume, the microbleed diameters were further converted into microbleed volumes assuming a spherical shape of the microbleed: $V=1/6\pi d_M^3$. To quantitatively assess the volume of a microbleed for each TE, the volume ratio of a microbleed at TE=*te* was calculated as the ratio of volumes measured at TE=*te* and TE≈20ms (minimum TE for CMB suggested in literature (3)). Similarly, total susceptibility ratio was calculated as the ratio of total susceptibilities estimated at TE=*te* and TE≈20ms. Linear regression was performed between the total susceptibility of each CMB and its T2*W image volume at the same TE. A histogram of the total susceptibility of all the CMB in all the patients was generated to analyze its

distribution.

7.3.4 Statistical Analysis

For all the ratio measurements, the results were reported in mean±standard deviation, and the Student's t test was used to assess the difference significance. For the linear regressions, the F-test was performed to assess significance. The statistical evaluations were conducted on Excel 2007 (Microsoft, Redmond, WA).

7.4 Results

CMB findings are summarized in Table 7.1. The measured contrasts of the QSM was independent of the number of employed echoes (contrast ratio=1.04±0.12, P=0.31), but the noise decreased with more echoes (noise ratio=0.29±0.08, P<0.01). This is exemplarily illustrated in Figure 7.2. There was no substantial variation in QSM profiles of all TEs in Figure 7.2d. The microbleed total susceptibility did not show a significant linear dependence on the choice of echo time (slope = -0.032, P = 0.50) (Figure 7.2e). QSM noise decayed monotonically with increasing TE (exponent = -1.17, close to inverse TE) (Figure 7.2f).

The TE independence of total susceptibility of CMB is further illustrated in another example in Figure 7.3, which also includes volume measurements and QSM comparison with T2*W, SWI, and R2*. The susceptibility ratio did not change substantially while the volume ratio increased with TE (Figure 7.3a). All the microbleeds identified on T2*W were also detected on SWI, R2* map and QSM at the same echo time (TE≈40 ms). The diameter of the microbleed exhibited substantial enlargement with TE on T2*W (Figure 7.3b&c) and SWI (Figure 7.3d&e). The

enlargement was moderate on R2* (Figure 7.3f&g) and substantially reduced on QSM (Figure 7.3h&i).

Table 7.1. CMB finding summary

Patient	Number of CMBs	Total Susceptibility (ppm·μL)
1	3	38.7
2	3	11.6
3	9	130.3
4	8	131.8
5	1	8.0
6	5	16.6
7	3	6.6
8	2	5.4
9	5	29.8
10	1	4.9

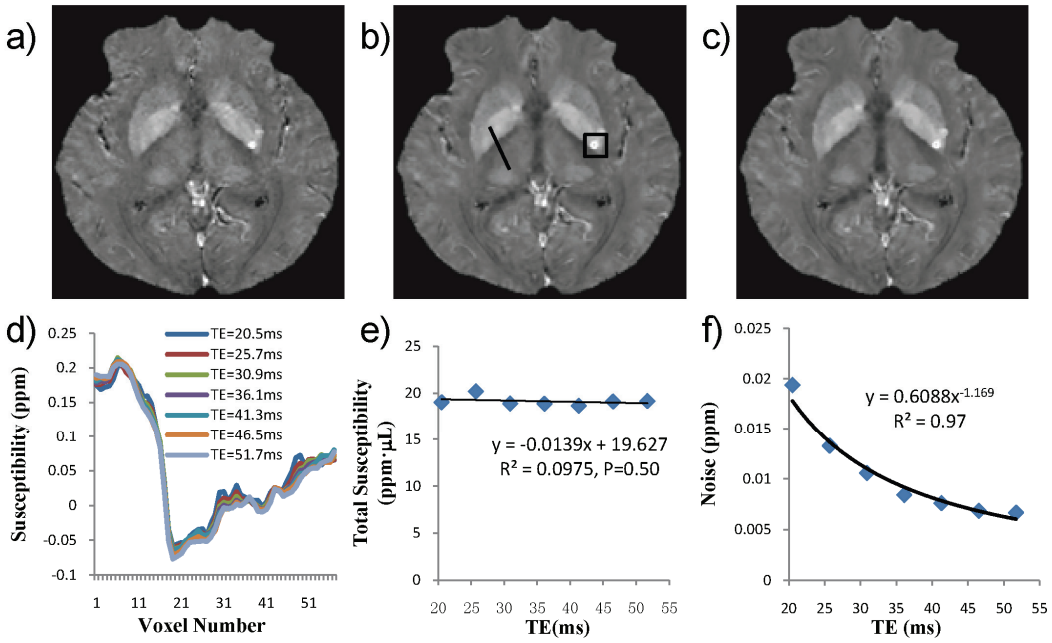

Figure 7.2. Qualitative and quantitative analysis of the QSM at different TEs. a-c) QSM reconstructed at TE=20.5ms (a), 41.3ms (b) and 51.7ms(c) do not show TE dependence by visual inspection. The window/level of the QSM is adjusted to from -0.2 to 0.4 ppm, a dark line in b) marks for profiling and a dark square in b) for total susceptibility measurement. d&e) The TE independency of the QSM is quantitatively confirmed by the susceptibility measured along a line profile (d), and by the total susceptibility of the microbleed at various TEs (e). f) The noise of the QSM decays monotonically with increasing TE.

For all 40 microbleeds, the volume ratios at TE≈40ms were 1.25±0.37, 1.66±0.60, 2.02±0.97 and 2.14±1.06 for QSM, R2*, T2*W and SWI, all larger than one ($P<0.01$). The total susceptibility ratio at TE≈40ms was 1.03±0.22, not significantly different from one ($P=0.36$). There was no correlation between the total susceptibility and the volumes of the CMB (measured at TE≈40ms) ($P=0.57$) (Figure 7.4b). The total susceptibilities in 37 of 40 microbleeds were smaller than 25ppmµL (Figure 7.4c).

*Figure 7.3. Comparison with R2*map, T2*W and SWI on a representative case. a) The volume of the microbleed monotonically increased with an increasing TE on all the images as indicated by the volume ratios (V-T2*W, V-SWI, V-R2* and V-QSM). However, the total susceptibility ratio did not demonstrate significant TE dependence (P=0.47). b-i) T2*W, SWI, R2* map and QSM of the same microbleed are shown at TE=19.5ms (b, d, f, h) and at TE=38.7ms (c, e, g, i). The arrow in (b) is pointing at the measured microbleed. The window/level of the QSM is adjusted to from -0.1 to 0.2 ppm.*

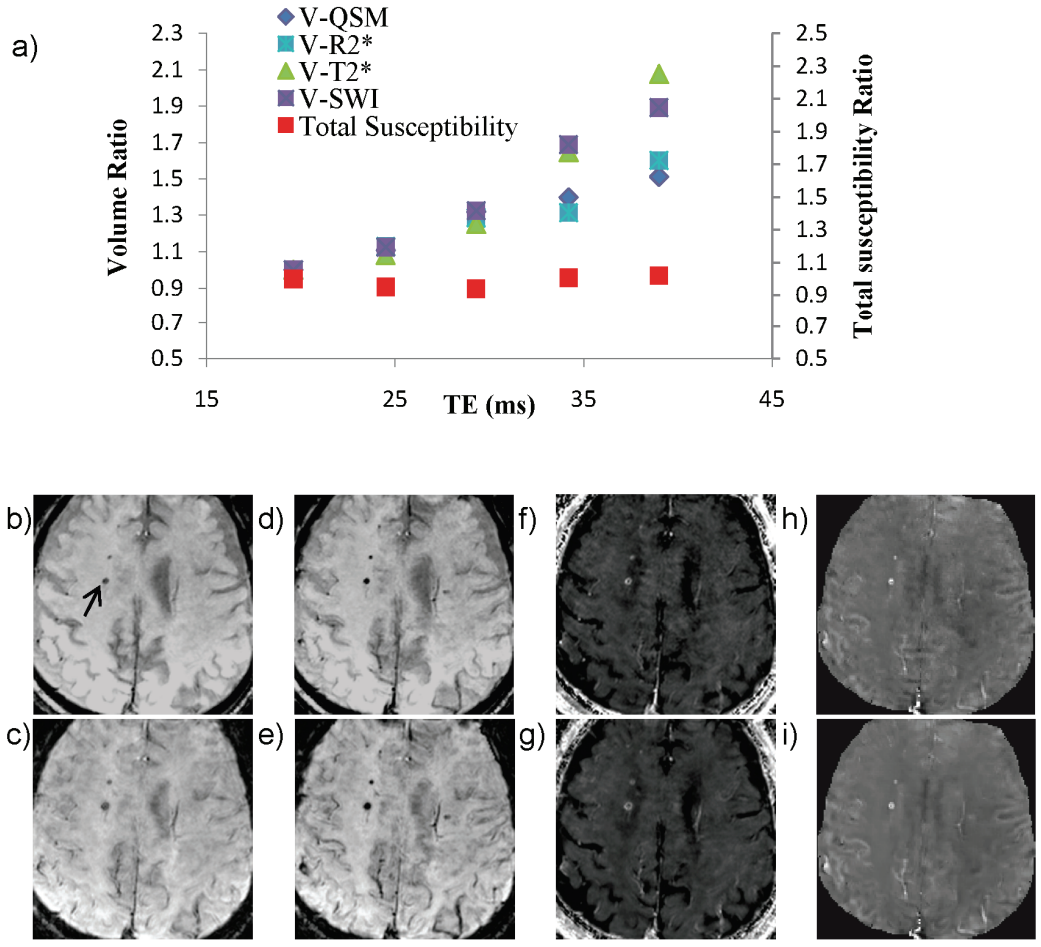

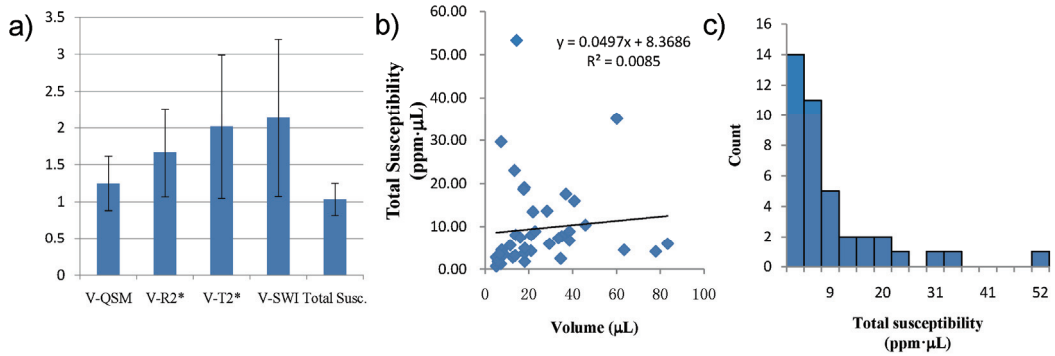

*Figure 7.4. Comparison with R2*map, T2*W and SWI across all the patients. a) All the volume ratios (V-T2*W, V-SWI, V-R2* and V-QSM) at TE≈40ms substantially deviated from one. However, the total susceptibility ratio did not show statistically significant difference than one (P=0.36). b) There is no statistical significant correlation between total susceptibility and volume, either (P = 0.57). The histogram of the total susceptibility of all the CMB is shown in (c).*

7.5 Discussion

Our preliminary data demonstrated the feasibility to apply QSM in patients with CMB and confirmed that the total susceptibility of a microbleed is independent of echo time.

Total magnetic susceptibility of a CMB overcomes the TE dependence in the size measurement in the previous approach to characterize CMB burden. Geometric measurement in gradient echo MRI and its derivatives (including T2*W, SWI and R2*) fundamentally suffer from inherent blooming artifacts (34): hypointensity at a voxel only indicates field variation there, but the field sources may be in neighboring regions. The dipole deconvolution in QSM can theoretically eliminate this blooming artifacts when proper prior information is used such as morphology derived from images with no or little blooming artifacts. Our current QSM uses a composite T2*W

magnitude and gets contaminated moderately by the blooming artifacts, which leads to the minor volume increase on the calculated QSM and consequently a decrease in the estimated volume susceptibility of the CMBs. It is shown here that even in the current MEDI implementation, the integration of susceptibility over volume, the total susceptibility, is independent of echo time. This in vivo TE independency is in accordance with previous phantom and ex vivo validations (35), in which QSM have shown to be able to accurately quantify the amount of iron.

Susceptibility of CMB primarily comes from hemosiderin deposits, reflecting the amount of iron that is recognized as an important factor for brain injury in intracerebral hemorrhage (36-37). Accordingly, there are increasing interests in the magnetism of hemorrhages (38-39). Since total susceptibility is a reliable measurement independent of the blooming artifacts and partial volume effects in the case of very small microbleeds, it may be a more useful measurement than volume. The lack of correlation between volume and total susceptibility in our data indicates there is significant variation in volume susceptibility or iron concentration. Further study is needed to investigate the relation between total susceptibility, volume susceptibility, neurologic damage and risk in disease and medication. For example, CMB burden via QSM may be a valuable indicator for prognosis of children with acute non-accidental head trauma (11) and for assessing the hemorrhage risk in patients under anticoagulation such as taking warfarin (13-14).

The noise on QSM decreases with increasing echo time because a longer TE allows more dephasing for accurate field map estimation. The contrast of QSM, which is determined by tissue susceptibility, is independent of TE. This physical principle

supports the use of the QSM to characterize CMB burden. It is preferable to have a short TE to capture the morphology and field information before the signal in a voxel decays to the noise level due to surrounding strong susceptibility sources, and a long TE to reduce the noise on the QSM to improve sensitivity for weak susceptibility sources. This multiple echo GRE sequence offers the benefit of simultaneous acquisition of all echo times in one excitation.

Figure 7.5. Iron and calcium deposits on R2 and QSM.*

a) Both iron in basal ganglia and calcium deposits in the lateral ventricle appear to be hyperintense in the R2 map. b) Paramagnetic iron deposits have positive values and diamagnetic calcium deposits have negative values on QSM. The window/level of the QSM is adjusted to from -0.1 to 0.2 ppm.*

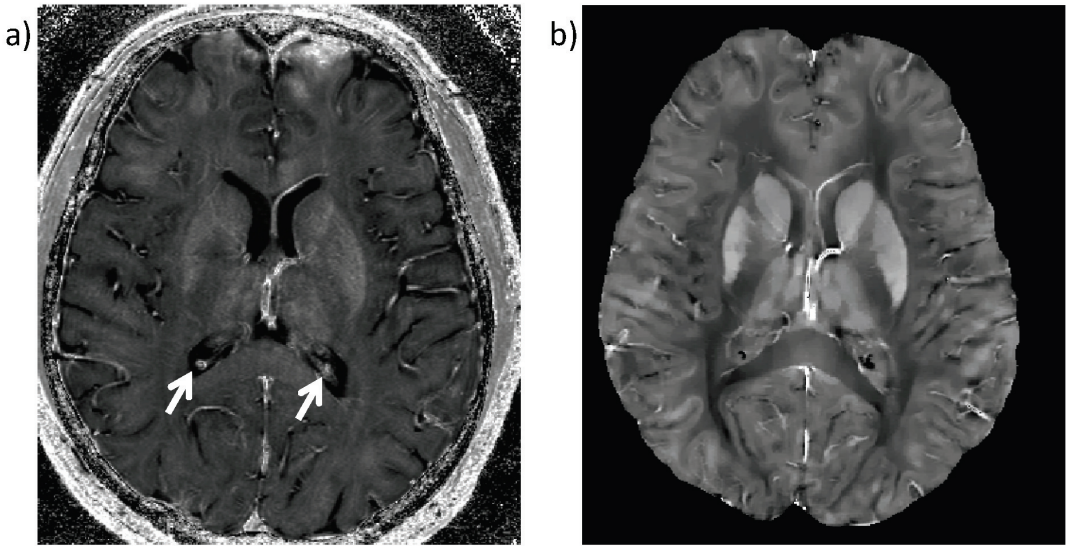

In this study, we did not measure the total hypointensities of CMB in T2*W and SWI images. These hypointense regions mostly contain noise. Consequently, the total hypointensities would be just volume times noise level, which does not provide useful information in addition to the volume of CMB. We also did not measure the total R2* value of CMB. Both iron and calcium deposits generate similar appearance in R2* maps (arrow in Figure 7.5a) while QSM is able two differentiate them based on their magnetisms (Figure 7.5b and (25)). The measured R2* value is also subject to T2 quench effect (40). Therefore, total R2* measurement of CMB may not serve the optimal candidate for characterizing CMB burden.

In summary, the total susceptibility of a CMB is an intrinsic physical property independent of echo time, and this is confirmed experimentally on QSM. Characterization of CMB using total susceptibility overcomes the dependence on TE of CMB size measurement in GRE MRI, offering a more objective means to characterize CMB burden.

7.6 Reference

1. Jeerakathil T, Wolf PA, Beiser A, et al. Stroke risk profile predicts white matter hyperintensity volume: the Framingham Study. Stroke. 2004;35(8):1857-61.

2. Fazekas F, Kleinert R, Roob G, et al. Histopathologic analysis of foci of signal loss on gradient-echo T2*-weighted MR images in patients with spontaneous intracerebral hemorrhage: evidence of microangiopathy-related microbleeds. AJNR Am J Neuroradiol. 1999;20(4):637-42.

3. Greenberg SM, Vernooij MW, Cordonnier C, et al. Cerebral microbleeds: a guide to detection and interpretation. Lancet Neurol. 2009;8(2):165-74.

4. Vernooij MW, van der Lugt A, Ikram MA, et al. Prevalence and risk factors of cerebral microbleeds: the Rotterdam Scan Study. Neurology. 2008;70(14):1208-14.

5. Lee SH, Bae HJ, Kwon SJ, et al. Cerebral microbleeds are regionally associated with intracerebral hemorrhage. Neurology. 2004;62(1):72-6.

6. Lee SH, Kim BJ, Roh JK. Silent microbleeds are associated with volume of primary intracerebral hemorrhage. Neurology. 2006;66(3):430-2.

7. Fan YH, Zhang L, Lam WW, Mok VC, Wong KS. Cerebral microbleeds as a risk factor for subsequent intracerebral hemorrhages among patients with acute ischemic stroke. Stroke. 2003;34(10):2459-62.

8. Greenberg SM, Eng JA, Ning M, Smith EE, Rosand J. Hemorrhage burden predicts recurrent intracerebral hemorrhage after lobar hemorrhage. Stroke.

2004;35(6):1415-20.

9. Kirsch W, McAuley G, Holshouser B, et al. Serial susceptibility weighted MRI measures brain iron and microbleeds in dementia. J Alzheimers Dis. 2009;17(3):599-609.

10. Yakushiji Y, Nishiyama M, Yakushiji S, et al. Brain microbleeds and global cognitive function in adults without neurological disorder. Stroke. 2008;39(12):3323-8.

11. Colbert CA, Holshouser BA, Aaen GS, et al. Value of cerebral microhemorrhages detected with susceptibility-weighted MR Imaging for prediction of long-term outcome in children with nonaccidental trauma. Radiology. 2010;256(3):898-905.

12. Akiyama Y, Miyata K, Harada K, et al. Susceptibility-weighted magnetic resonance imaging for the detection of cerebral microhemorrhage in patients with traumatic brain injury. Neurol Med Chir (Tokyo). 2009;49(3):97-9; discussion 9.

13. Lee GH, Kwon SU, Kang DW. Warfarin-induced intracerebral hemorrhage associated with microbleeds. J Clin Neurol. 2008;4(3):131-3.

14. Lee SH, Ryu WS, Roh JK. Cerebral microbleeds are a risk factor for warfarin-related intracerebral hemorrhage. Neurology. 2009;72(2):171-6.

15. Cordonnier C, Al-Shahi Salman R, Wardlaw J. Spontaneous brain microbleeds: systematic review, subgroup analyses and standards for study design and reporting. Brain. 2007;130(Pt 8):1988-2003.

16. Vernooij MW, Ikram MA, Wielopolski PA, Krestin GP, Breteler MM, van der Lugt A. Cerebral microbleeds: accelerated 3D T2*-weighted GRE MR imaging versus conventional 2D T2*-weighted GRE MR imaging for detection. Radiology. 2008;248(1):272-7.

17. Cordonnier C, Potter GM, Jackson CA, et al. improving interrater agreement about brain microbleeds: development of the Brain Observer MicroBleed Scale (BOMBS). Stroke. 2009;40(1):94-9.

18. Nandigam RN, Viswanathan A, Delgado P, et al. MR imaging detection of cerebral microbleeds: effect of susceptibility-weighted imaging, section thickness, and field strength. AJNR Am J Neuroradiol. 2009;30(2):338-43.

19. de Rochefort L, Brown R, Prince MR, Wang Y. Quantitative MR susceptibility mapping using piece-wise constant regularized inversion of the magnetic field. Magn Reson Med. 2008;60(4):1003-9.

20. de Rochefort L, Liu T, Kressler B, et al. Quantitative susceptibility map reconstruction from MR phase data using bayesian regularization: validation and application to brain imaging. Magn Reson Med. 2010;63(1):194-206.

21. Li W, Wu B, Liu C. Quantitative susceptibility mapping of human brain reflects spatial variation in tissue composition. Neuroimage. 2011.

22. Liu J, Liu T, de Rochefort L, Khalidov I, Prince M, Wang Y. Quantitative susceptibility mapping by regulating the field to source inverse problem with a sparse prior derived from the Maxwell Equation: validation and application to brain. ISMRM

Proceedings. 2010:4996.

23. Liu T, Spincemaille P, De Rochefort L, Kressler B, Wang Y. Multiple Orientation Acquisition to Invert Dipole Field for Quantitative Susceptibility Mapping Proc ISMRM. 2008:643.

24. Liu T, Spincemaille P, de Rochefort L, Wong R, Prince M, Wang Y. Unambiguous identification of superparamagnetic iron oxide particles through quantitative susceptibility mapping of the nonlinear response to magnetic fields. Magn Reson Imaging. 2010;28(9):1383-9.

25. Schweser F, Deistung A, Lehr BW, Reichenbach JR. Differentiation between diamagnetic and paramagnetic cerebral lesions based on magnetic susceptibility mapping. Med Phys. 2010;37(10):5165-78.

26. Shmueli K, de Zwart JA, van Gelderen P, Li TQ, Dodd SJ, Duyn JH. Magnetic susceptibility mapping of brain tissue in vivo using MRI phase data. Magn Reson Med. 2009;62(6):1510-22.

27. Wharton S, Bowtell R. Whole-brain susceptibility mapping at high field: a comparison of multiple- and single-orientation methods. Neuroimage. 2010;53(2):515-25.

28. Wharton S, Schafer A, Bowtell R. Susceptibility mapping in the human brain using threshold-based k-space division. Magn Reson Med. 2010;63(5):1292-304.

29. Kressler B, de Rochefort L, Liu T, Spincemaille P, Jiang Q, Wang Y. Nonlinear regularization for per voxel estimation of magnetic susceptibility

distributions from MRI field maps. IEEE Trans Med Imaging. 2010;29(2):273-81.

30. Marques JP, Bowtell R. Application of a Fourier-based method for rapid calculation of field inhomogeneity due to spatial variation of magnetic susceptibility. Concepts in Magnetic Resonance Part B: Magnetic Resonance Engineering. 2005;25B(1):65-78.

31. Liu T, Liu J, de Rochefort L, et al. Morphology Enabled Dipole Inversion (MEDI) from a single angle acquisition: comparison with COSMOS in human brain imaging. Magn Reson Med. 2010;in press.

32. Liu J, Liu T, de Rochefort L, Khalidov I, Prince M, Wang Y. Quantitative Susceptibility Mapping by Regulating the Field to Source Inverse Problem with a Sparse Prior Derived from the Maxwell Equation: Validation and Application to Brain. Proceedings 18th Scientific Meeting, International Society for Magnetic Resonance in Medicine. Stockholm, Sweden2010; p. 4996.

33. Haacke EM, Xu Y, Cheng YC, Reichenbach JR. Susceptibility weighted imaging (SWI). Magn Reson Med. 2004;52(3):612-8.

34. Schrag M, McAuley G, Pomakian J, et al. Correlation of hypointensities in susceptibility-weighted images to tissue histology in dementia patients with cerebral amyloid angiopathy: a postmortem MRI study. Acta Neuropathol. 2009.

35. Liu T, Spincemaille P, de Rochefort L, Kressler B, Wang Y. Calculation of susceptibility through multiple orientation sampling (COSMOS): a method for conditioning the inverse problem from measured magnetic field map to susceptibility

source image in MRI. Magn Reson Med. 2009;61(1):196-204.

36. Xi G, Keep RF, Hoff JT. Mechanisms of brain injury after intracerebral haemorrhage. Lancet neurology. 2006;5(1):53-63.

37. Lou M, Lieb K, Selim M. The relationship between hematoma iron content and perihematoma edema: an MRI study. Cerebrovascular diseases (Basel, Switzerland). 2009;27(3):266-71.

38. McAuley G, Schrag M, Barnes S, et al. Iron quantification of microbleeds in postmortem brain. Magn Reson Med. 2010.

39. Schweser F, Deistung A, Lehr BW, Reichenbach JR. Quantitative imaging of intrinsic magnetic tissue properties using MRI signal phase: An approach to in vivo brain iron metabolism? Neuroimage. 2010.

40. Zurkiya O, Chan AW, Hu X. MagA is sufficient for producing magnetic nanoparticles in mammalian cells, making it an MRI reporter. Magn Reson Med. 2008;59(6):1225-31.

41. Smith SM. Fast robust automated brain extraction. Hum Brain Mapp. 2002;17(3):143-55.

42. Cusack R, Papadakis N. New robust 3-D phase unwrapping algorithms: application to magnetic field mapping and undistorting echoplanar images. Neuroimage. 2002;16(3 Pt 1):754-64.

CHAPTER 8

8 FUTURE DIRECTIONS AND CONCLUSION

8.1 Future Directions

Since the generation of the first QSM, methodology has evolved rapidly to overcome various technical barriers. Future research areas of QSM may include the performance of QSM at high field, algorithmic improvements for better reliability and speed, and exploration of the applications.

8.1.1 QSM at High Field

Since magnetic susceptibility characterizes the degree of magnetization, a stronger polarization field is naturally desirable for susceptibility calculation. So far, QSM has been performed at 1.5 T and 3 T. The noise level at 3 T is evidently lower than that at 1.5 T as seen in Figure 6.3 and Figure 6.4. This observation agrees with MR signal theory. At a higher field strength such 7 T, the magnetization will be stronger for most materials that are paramagnetic or diamagnetic, improving the sensitivity of QSM. The enhanced signal noise ratio in the original MR signal can be translated to a reduced noise level on the reconstructed QSM. Utilizing this intrinsic gain in SNR, smaller voxels can be used to alleviate the partial volume effect and digitization error, or faster data acquisition can be used capture dynamic profiles. At 7 T, it is possible that the phase contrast between cortical gray and white matter is strong enough that MEDI will no longer underestimate the susceptibility in this region.

8.1.2 Algorithmic Improvements

QSM consists of several sequential steps: field map estimation, phase unwrapping, background field removal, and the inversion. Hence, improvement in each of the steps can lead to an improvement in the final reconstruction.

In the field map estimation process, water-fat separation can be incorporated. The existence of fat causes an additional chemical shift on the field map. This additional component and the field induced by susceptibility are superimposed in space. However, their contribution to the observed MR signal can be modeled using a nonlinear formula. Advance water-fat separation techniques have shown promising field map estimation in the presence of fat, although its influence on the accuracy of the final QSM still needs investigation.

For phase unwrapping and background field removal, the opportunity for improvement lies at the boundary of the air-tissue interface. This interface not only results in a rapid field variation, but also leads to reduced signal noise ratio in the original MR signal due to T2* decay. Strategies to enhance the reliability of the measurement in this region is likely to have a substantial impact on the estimated local field map.

The inversion technique has the greatest room for further development. One major limitation of the current QSM inversion technique is its robustness. The noise on the phase image follows a distribution in which the probability of an error does not vanish as it deviates from zero. However, for numerical simplicity and with approximation, the noise is usually treated as Gaussian distribution. Better mechanisms to account for the non-Gaussian noise have been studied previously in robust regression, and we may

be able to translate the insights to QSM. Another opportunity is to improve the precision for materials with weak susceptibility. The current l_1 implementation preferentially underestimates materials with weak susceptibility and weak boundary. An enhanced boundary definition is a potential remedy for this regional underestimation.

Last but not least, the current MEDI implementation involves solving a weighted l_1 minimization using a quasi-Newton method that requires a long computational time. To improve the speed, three approaches are worth to investigate. First, more sophisticated solvers such as interior points methods can be employed to solve the l_1 minimization problem. Second, in the quasi-Newton method, the benefits and drawbacks of various iterative update schemes need to be better understood. Third, with increasing computation power provided by multi-core central processing unit (CPU) or general purpose graphics processing units (GPGPU), it is possible to achieve parallelization of the computation to shorten the total reconstruction time.

8.1.3 Exploration of Applications

In an *in vivo* environment, major endogenous susceptibility sources include iron and calcification. Additionally, iron based and gadolinium based contrast agents also demonstrate strong paramagnetism. Focusing on the identification and quantification of these materials, the potential applications are listed as follows.

Utilizing the linear relationship between contrast agent concentration and susceptibility, QSM may be applied to preclinical animal models may facilitate the development of targeted drugs, which requires monitoring the bio-distribution of the

drug after administration. If contrast agents are bound to the drug, we can use susceptibility to quantify the contrast agent concentration and further infer the drug concentration. This approach inherits the intrinsic advantages of MRI, such as large field of view, excellent contrast of soft tissue, and non-invasiveness for repetitive assessments, and overcomes the non-linear relationship between signal intensity and drug concentration that has plagued conventional MRI methods for reliable quantification.

Because MRI is very sensitive to iron and iron is a vital element to human life, it may prove to be valuable to apply QSM to measure the iron concentration in human brain and stratify the iron-related diseases. For example, motor deterioration has been suggested to be associated with iron deficiency, and neurodegenerative diseases including Alzheimer's disease, Parkinson's disease, Huntington chorea and Hallervorden-Spatz syndronme have been observed to be associated with elevated brain iron level.

QSM may also be useful for quantifying the concentration of gadolinium based contrast agents routinely used in brain MRI. Conventional MRI utilizes the T1 shortening effect of gadolinium to enhance lesions with excessive gadolinium uptake. This enhancement is nonlinear and subject to T1 saturation, i.e., increase in gadolinium concentration may not result in signal enhancement. On the contrary, susceptibility is linear to the concentration of gadolinium as illustrated in Figure 4.4, allowing a more accurate estimation of gadolinium quantification. This is beneficial for assessing tissue vascularity in tumor grading or surgical planning to excise tumor. If the data acquisition can be substantially accelerated in the future, QSM may be used

to monitor perfusion in dynamic contrast enhanced MRI to estimate the microvascular permeability.

8.2 Conclusion

In this thesis, a framework for estimating tissue magnetic susceptibility in MRI is presented. Within the framework, a projection onto dipole fields technique is presented to allow clear visualization and accurate estimation of the local field induced from susceptibility sources of interest. Subsequently, two independent inversion techniques are proposed to solve for the susceptibility sources from the estimated local field, both of which have been validated experimentally. The utility of quantitative susceptibility mapping (QSM) was demonstrated in two applications. In molecular MRI, QSM allows an unambiguous identification of iron-based contrast agents in the presence of air. In cerebral MRI, QSM enables an objective measurement of cerebral microbleed burden independent of the choice of echo time, which is essential for longitudinal patient follow-up and cross center subject comparison.